

# FABRICATION, CHARACTERIZATION AND TESTING OF FUNCTIONALLY GRADED ALUMINUM-BASED TARGETS FOR SPUTTERING DEPOSITION OF HYBRID COMPOSITES

By

Glorimar Ramos Rivera

A thesis submitted in partial fulfillment of the requirements for the degree of

**MASTER OF SCIENCE**  
in  
**MECHANICAL ENGINEERING**

UNIVERSITY OF PUERTO RICO  
MAYAGÜEZ CAMPUS  
2011

Approved by:

\_\_\_\_\_  
Pedro Quintero, Ph.D.  
Member, Graduate Committee

\_\_\_\_\_  
Date

\_\_\_\_\_  
Ricky Valentín, Ph.D.  
Member, Graduate Committee

\_\_\_\_\_  
Date

\_\_\_\_\_  
O. Marcelo Suárez, Ph.D.  
Chair, Graduate Committee

\_\_\_\_\_  
Date

\_\_\_\_\_  
Rogelio Palomera García, Ph.D.  
Representative of Graduate Studies

\_\_\_\_\_  
Date

\_\_\_\_\_  
J. Gustavo Gutiérrez, Ph.D.  
Chairperson of the Department

\_\_\_\_\_  
Date

## Abstract

---

The fabrication, characterization and testing of sputtering targets were completed for the deposition of hybrid composites. The chemical composition of the target specimens consisted of an aluminum-silicon matrix reinforced with  $\text{AlB}_{12}$  and  $\text{AlB}_2$  particles. These composites were manufactured by centrifugal casting and vacuum casting (as control samples). The characterization of the composites was divided into three sections: structure, mechanical properties and thermal properties. The characterization results showed better segregation of reinforcement in the composites containing  $\text{AlB}_2$  particles. Associated with this particle segregation accompanying changes in the mechanical and thermal properties of the compound were found. The thermal analysis of the composites showed that both silicon and the presence of borides in the composite were responsible for the decrease in melting point and thermal expansion coefficient of the compound respectively.

The fabricated targets were mounted in the AJA sputtering system with varying power from 200 to 450 W to determine which of the power set produced films with the smallest surface roughness; in this case was 450W. Afterwards, at this power films were deposited over glass, silicon and polymer substrates. Preliminary studies of structure and mechanical properties of the films showed that the films produced with the centrifuged targets had smaller grain size, dominant compression stresses, higher hardness and elastic modulus, and higher disorder in the crystalline structure when compared to the films produced with pure aluminum target.

## Resumen

---

La fabricación, caracterización y prueba de blancos de deposición fue llevada a cabo para deposición de compuestos híbridos. La composición química de los compuestos consistía en una matriz de aluminio-silicio reforzada con partículas de  $\text{AlB}_2$  y  $\text{AlB}_{12}$ . Los compuestos fueron fabricados por fundición centrífuga y fundición al vacío (como muestras control). La caracterización de los compuestos se dividió en tres secciones: estructura, propiedades mecánicas y propiedades termales. Los resultados de la caracterización demostraron mejor segregación de partículas en los compuestos reforzados con partículas de  $\text{AlB}_2$ . Junto con este gradiente de partículas también se encontró un cambio en las propiedades mecánicas y termales del compuesto. Las mejores propiedades fueron encontradas en las zonas donde había una mayor segregación de refuerzos. El análisis termal de las muestras demostró que tanto el silicio como la presencia de boruros en el compuesto eran responsables de la disminución en el punto de fusión y coeficiente de expansión termal del compuesto respectivamente.

El análisis de los blancos de deposición en el equipo de "sputtering" consistió en variar la potencia de 200 hasta 450 W para determinar cuál de ellas resultaba la lámina con la menor rugosidad de superficie posible, en este caso fue 450W. A esta potencia fueron fabricadas las láminas depositadas sobre substratos de vidrio, silicio y polímero. La estructura y las propiedades mecánicas de las láminas fueron estudiadas preliminarmente. Los resultados demostraron que las láminas fabricadas con los blancos de deposición centrifugados obtuvieron menor tamaño de grano, esfuerzos en compresión, mayor dureza y modulo elástico, mayor desorden en la estructura cristalina que las muestras fabricados con aluminio puro.

## Acknowledgements

---

A major research project like this is never the work of only one person. The contributions of many different people, in different ways, have made this possible. I would like to extend my appreciation especially to the following.

Thank God for the wisdom and perseverance that he has been bestowed upon me during this thesis, and indeed, throughout my life.

Special thanks also to my advisor Dr. O. Marcelo Suárez because from the initial stages of this thesis, to the final draft, I owe an immense debt of gratitude to him where his sound advice assistance, support and careful guidance were invaluable.

Also to all my graduate friends, especially; Boris Rentería, Natalia Cortés, Gabriel J. Negrón, Jairo Boada, and Elvin Estremera for sharing the literature, invaluable assistance, their knowledge and their in sincere friendship.

I want to express my love and gratitude to my beloved families; for their understanding & endless love, through the duration of my studies, also, to my love Juan J. Reinés for his endless support.

To each of the above, I extend my deepest appreciation.

# Table of Contents

---

Abstract.....	ii
Resumen .....	iii
Acknowledgements.....	iii
Table of Contents.....	v
List of Figures .....	viii
List of Tables .....	xii
Chapter 1: Introduction.....	1
1.1. Literature Review .....	2
1.1.1. Functionally Graded Composites.....	2
1.1.2. Aluminum-Boron Alloys .....	4
1.1.3. Aluminum-Silicon Alloys .....	5
1.1.4. Sputtering Deposition .....	6
1.1.5. Literature Review Summary.....	8
1.2. Objectives .....	9
Chapter 2: Background .....	10
2.1. Introduction .....	10
2.2. Composites Description .....	10
2.3. Metal Matrix Composites (MMCs) .....	12
2.4. Aluminum Matrix Composites (AMCs).....	13
2.5. Aluminum-Silicon System.....	13
2.6. Aluminum-Boron System.....	16
2.7. Aluminum – Boron – Silicon Systems.....	17
2.8. Functionally Graded Materials (FGMs).....	18
2.9. Physical Vapor Deposition (PVD).....	20
2.9.1. Vacuum deposition .....	21
2.9.2. Ion Plating .....	21
2.9.3. Sputter Deposition .....	22
2.10. Thin Film Technology .....	23
2.11. Microstructure of Aluminum Thin Films.....	24
Chapter 3: Methodology of Fabrication and Characterization of Sputtering Targets .....	26
3.1. Material Description.....	26

3.2. Fabrication of Sputtering Targets .....	27
3.2.1. Description of the Centrifugal Caster .....	28
3.2.2. Description of the Vacuum Equipment.....	29
3.3. Experimental Procedure.....	30
3.3.1. Specimen Cutting and Sample Dimensions .....	31
3.3.2. Metallographic Preparation.....	32
3.4. Characterization of Specimens.....	32
3.4.1. Microstructure Analysis.....	32
3.4.2. Hardness.....	33
3.4.2.1. Rockwell Hardness .....	33
3.4.2.2. Vickers Microhardness .....	34
3.4.2.3. Nanoindentation .....	34
3.5.1. Thermal Characterization .....	35
3.5.1.1. Differential Thermal Analysis (DTA).....	35
3.5.1.2. Thermomechanical Analysis (TMA) .....	36
Chapter 4: Results and Discussion .....	37
4.1. Microstructure Analysis .....	37
4.1.1. Microstructure of Vacuum Cast Specimens .....	37
4.1.2. Microstructure of Centrifugally Cast Specimens.....	39
4.1.3. Scanning Electron Microscopy.....	42
4.1.4. X-Ray Diffraction .....	45
4.1.5. Volume Fractions of Particles and Pores .....	48
4.1.6 Average Grain Size .....	50
4.2. Hardness.....	53
4.2.1. Superficial Rockwell Hardness and Vickers Microhardness .....	53
4.2.2. Mechanical Properties via Nanoindentation .....	56
4.2.3. Discrepancy between hardness measurements.....	62
4.3. Thermal Characterization .....	64
4.3.1. Differential Thermal Analysis (DTA).....	64
4.3.1.1. Centrifuged and Vacuum Cast Specimens.....	64
4.3.1.2. Effect of Boron and Silicon on the Thermal Properties of Al-Si-B Composites ..	67
4.3.2. Coefficient of Thermal Expansion (CTE) via Thermomechanical Analysis .....	68
Chapter 5: Methodology of Fabrication and Characterization of the Hybrid Composites .....	72
5.1. Polymer Description and Method of Fabrication .....	72

5.2. Description of Sputtering System .....	73
5.3. Sputtering Process .....	74
5.4. Experimental Setup .....	74
5.5. Selection of the Target Material .....	75
5.6. Deposition Parameters and Fabrication Process of the Films.....	76
5.7. Thin Film Characterization .....	77
5.7.1. Experimental Procedure .....	77
5.7.2. Morphology:.....	78
5.7.2.1. Thickness Measurement.....	78
5.7.2.2. Atomic Force Microscopy.....	79
5.7.2.3. X-ray Diffraction .....	79
5.7.3. Mechanical Characterization: Nanoindentation .....	80
Chapter 6: Results and Discussion .....	81
6.1. Morphology and Thickness Measurement .....	81
6.2. Film Roughness .....	84
6.2.1. Surface Roughness of films deposited over glass substrates .....	85
6.2.2. Surface Roughness of Films Deposited on the Polymer Substrate .....	87
6.3. Films Topography Study Using AFM .....	89
6.4. X-Ray Diffraction Analysis .....	91
6.4.1. XRD: Silicon Substrates .....	92
6.4.1.1 Comparison between AFM analysis and the measured crystallite size .....	94
6.4.2. XRD: Polymer Substrate.....	95
6.4.2.1. Grain Size of Films Deposited Over Polymer Substrates .....	97
6.5. Mechanical Properties of the Deposited Films.....	98
6.5.1. Films on Glass Slide Substrates .....	100
Chapter 7: Conclusions and Future Work.....	102
7.1 Conclusions .....	102
7.2 Future Work .....	107
References:.....	108

## List of Figures

---

Figure 1 Classification of composites material with metal matrixes. ....	12
Figure 2 Schematic illustration of the reinforcement type about MMC: a) long unidirectional fiber; b) short fiber and whiskers; c) particles [25]. ....	12
Figure 3 Aluminum-silicon equilibrium phase diagram [16]. ....	14
Figure 4 Aluminum-silicon phase diagram and microstructure (amended from [25]). ....	15
Figure 5 The Al-B binary phase diagram [29]. ....	16
Figure 6 Calculated vertical section in the Al–B–Si system at constant 0.1 wt.% B. The ternary eutectic liquid composition is 12.5 wt.% Si and only 0.01 wt.% B; the temperature is 0.1C below the 577.0 °C of the binary Al–Si eutectic [34]. ....	17
Figure 7 Schematic of FGM microstructure before and after centrifuging. ....	19
Figure 8 Schematic of the vacuum deposition process [40]. ....	21
Figure 9 Schematic representation of the ion plating process [41]. ....	22
Figure 10 Schematic representation of sputtering process using a DC source [42]. ....	23
Figure 11 Standard Zone Diagram for Metallic Thin Films [46]. ....	25
Figure 12 Optical micrographs of the master alloys used; a) Al-5wt%B <sub>2</sub> b) Al-12wt%Si c) Al- 5wt%B <sub>12</sub> d) Pure aluminum. ....	27
Figure 13 CAD model of graphite mold. ....	28
Figure 14 Top view of the centrifugal caster. ....	29
Figure 15 Front view of the adapted vacuum equipment. ....	30
Figure 16 Flow chart of experimental procedure of the bulk material. ....	30
Figure 17 Sample cutting and dimensions with respect to the applied centrifugal force. ....	32
Figure 18 LECO Rockwell LR-50 hardness tester. ....	33
Figure 19 Microhardness Tester. ....	34
Figure 20 Agilent G200 Nanoindenter. ....	35
Figure 21 Mettler Toledo TGA/SDTA 851 <sup>e</sup> equipment. ....	36
Figure 22 Mettler Toledo TMA/SDTA 840 <sup>e</sup> . ....	36
Figure 23 Optical images of composites containing a) AlB <sub>2</sub> particles and b) AlB <sub>12</sub> particles. ....	38
Figure 24 Micrographs of vacuum cast composites with different weight percent of boron a) 2 wt.%B <sub>2</sub> , b) 3 wt.%B <sub>2</sub> , c) 2 wt.%B <sub>12</sub> and d) 3 wt.%B <sub>12</sub> . ....	38
Figure 25 Microstructures of the centrifuged specimens with the three defined zones for samples with different weight percent of diboride particles. ....	40

Figure 26 Microstructures in the three defined zones for samples with different weight percent of dodecaboride particles. ....	41
Figure 27 a) SEM image of Al-3wt%B <sub>12</sub> -3%Si, b) Global EDS spectrum obtained on the SEM image area of figure a); c) SEM image of Al-3wt%B <sub>2</sub> -3%Si; d) Global EDS spectrum obtained on the SEM image area of figure c). ....	43
Figure 28 EDS mapping of the Al-3wt%B <sub>12</sub> -3%Si composite. ....	44
Figure 29 EDS mapping of the Al-3wt%B <sub>2</sub> -3%Si composite. ....	44
Figure 30 XRD curves showing the phases present on the Al-3wt.%B <sub>12</sub> -3wt.%Si. ....	46
Figure 31 XRD curves showing the phases present on the Al-3wt.%B <sub>2</sub> -3wt.%Si. ....	47
Figure 32 AlB <sub>2</sub> peak. ....	47
Figure 33 a) Boride particles volume percent as function of wt.%B <sub>x</sub> , b) Silicon particles volume percent as a function of wt.%B <sub>x</sub> and c) Pores volume percent as a function of wt.%B. ....	49
Figure 34 Measured average ASTM grain size G. ....	51
Figure 35 Optical micrographs of grain size distributions throughout centrifuged Al-2wt%B <sub>2</sub> -3wt%Si composite compared with Al-2wt%B <sub>2</sub> -3wt%Si vacuum cast specimen. ....	52
Figure 36 Superficial Rockwell hardness along the longitudinal axis of the centrifugally cast Al-B-Si composites: a) containing AlB <sub>2</sub> , b) containing AlB <sub>12</sub> . ....	53
Figure 37 Vickers microhardness along the longitudinal axis of centrifugally cast Al-B-Si composites: a) containing AlB <sub>2</sub> , b) containing AlB <sub>12</sub> . ....	54
Figure 38. SEM secondary electron images of undamaged areas of Al-B-Si composites a) AlB <sub>2</sub> and b) AlB <sub>12</sub> . ....	55
Figure 39. SEM images of Rockwell indentation on both composites studied within the Rockwell indentation mark on a composite containing: a) diboride particles; and c) dodecaboride particles. ....	56
Figure 40 Elastic modulus as a function of hardness obtained via nanoindentation from different localizations of composites containing diboride and dodecaboride particles. ....	57
Figure 41 Schematic of the Composite Sphere Model used in [63]. ....	58
Figure 42 Elastic Modulus of AlB <sub>2</sub> and AlB <sub>12</sub> particles via nanoindentation at different range of loadings a) 4-8mN and b) 60-70mN. ....	59
Figure 43 Optical micrographs of the array performed over the borides samples where includes the indent locations around and over the particles a) AlB <sub>2</sub> sample b) AlB <sub>12</sub> sample. ....	59
Figure 44 MATLAB plots of the evolution of the elastic modulus at different locations in the array, a) elastic modulus distribution near an AlB <sub>2</sub> particle: b) contour plot of (a): c) elastic modulus distribution near an AlB <sub>12</sub> particle: and d) contour plot of (c). ....	61

Figure 45 Contour plots of hardness distribution array near particles: a) $\text{AlB}_2$ ; and b) $\text{AlB}_{12}$ . ....	62
Figure 46 DTA thermograms for the centrifugal and vacuum cast samples upon heating. The first endothermic peak corresponds to the Al-Si eutectic melting and the second one to the matrix melting of Al-2wt%B <sub>2</sub> -3wt%Si composites. ....	64
Figure 47 DTA curves of Al-3wt%Si, Al-2wt%B <sub>2</sub> and pure aluminum obtained for reference purposes. ....	65
Figure 48 DTA thermograms obtained upon heating to study the influence of boron on the melting of the composites. ....	66
Figure 49 DTA thermograms showing the effect of boride particles on the matrix melting point. ....	67
Figure 50 DTA thermograms of the influence of silicon percent in Al-3wt.%B <sub>2</sub> composites. ....	68
Figure 51 CTE of centrifuged and vacuum cast specimens as a function of reinforcement volume percent. ....	70
Figure 52 CTE of centrifuged and vacuum cast specimens. ....	70
Figure 53 CTE of gravity cast samples as a function of silicon and boron percent. ....	71
Figure 54 Poly(styrene-isobutylene-styrene) ABA structure. ....	73
Figure 55 Sputtering System Description. ....	74
Figure 56 Photograph of Sputtering Process. ....	75
Figure 57 Experimental procedure flow chart of film characterization. ....	77
Figure 58 KLA Tencor P-6. ....	78
Figure 59 Photograph of the EasyScan atomic force microscope. ....	79
Figure 60 Film thickness as function of the discharged power. ....	83
Figure 61 SEM micrographs of the targets used after sputtering: a) aluminum; b) diboride containing target material c) dodecaboride containing target material. ....	83
Figure 62 Dodecaboride particle eroded by the Ar plasma during the sputtering process. ....	84
Figure 63 Roughness of the film deposited. ....	86
Figure 64 Summary of AFM image of films surfaces used for roughness measurements. ....	86
Figure 65 AFM-measured RMS roughness values for sputtered alloys. ....	87
Figure 66 Surfaces AFM images of: a) SIBS film, b) aluminum film, c) Al-Si/ $\text{AlB}_2$ film and d) Al-Si/ $\text{AlB}_{12}$ film. ....	88
Figure 67 Topographical AFM images of polymer substrate and films produced via sputtering, a) SIBS image: b) perspective image of (a): c) Aluminum film image: d) perspective image of (c): e) Al-Si/ $\text{B}_2$ film image: f) perspective image of (e): g) Al-Si/ $\text{B}_{12}$ film image: h) perspective image of (g). ....	91

Figure 68 Diffraction profiles of the films deposited over the silicon substrates: a) aluminum target and b) fabricated targets. ....	93
Figure 69 AFM images of the films deposited over silicon wafers: a) aluminum; b) Al-Si/3wt.%AlB <sub>2</sub> ; c) Al-Si/3wt.%AlB <sub>12</sub> . ....	95
Figure 70 Characteristic peaks of the sputtered films deposited over SIBS. ....	96
Figure 71 XRD of the films deposited over SIBS substrates: a) aluminum target and b) fabricated targets. ....	97
Figure 72 Characteristic field emission SEM micrographs used to measure the grain size of the produced films. ....	98
Figure 73 Characteristic load vs displacement curves for films produced with dodecaboride containing target. ....	100
Figure 74 Nanoindentation results of the produced films deposited over glass slides substrates a) Elastic modulus and b) hardness. ....	101

## List of Tables

---

Table 1 Thin Film Applications [43].	24
Table 2 Chemical Composition of Cast Composites.	27
Table 3 Centrifugal Casting Parameters.	29
Table 4 Eutectic range as measured on the DTA curves.	66
Table 5 Melting range measured on the DTA curves.	66
Table 6 Eutectic and matrix melting signals measured on the reference specimens.	67
Table 7 Sputtering Parameters.	76
Table 8 Computed Al lattice parameters of the sputtered films.	94
Table 9 Analysis of the diffractograms from films deposited on polymers substrates.	97

## Chapter 1: Introduction

---

The present thesis focuses on the design, fabrication, characterization and preliminary testing of sputtering targets for deposition on substrates intended for hybrid composites. Such composites are being developed for applications such as MEM resonators and switches. A novel metal-based composite (MBC) is formulated to design the targets for sputtering. To produce such material with controlled microstructure gradients, the MBC is produced by centrifugal casting. This technique allows fabricating a functionally-graded material (FGM), which is normally defined as a non-homogenous composite whose properties are different along some spatial direction. For the present research the FGM consists of an aluminum matrix containing silicon with boride particles as reinforcements.

Aluminum has been selected as the matrix metal because of its low density, high ductility, and high electrical and thermal conductivities. The presence of boride particles permits adjusting the stiffness and wear resistance of the aluminum matrix, while silicon improves the castability of the part and the overall strength of the material. Fabricating the sputtering targets by centrifugal casting is essential as one can obtain a number of targets with different amounts of particles in one fabrication process. The targets are then sliced from the casting with the proper thickness (required by the sputtering gun). In each casting one can gradually adjust the physical, chemical, and mechanical properties of the composite as required by the intended application.

Testing the adequacy of the targets is the final stage of this project. The targets will be used in the sputtering system to produce thin films. Hence, the combination of the centrifugal casting and the sputter deposition techniques would permit the precise design of highly reliable composites.

## 1.1. Literature Review

The realization of this work has involved the use of two distinct themes and/or techniques in order to obtain a final product, which is in this case the assembly of hybrid composites for devices. For this reason, this section of the thesis is subdivided in two subsections. The first subsection focuses on the materials science background related to the fabrication process of the composites and the benefits of the selected reinforcements. The second subsection involved basic understanding of electronic materials processing, more specifically, on the parameters affecting the sputtering deposition of thin films.

### 1.1.1. Functionally Graded Composites

Relevant work related to functionally gradient materials (FGM) or composites can be found in works like the one due to Suresh et al [1]. The authors defined FGMs as a class of composite materials consisting of two or more phases, which is fabricated with its composition and/or microstructure varying in some spatial direction. Other works that involve the study of mechanical and thermal properties of FGM composites are due to Watanabe et al [2] and Kang et al [3]. Watanabe carried out a microstructure study and mechanical properties analysis of FGMs fabricated by a centrifugal casting technique, which produced particle distribution gradients of compounds of Al/SiC, Al/Al<sub>3</sub>Ti, and Al/Al<sub>3</sub>Ni. These authors reported the variation of matrix hardness following the composition gradient. Mechanical properties such as Young's modulus, internal friction, and fatigue crack growth in an *in-situ* Al/Al<sub>3</sub>Ni FGM were also evaluated. The study mainly showed that SiC particles moved toward the outer parts of the casting under the action of centrifugal force (due to the density difference between reinforcements and matrix).

Kang et al [3] developed a transient thermal analysis of solidification in a centrifugal casting for composite materials containing particle segregation . In this work the authors studied one-dimensional heat transfer analysis at some stage in centrifugal casting technique using an aluminum-copper alloy containing  $Al_2O_3$ , SiC, and graphite particles. They proposed a numerical model of particle segregation during centrifugal casting of a liquid metal containing suspended particles. In addition, they observed that liquid metal temperature was influenced by the speed of rotation, the variation of reinforcement and the constitution (chemical composition) of the base alloy. Additionally, the initial mold temperature and its speed of rotation were found to significantly affect the solidification time due to particle segregation. This has been recently corroborated by T. Adelakin et. al in an FGM made of an aluminum matrix composite reinforced with boride particles [4].

Another relevant work is the one performed by Wang [5] in 20% SiC<sub>p</sub>/Al composites. In this research the external zone of a cylinder cast under centrifugal force was enriched with carbide particles while some SiC particles were segregated in the inner zone of the cylinder. As a result, a cylinder with external reinforced zone, and inner particle-free zone was fabricated by centrifugal casting. The calculated particle volume fraction and the measured Brinell hardness corroborated the segregation. Similar results can be found in the works performed by Melgarejo [6] and Adelakin [7]. The main differences between those two works and Wang's study are the equipment utilized, the relative position of the casting with respect to the centrifugal force and the composition of the material used and the type of reinforcements used.

Melgarejo [6] and Adelakin [7] in their thesis work used a centrifugal caster to produce FGMs of aluminum matrix. Melgarejo completed an intensive microstructure characterization of centrifugally cast aluminum matrix composites containing 2 wt.% Mg – and 1, 2, 3 and 4 wt.% B. In this research he analyzed the wear strength of the fabricated specimens. Later, Adelakin

performed an extensive investigation based on a systematic study of centrifugal casting parameters and on Al-Cu, Al-Mg and pure aluminum-based composites with different boride particles volume fractions. Both works revealed extensive boride particles segregation towards the external zone compared with the internal zone of the casting. As a consequence, higher hardness and higher resistance to wear were measured in the casting outer region.

Furthermore, Calderón in his thesis work [8], performed a large study of fatigue under high loading rates with a series of composites with an Al-Cu-Mg matrix reinforced with  $AlB_2$  dispersoids in homogeneous (via gravity casting) and functionally graded conditions (via centrifugal casting). Calderón obtained through centrifugal casting a gradual variation of the volume fraction of reinforcing particles along the cross section. He also discovered an unexpected interaction between Mg and the  $AlB_2$  particles, which was responsible for some strength reduction of the composites. The author demonstrated that the particle distribution affected the crack growth behavior of the FGMs, decreasing the fatigue resistance when the crack tip traveled through higher particle density zones.

In closing, the different works discussed above have in common that they clearly demonstrated the feasibility of the fabrication of FGM using the centrifugal casting technique. In that respect this thesis uses the extensive experience acquired in those works and implemented their recommendations as background for the fabrication of an FGM consisting of an aluminum-silicon matrix containing boride particles as reinforcements.

### **1.1.2. Aluminum-Boron Alloys**

It is well known that at high temperature boron reacts with liquid aluminum producing diboride and dodecaborides. These borides act as effective reinforcement of the solid aluminum matrix

and increase the overall strength of Al-B based material, which has low production cost, according to Suárez [9]. Further modification of the matrix to contain elements with high solubility in Al can also help raise the strength of the material. At UPRM laboratories, it was discovered that  $\text{AlB}_{12}$  particles (with observed microhardness values of  $\sim 2,800$  HV) embedded in an Al matrix can be a better reinforcement for aluminum, at the microscale as well as at the nanoscale. According to Mirkovic [10] the  $\text{AlB}_{12}$  phase can also be considered as a promising compound for high temperature thermoelectric applications and aircraft protection.

Additionally, it is known that inoculation of Al alloys with small amounts of aluminum-boron alloys results in improved electrical and thermal conductivities by depleting the melt of chromium, titanium, vanadium and zirconium, according to Jackson [11]. Many studies have shown that Al-B master alloys are also effective grain refiners of cast Al-Si alloys [12-14]. Moreover, borides present in those alloys can provide strengthening to the matrix, whereas the presence of boride particles permits adjusting the stiffness and wear resistance of the aluminum matrix, as indicated by Melgarejo [15].

### **1.1.3. Aluminum-Silicon Alloys**

Al-Si master alloys are widely used in the fabrication of casting alloys due to their excellent castability and a good compromise between mechanical properties and light weight. Their application as structural materials is favored by their physical properties (primarily influenced by their chemical composition) and their mechanical properties (influenced by both chemical composition and microstructure) that were studied by many authors including Warmuzek [16]. In particular, the outstanding effect of silicon in cast aluminum alloys is the improvement of their casting characteristics. Additions of silicon to pure aluminum dramatically improve fluidity, hot

tear resistance, and feeding characteristics upon casting. This is also accompanied by a reduction in specific gravity and thermal expansion coefficient, as indicated by Rooy. [17].

#### **1.1.4. Sputtering Deposition**

A relevant work concerning sputtering targets and their deposition yields is found in an article by Terwagne et al.[18]. In this work the authors used two sputtering Si-Al alloys targets with different chemical composition. The authors identified the targets as  $T_1$  and  $T_2$  where the  $T_1$  had a composition of  $Si_{50}Al_{50}$  and the fabrication method of the target was by embedding silicon grains in an aluminum matrix. For  $T_2$  the composition was  $Si_{70}Al_{30}$  and its fabrication was using pressed powder. They also found that the sputtering yield of the aluminum is twice larger than silicon resulting in preferential sputtering effects of Al over Si. As a result, the authors recommended that Al-Si sputtering targets be preferred over the Si-Al composites.

As aforementioned, in order to understand the experimental procedures concerning sputtering deposition, first it is necessary to review the parameters that are involved in the sputtering process. Work concerning the production of thin films via radio frequency magnetron sputtering deposition was presented by Jeong, et al. [19]. In this work they described the effect of sputtering parameters on the electrical properties of un-doped ZnO and Al-doped ZnO thin films on a glass substrate. They found that the resistivity of aluminum-doped ZnO increases with increasing substrate temperature. A similar case is encountered in the work by Kim et al. [20]. Here Ti-B-Al-O thin films were studied using the same sputtering technique and aluminum substrate. In this work they revealed that when substrate temperature increased, the grains became bigger, porosity decreased and the electrical resistance lowered.

In a work done by Sirghi, et al. [21], deposition of titanium dioxide thin films on polymethyl methacrylate and polycarbonate substrates resulted in buckling of the substrate surfaces. This work revealed that the substrate surface temperature depends on the substrate thickness, discharge power and substrate holder temperature. Their study also concluded that the buckling of polymer substrate surface in the deposition plasma may not be regarded as a temperature driven surface instability, but more as an effect of argon ion bombardment. This work is particularly relevant to this thesis since the intended deposition system encompasses a polymeric substrate and an inorganic thin film.

From these studies, a common characteristic can be observed related to the sputtering parameters that need to be taken into consideration. Namely these parameters are: substrate temperature, sputtering rate, sputtering temperature, discharge power and base pressure.

Moreover, the work performed by Lance [22] is more closely related to this thesis. This study comprises an investigation of highly reflective thin film for microelectromechanical systems (MEMS). In his thesis work he performed a characterization of sputtered thin films with six different commercial targets produced by two different companies. Three of them were Al-Cu with varying copper percent up to 1.5%Cu (Al-0.5%Cu, Al-1%Cu, Al-1.5%Cu), one of Al-2%Cr-1%Cu, one of Al-2%Ti-1%Cu and finally a pure Al target as a comparison. The films resulting from each target were characterized by a variety of optical, electrical, and mechanical techniques to obtain data relating microstructure to the film's reflectivity and mechanical properties. The results showed that copper solute addition generate films that maintain much of the bulk reflectance of pure aluminum while refining surface morphology to create a more specular surface consisting of smaller, more uniform grains.

### **1.1.5. Literature Review Summary**

In closing, each of the discussed articles has had some or major influence in the evolution of this thesis. Many topics were covered from the fabrication of functionally graded material to the fabrication of thin films. One can conclude that aluminum-boron alloys have been considered to have great potential for the aerospace applications because of their excellent characteristics. Their improved mechanical properties along with their light density and their high resistance to wear make them potential candidates for those types of applications. As a consequence, in this thesis those appealing characteristics are applied them to the expanding field of micro-electronics. Such properties could be then used at a micro and nano-scale in an integrated circuit (IC) industry.

Based on this literature review, it can be stated that there is no information about the fabrication of sputtering targets via centrifugal casting, where the graded concentration of particles could permit composite layers with tunable stiffness. In that respect, the originality of this work is apparent as well as its relevancy since most efforts in this area have only been focused on the production of sputtering targets via simple casting methods such as vacuum casting. Also, sputtering targets with aluminum, boride particles and silicon as the constituents cannot be found in the market while there is no available information about their characterization and performance in thin films. Moreover, this thesis has an additional impact on the reduction of the production cost of the target because of the processing technique used and the low cost of aluminum compared to platinum, titanium, chrome, gold, and copper (main constituents in the IC) without significant reduction on desired properties such as high thermal and electrical conductivities. In addition, the combination of the fabricated target and the polymer substrate will give the polymer the stiffness, hardness and elastic modulus necessary to be used in electronic applications. This thesis has a double impact on modern technology because the

fabricated material is inherently multifunctional as it can be used in two completely different fields, aerospace as well as electronics at the macro, micro and nanoscale.

## **1.2. Objectives**

The main goal for this research is the fabrication via centrifugal casting and characterization of aluminum matrix composite targets for a sputtering system. The dimension of the targets is restricted by the geometry of the holder of the AJA® sputter machine. The dimensions of the target holder are 2" wide and 0.25" thick. To manufacture targets with these dimensions requires precise modification of almost all the parameters of the centrifugal casting. As a consequence, the following specific objectives have been established:

- Determination of the strengthening effect of varying levels of B forming  $\text{AlB}_2$  and  $\text{AlB}_{12}$  particles in an aluminum matrix.
- Characterization of the bulk and the centrifugally cast material
- Preliminary studies of the sputter deposition using the fabricated targets.

## Chapter 2: Background

---

### **2.1. Introduction**

In this Chapter, the reader will find the background theory relevant to this thesis, beginning with a basic definition of composites and some of their pertinent characteristics. This is followed by a description of metal matrix composites, aluminum matrix composites and their advantages. Additionally the reader will find a brief discussion of the phase diagrams of the constituents used in this thesis, beginning with Al-Si system, followed by the Al-B, B-Si and Al-B-Si systems. Furthermore, a brief introduction of functionally graded materials (FGMs), thin films and physical vapor deposition will also be discussed because of their relevance to this thesis.

### **2.2. Composites Description**

In order to understand what a metal matrix composite (MMC) is, it is important to introduce first here a definition of composites. A composite is a material that consists of constituents produced via a physical combination of pre-existing ingredient materials to obtain a new material with unique properties when compared to the monolithic material properties [23]. In this type of material the constituents retain their identities, that is, they do not dissolve or merge completely into one another. Normally, the constituents can be physically identified and exhibit an interface between one another. Composite materials are classified by: their matrix nature (polymer, ceramic, metal), their reinforcement, which includes the chemical nature (oxides, carbides, nitrides), shape (continuous fibers, short fibers, whiskers, particulates) and orientation, and their processing routes. If well designed, the advantage of a given composite material is that it usually exhibits the best qualities of their constituents and often some qualities that neither the constituent possesses. Some of the properties that can be improved by forming a composite material are: strength, stiffness, corrosion resistance, wear resistance, weight,

fatigue life, temperature-dependent behavior, thermal insulation, thermal conductivity, and acoustical insulation among others.

### 2.3. Metal Matrix Composites (MMCs)

Metal matrix composites, like all composites, consist of at least two chemically and physically distinct phases, suitably distributed to provide properties not obtainable with either of the individual phases, e.g., a fibrous or particulate phase, distributed in metallic a matrix [24]. MMCs combine into a single material a metallic base with a reinforcing constituent, which is usually non-metallic and is commonly a ceramic. Like their polymer matrix counterparts, these composites are often produced by combining two pre-existing constituents (e.g. a metal and a ceramic fiber). Metal matrix composites can be classified in various ways. For instance, one can consider the type and contribution of reinforcement components in particle-, layer-, fiber- and penetration composite materials as shown in Figure 1. Fiber composite materials can be further classified into continuous fiber composite materials (multi- and monofilament) and short fibers or, rather, whisker composite materials, as seen in Figure 2.

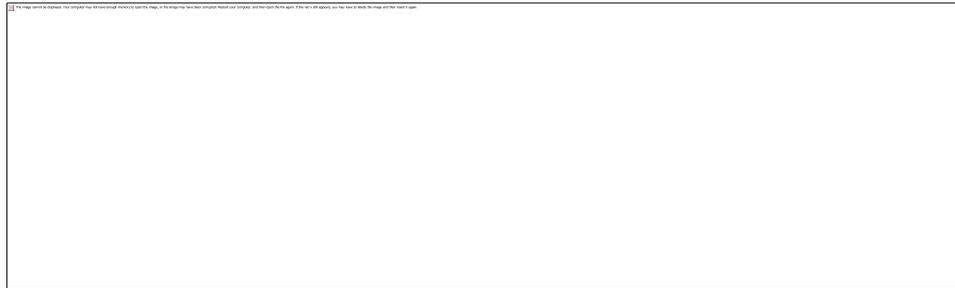


Figure 1 Classification of composites material with metal matrix.

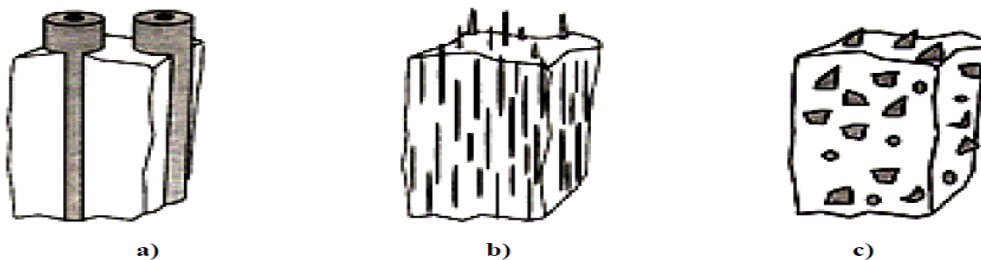


Figure 2 Schematic illustration of the reinforcement type about MMC: a) long unidirectional fiber; b) short fiber and whiskers; c) particles [25].

MMCs offer, therefore, a range of advantages that are important for their selection and use as structural materials. Some features include the combination of high strength, high elastic modulus, high toughness and impact resistance, low sensitivity to changes in temperature or thermal shock, high surface durability, low sensitivity to surface flaws, high electrical and thermal conductivity, and minimum exposure to the potential problem of moisture absorption resulting in environmental degradation, and improved fabricability with conventional metal working equipment [26].

## **2.4. Aluminum Matrix Composites (AMCs)**

Aluminum is the most popular matrix for MMCs. This is because Al alloys have low density, their capability to be strengthened by precipitation, their good corrosion resistance, high thermal and electrical conductivity, and high damping capacity [27]. Aluminum matrix composites (AMCs) offer a large variety of mechanical properties depending on the chemical composition of the Al-matrix. They are usually reinforced by  $\text{Al}_2\text{O}_3$ , SiC and C but  $\text{SiO}_2$ , B, BN,  $\text{B}_4\text{C}$ , AlN may be considered. The aluminum matrices are in general Al-Si, Al-Cu, 2xxx or 6xxx alloys [17]. Their isotropic mechanical properties (higher than their unreinforced alloys) and their low costs (cheap processing routes and low prices of some of the discontinuous reinforcement such as SiC particles or  $\text{Al}_2\text{O}_3$  short fibers) make them very attractive.  $\Delta$

## **2.5. Aluminum-Silicon System**

Aluminum-silicon alloys form a eutectic at approximate 12.6 wt.% silicon, the eutectic temperature being 577 °C as shown in Figure 3. This represents a typical composition for a casting alloy because it has the lowest possible melting temperature. For this reason Al -12 wt.%Si alloys are common. Silicon has a very low solubility in aluminum and it therefore

precipitates as virtually pure silicon, which is hard and hence improves the abrasion resistance [28].

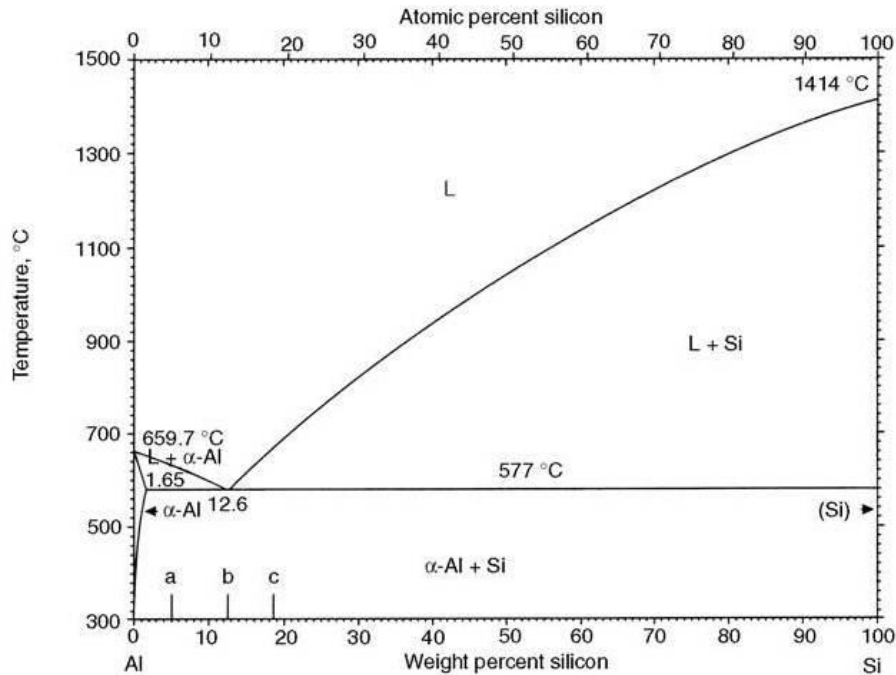


Figure 3 Aluminum-silicon equilibrium phase diagram [16].

During solidification of hypoeutectic Al-Si alloys the first phase to form is  $\alpha$ -aluminum as shown in Figure 4. The  $\alpha$ -aluminum solid solution is the matrix of aluminum-silicon alloys. Cooling from the liquid phase the alloy crystallizes into non-faceted dendrites when the liquidus temperature is reached. Silicon diamond cubic structure with the atoms bonded covalently [16]. Solidification occurs over a temperature range (mushy zone) and it is completed at the eutectic temperature 577 °C. Figure 4 also shows a section of the aluminum-silicon phase diagram in which presents the microstructure at the different stages of temperature and composition of aluminum-silicon alloys. The chemical compositions of these different stages are: hypoeutectic 1.65-12.6 wt.% Si, eutectic 12.6 wt.% Si and hypereutectic >12.6wt.% Si.

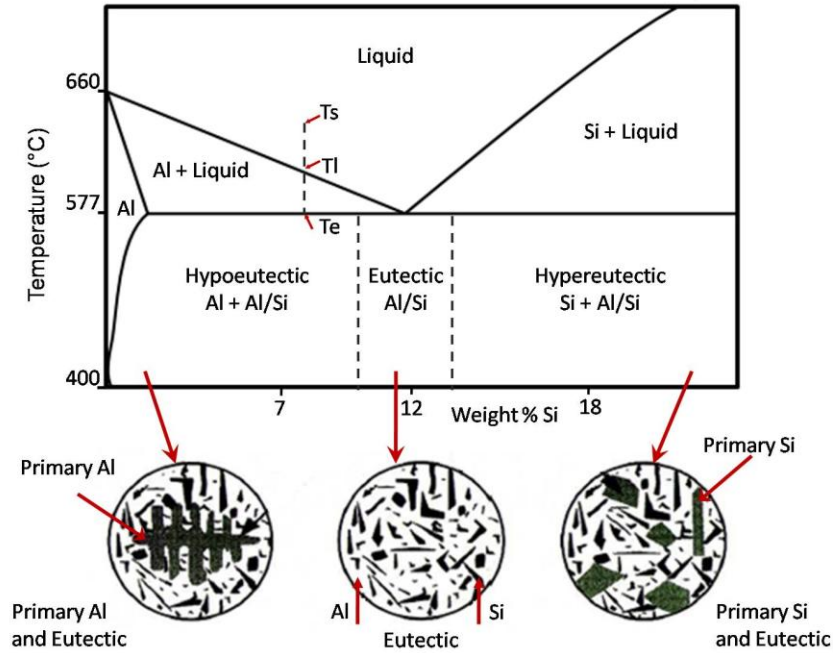


Figure 4 Aluminum-silicon phase diagram and microstructure (amended from [25]).

Some advantages of binary aluminum-silicon alloys (pertinent to this thesis) are that they exhibit excellent fluidity, castability, and corrosion resistance. Also these alloys display low strength and poor machinability. The strength, ductility, and castability of hypoeutectic aluminum-silicon alloys can be further improved by modification with the addition of Na or Sr to the aluminum-silicon eutectic. Aluminum-silicon alloys exhibit low specific gravity and coefficients of thermal expansion [17].

## 2.6. Aluminum-Boron System

The Al-B system has been the object of debates with respect to the equilibrium phases at room temperature. Studying thermal behavior of this system, at least seven invariant temperatures has been proposed [29]. From the equilibrium phase diagram of Al-B system shown in Figure 5 it can be concluded that there is some agreement that the stable solid phases are  $\beta$ B,  $\alpha$ AIB<sub>12</sub>,  $\beta$ AIB<sub>12</sub>, AIB<sub>10</sub>, AIB<sub>2</sub> and Al. Experimental evidence leads to the conclusion that AIB<sub>2</sub> and  $\alpha$ AIB<sub>12</sub> are the only true binary aluminum boride compounds that could be present at room temperature [29]

AIB<sub>2</sub> has a hexagonal close packed hp3 crystal structure with lattice parameters:  $a = 0.3006$  nm and  $c = 0.3252$  nm, whereas AIB<sub>12</sub> has a complex tetragonal crystal structure with  $a = 1.0161$  nm and  $b = 1.4238$  nm. Boron and aluminum atoms occupy alternative honeycomb layers in the hexagonal AIB<sub>2</sub> crystals [30]. The melting points of AIB<sub>2</sub> and AIB<sub>12</sub> were reported as  $1655 \pm 50$  °C and  $2163 \pm 50$  °C, respectively [31]. Other Al-B compounds, such as AIB<sub>12</sub> and AIB<sub>10</sub>, were also reported, but they were later proved to be metastable or ternary compounds that are stabilized by small amount of impurities [32].

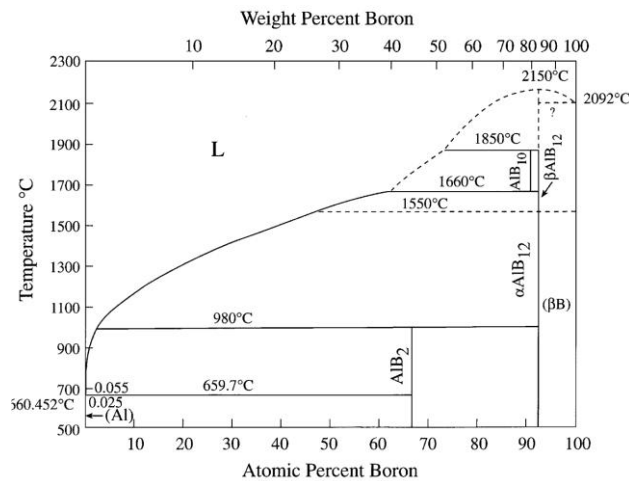


Figure 5 The Al-B binary phase diagram [29].

## 2.7. Aluminum – Boron – Silicon Systems

Very small additions of boron to Al–Si alloys lead to the precipitation of aluminum borides. At the Al–Si eutectic liquid, an addition of about 0.01 wt.% B is sufficient for this effect. This is the dominant feature of the presented Al–B–Si phase diagram section at 0.1 wt.% B, shown in Figure 6. It shows the binary Al–Si diagram with just the additional  $\text{AlB}_2$  as the equilibrium phase. The other boride,  $\text{AlB}_{12}$ , precipitates from the liquid at high temperature and high Si content. It is unimportant if boron in Si–1% B is in solid solution with Si or present as  $\text{SiB}_3$ . By contrast, Figure 6 shows that the typical homogenization temperature of 800 °C [33] is close to the saturation limit of the borides, resulting in a small driving force for the dissolution of borides introduced with an Al–B master alloy and, thus, a slow dissolution. Figure 6 also indicates that  $\text{AlB}_2$  is the most stable boride in that range, it is suggested that  $\text{AlB}_{12}$  may be formed due to kinetic reasons.

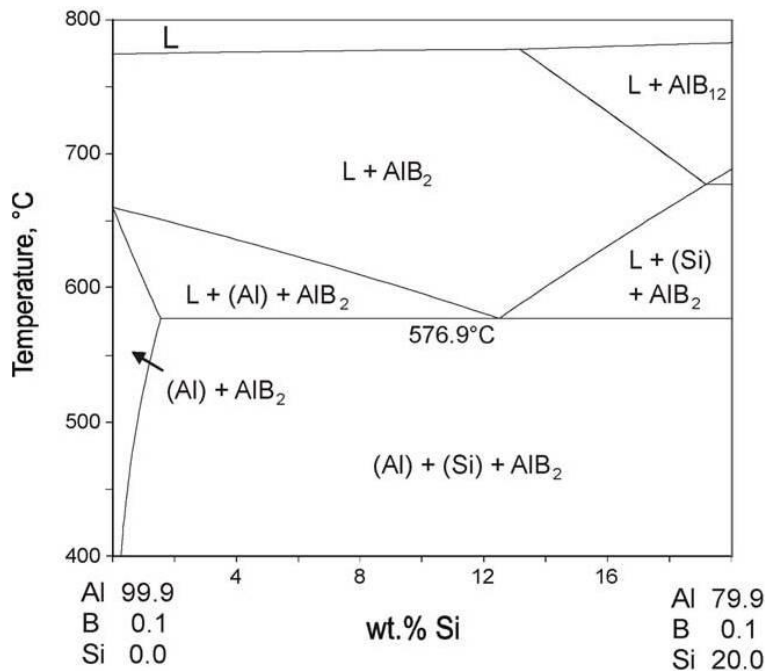


Figure 6 Calculated vertical section in the Al–B–Si system at constant 0.1 wt.% B. The ternary eutectic liquid composition is 12.5 wt.% Si and only 0.01 wt.% B; the temperature is 0.1C below the 577.0 °C of the binary Al–Si eutectic [34].

## **2.8. Functionally Graded Materials (FGMs)**

FGMs are a new generation of engineered materials wherein the microstructure features are spatially varied through non-uniform distribution of the reinforcement phase(s). In order to accomplish this, engineers use reinforcements with different properties, sizes, and shapes, as well as by interchanging the roles of the reinforcement and matrix phases in a continuous manner [35]. The result is a microstructure that results in continuously or discretely changing thermal and mechanical properties at the macroscopic or continuum scale, as seen in Figure 7. This new concept of engineering the microstructure marks the beginning of a revolution both in the materials science and mechanics of materials areas since it allows one, for the first time, to fully integrate the material and structural considerations into the final design of structural components.

As mentioned above FGMs feature gradual compositional variation from high concentration of particles at one end to almost pure metal at the other, leading to exclusive advantages of smooth transition in thermal stresses across the thickness. Also FGMs can be used to avoid problems associated with the presence of an interface in a material: stress singularities due to elastic or thermal property mismatch, poor adhesion, or unwanted reflections at the interface [36]. They can also serve to introduce a designed property profile into a material providing an optimum response to an external field in functional applications.

There are numerous methods to reach the functionally graded properties [37]. One of them was developed by Fukui [38], where a centrifugal force is used for segregating the particles. If the reinforcement particles possess higher density compared to the density of the molten matrix, those particles move assisted by centrifugal forces along the radial direction (Figure 7). This is, probably the most cost-effective and attractive processing route to fabricate a FGM. The extent

of segregation depends on diverse processing parameters as well as cast geometry: pouring temperature of the melt, solidification time, rotational speed, and density difference between reinforcement particles and matrix.

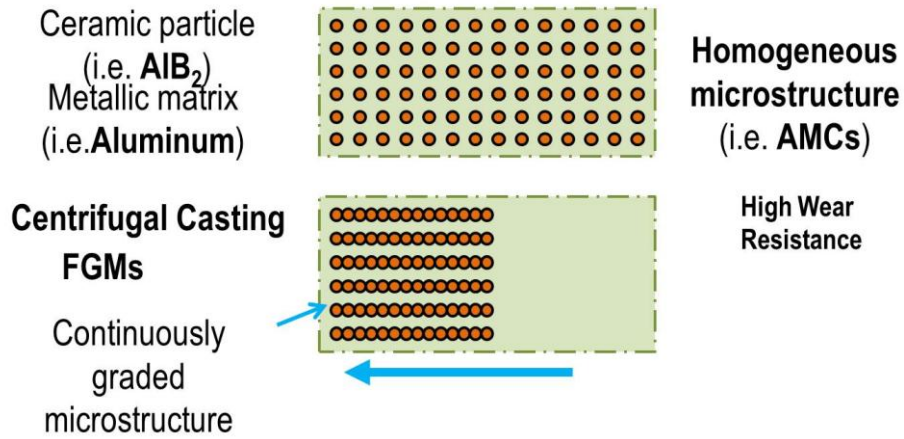


Figure 7 Schematic of FGM microstructure before and after centrifuging.

## **2.9. Physical Vapor Deposition (PVD)**

PVD processes are atomistic deposition process in which a material is vaporized from a solid or liquid source in the form of atoms or molecules, transported in the form of a vapor through a vacuum or low pressure gaseous environment to the substrate where it condenses [39]. Typically PVD processes are used to deposit films which thickness in the range of a few nanometers to thousands of nanometers additionally, they can be used to form multilayer coatings, graded composition deposits, very thick deposits and freestanding structures. The substrates can range in size from very small to very large such as the 10' x 12' glass panels used for architectural glass. The substrates can range in shape from flat to complex geometries such as watch bends and tool bits. Typical PVD deposition rates are 1-100 Å per second.

Moreover, a PVD process can be used to deposit films of elements and alloys as well as compounds using reactive deposition processes. In reactive deposition processes, compounds are formed by the reaction of depositing material with the ambient gas environment such as nitrogen (e.g. titanium nitride, TiN) or with a co-depositing material (e.g. titanium carbide, TiC). Quasi-reactive deposition is the deposition of films of a compound material from a compound source where loss of the more volatile species or less reactive species during the transport and condensation process, is compensated for by having a partial pressure of reactive gas in the deposition environment. One example is the quasi-reactive sputter deposition of ITO (indium-tin-oxide) from an ITO sputtering target using a partial pressure of oxygen in the plasma. The main categories of PVD processing are vacuum evaporation, ion plating, and sputter deposition. A brief description of these PVD process is presented in the next paragraphs.

### 2.9.1. Vacuum deposition

Vacuum deposition is a PVD process in which the material from a thermal vaporization source reaches the substrate with little or no collision with gas molecules in the space between the source and substrate as shown in Figure 8. The trajectory of the vaporized material is “line-of-sight” which may lead to undesirable “shadow effects”. Typically, vacuum deposition takes place in the gas pressure range of  $10^{-5}$  Torr to  $10^{-9}$  Torr depending on the level of gaseous contamination (and potential contamination) that can be tolerated in the deposition system. Vacuum deposition is used to form optical interference coatings, mirror coating, decorative coatings, permeation barrier films on flexible packaging materials, electrically conducting films, wear resistance coatings, and corrosion protective coatings.

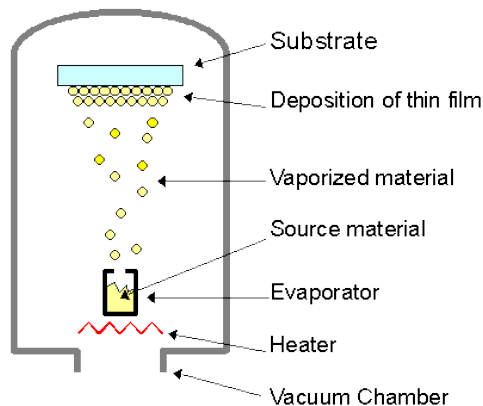


Figure 8 Schematic of the vacuum deposition process [40].

### 2.9.2. Ion Plating

Ion Plating is sometimes called ion assisted deposition (IAD) or ion vapor deposition (IVP). It utilizes concurrent or periodic bombardment of the depositing film by atomic-sized energetic particles, to modify and control the properties of the depositing film. In ion plating the energy, flux and mass of bombarding species along with the ratio of bombarding particles to depositing

particles are important processing variables. Ion plating is used to deposit hard coatings of compound materials, adherent metal coatings, optical coatings with high densities, and conformal coatings on complex surfaces. Figure 9 shows a schematic of the ion plating process.

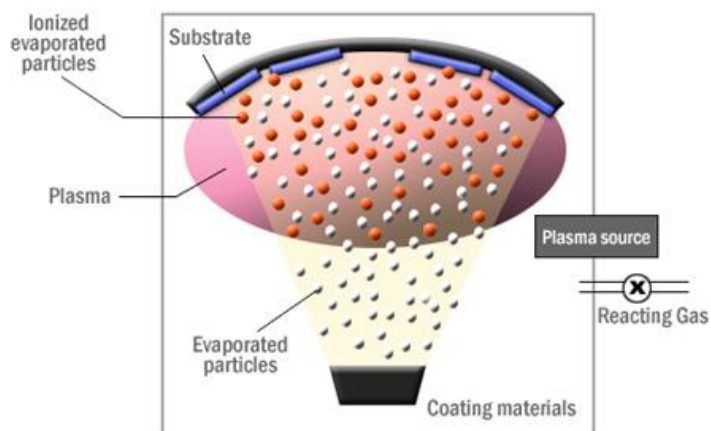


Figure 9 Schematic representation of the ion plating process [41].

### 2.9.3. Sputter Deposition

Sputter deposition is the deposition of material vaporized from a surface (target), by the physical sputtering process. Physical sputtering is non-thermal vaporization process where surface atoms are physically ejected from a solid surface by momentum transfer from an atomic-sized energetic bombarding particle. This is usually a gaseous ion accelerated from a plasma cloud [39]. Generally the source-to-substrate distance is short compared to vacuum deposition. Sputter deposition can be performed by energetic ion bombardment of a solid surface (sputtering target) in a vacuum using an ion gun or low pressure plasma (<5 mTorr) where the sputtered particles suffer few or no gas phase collisions in space between the source and the substrate. In other words, sputtering is a deposition technique that uses energetic ions, typically  $\text{Ar}^+$ , to bombard a material target. In the process, atoms are knocked loose from the surface of the target and are transported to the substrate, where deposition occurs. Electrically conductive

materials, such as aluminum in the present thesis, typically use a DC power source, in which the target acts as the cathode in a diode system [39]. Sputtering of dielectrics, such as ceramic materials (in this thesis, aluminum diboride  $AlB_2$  and aluminum dodecaboride  $AlB_{12}$ ), requires an RF power source to supply energy to the argon atoms. Figure 10 shows a schematic of sputter deposition with a DC plasma.

Sputter deposition is widely used to deposit thin film metallization on semiconductor material, coatings on architectural glass, and reflective coatings on compact disc, magnetic films, dry film lubricants and decorative coatings. For the present thesis sputter deposition will be the technique of choice for depositing thin films.

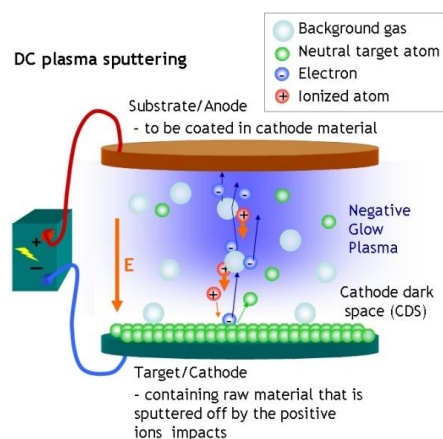


Figure 10 Schematic representation of sputtering process using a DC source [42].

## 2.10. Thin Film Technology

Thin films are deposited onto bulk materials (substrates) to achieve properties unattainable or not easily attainable in the substrates alone. They can be achieved by depositing multiple layers of different materials. Multilayer thin films can behave as completely new, engineered materials unknown in bulk form. When multiple layering is combined with lithographic patterning in the plane of the films, microstructures of endless variety can be constructed. This is the basis of technology of the integrated-circuit industry, and more recently it is being applied to optical

waveguide circuitry and to micromechanical devices [43]. Some applications for thin film are shown in Table 1. Examination of this table shows that the range of thin film applications is very broad.

Table 1 Thin Film Applications [43].

Thin film property category	Typical Application
<b>Optical</b>	Reflective/antireflective coatings, interference filters, decoration (color, luster), memory discs (CDs) and waveguides
<b>Electrical</b>	Insulation, conduction, semiconductor devices, and piezoelectric drivers
<b>Magnetic</b>	Memory discs (CDs)
<b>Chemical</b>	Barriers to diffusion or alloying, protection against oxidation or corrosion and gas/liquid sensors
<b>Mechanical</b>	Tribological coatings, hardness, adhesion and micromechanics
<b>Thermal</b>	Barrier layers and heat sink

### 2.11. Microstructure of Aluminum Thin Films

Pure aluminum thin films demonstrate outstanding reflectivity, over 90% throughout the visible spectrum [44]. It has both high thermal and electrical conductivity. However pure aluminum has several undesirable mechanical characteristics. These include low hardness, no true endurance limit, and poor high temperature operation. This leads to poor wear resistance and fatigue.

Sputtered aluminum typically has a polycrystalline structure comprised of crystalline grains separated by grain boundaries of differing composition and orientation [45]. Aluminum has a face-centered cubic structure. The grains in sputtered aluminum have a preferred (111) crystal orientation normal to the substrate surface. The structure of an Al thin film can be described by the standard zone diagram (SZD), shown below in Figure 11 [46]. The SZD relates temperature

and process pressure for a metallic coating. Sputtered films typically reside in either Zone 1 or Zone T. Zone 1 consists of fibrous, but porous, films that typically demonstrate tensile stress. Grains are columnar, but separated by voids. Zone T films are hard, dense, and fibrous in nature [46]. The resultant film texture primarily determines the resultant optical, mechanical, and electrical properties of the film system. Research has shown that microstructure-dependant film properties are affected by the underlying film topography [47, 48], residual gas content [48, 49], film surface roughness[44, 46], and most important from a material design standpoint, alloying constituents [45, 47, 50].

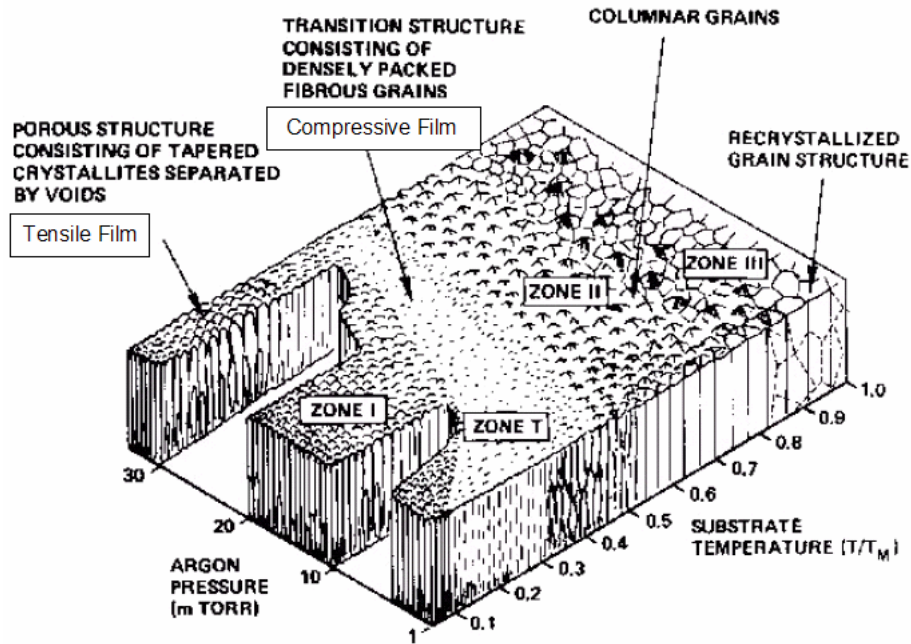


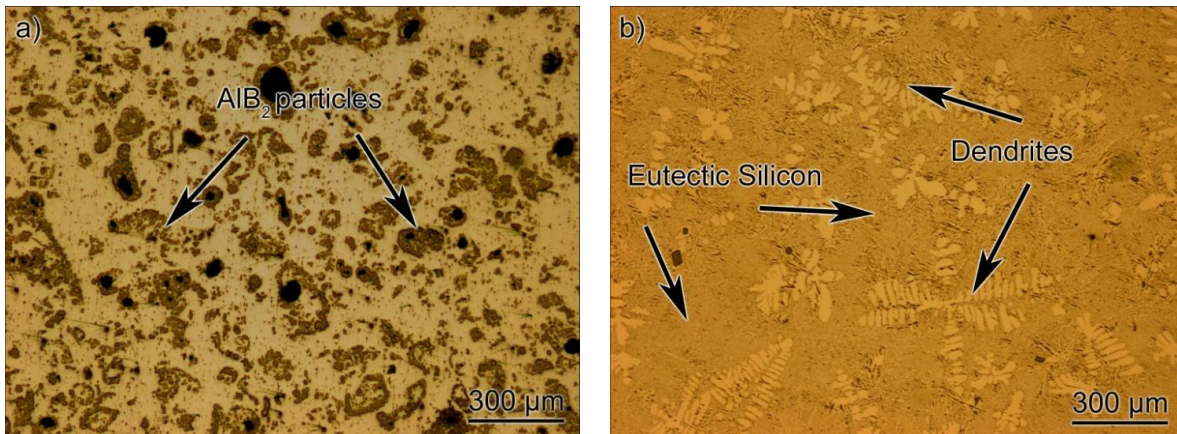
Figure 11 Standard Zone Diagram for Metallic Thin Films [46].

## Chapter 3: Methodology of Fabrication and Characterization of Sputtering Targets

---

### 3.1. Material Description

The Al-B-Si composites were prepared using three Al master alloys. First, two Al-B master alloys were utilized both containing 5wt%B: one had boron in the form of  $\text{AlB}_2$  and the other one,  $\text{AlB}_{12}$  particles. Silicon was provided by a binary Al - 12 wt.% Si, i.e. eutectic composition to facilitate melting and mixing. In addition 99% pure aluminum helped set up the balance.  $\text{AlB}_2$  and  $\text{AlB}_{12}$  particles (contained in the Al-B master alloys) were used as reinforcements in the fabrication of the specimens; they had a density of  $3.2 \text{ g/cm}^3$  and  $2.55 \text{ g/cm}^3$ , respectively [13], accompanied by high melting point of  $1655$  and  $2214^\circ\text{C}$ , respectively [7]. Figure 12a-d show the micrographs of the as-received master alloys used for this thesis. The composite chemical compositions listed in Table 2 were produced.



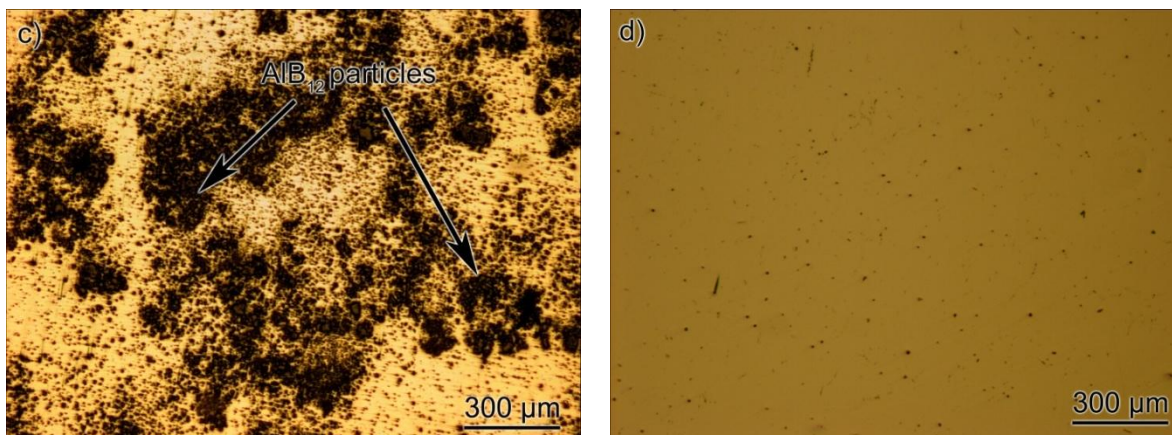


Figure 12 Optical micrographs of the materials used; a) Al-5wt%B<sub>2</sub> b) Al-12wt%Si c) Al-5wt%B<sub>12</sub> d) Pure aluminum.

Table 2 Chemical Composition of Cast Composites

Composite Composition	Mass Al-5wt%B <sub>2</sub> (g)	Mass Al-5wt%B <sub>12</sub> (g)	Mass Al-12wt%Si (g)	Pure Aluminum Addition (g)	Total Mass (g)
Al-2wt.%B <sub>2</sub> -3wt.%Si	80	0	50	70	200
Al-3wt.%B <sub>2</sub> -3wt.%Si	120	0	50	30	200
Al-2wt.%B <sub>12</sub> -3wt.%Si	0	80	50	70	200
Al-3wt.%B <sub>12</sub> -3wt.%Si	0	120	50	30	200

### 3.2. Fabrication of Sputtering Targets

For the fabrication of the sputtering targets two casting techniques were selected: centrifugal casting and conventional vacuum casting. From Chapter 2 it is known that centrifugal casting processes can create a material with a good segregation of particles, meaning that several sputtering targets can be obtained in just one centrifugal process. On the other hand, the conventional vacuum process was performed in order to get a homogenous segregation of particles and to be used as control samples for comparison reasons. From the compositions listed in Table 2 a total of sixteen specimens were fabricated by two casting processes. In the following sections all fabrication processes of the sputtering targets are discussed.

### **3.2.1. Description of the Centrifugal Caster**

Eight samples were fabricated using a centrifugal casting machine with a variable speed mechanism, which allows adjusting the rotational velocity from 300 rpm to 550 rpm. The machine also has a screen timer where the casting time for the casting can be varied. Time and rotational velocity are to be set experimentally depending on the sample needs and based on prior research [6]. A schematic representation of the graphite mold is shown in Figure 13 and the position of the transfer scoop and the mold are shown in Figure 14. The ceramic scoop weighs 340g and was used to transfer a charge of 200g into the cylindrical graphite mold. The distance of the cylinder close end to the axis of rotation is 200mm and the distance of the cylinder outer end from the rotation axis is 250mm. The arm is used to balance the lever carrying the mold and the scoop during the centrifugal casting process. The composite consisting of an Al molten matrix containing solid boride particles was poured into the scoop and then subject to the centrifugal forces resulting from constant rotational velocity along a fixed translational axis. The centrifugal casting machine rotates in a counter-clockwise motion. (top view in Figure 14) The centrifugal casting parameters used are summarized in Table 3.

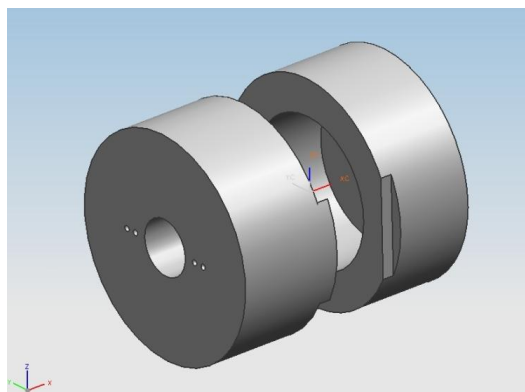


Figure 13 CAD model of graphite mold.

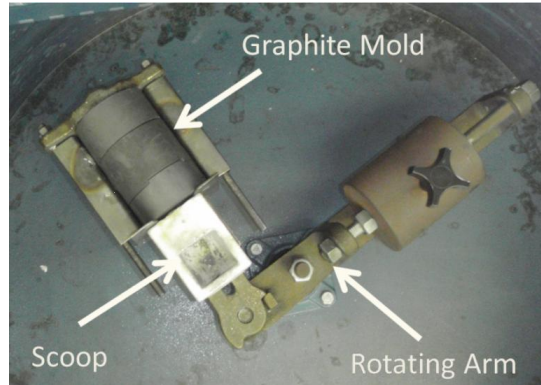


Figure 14 Top view of the centrifugal caster.

Table 3 Centrifugal Casting Parameters.

Mass (g)	Mold Material	Mold Temperature (°C)	Melting Temperature (°C)	Acceleration time (s)	Rotational Velocity (rpm)
200	graphite	400	750	10	350

### 3.2.2. Description of the Vacuum Equipment

For comparison purposes, eight sputtering targets were also fabricated via conventional vacuum casting as control specimens. The equipment used is almost the same as for gravity casting, the only difference being that the solidifying specimens are subject to a negative pressure set to 101.6 kPa, applied for 30 minutes. The other parameters such as mold material, melting temperature and mass were the same as those used for the centrifuged samples. The effects of the vacuum pressure were not the focus of the project so they were not analyzed and homogenous particle segregation was assumed. Figure 15 shows the equipment used for the control samples. It is important to mention that the equipment was adapted to ensure the vacuum at the chamber at a temperature of 700°C. This adaptation includes the housing, high temperature rubber and vacuum silicon grease. The housing material is silica and was also fabricated in UPRM laboratories.



Figure 15 Front view of the adapted vacuum equipment.

### 3.3. Experimental Procedure

Once the target specimens were fabricated via the two casting process, they followed several steps for metallographic preparation and analysis, as described in Figure 16. The flow chart includes all the steps to complete the experimental segment, fabrication and characterization of the bulk material. The following sections include a brief description of each step in this flowchart of experimental procedure.

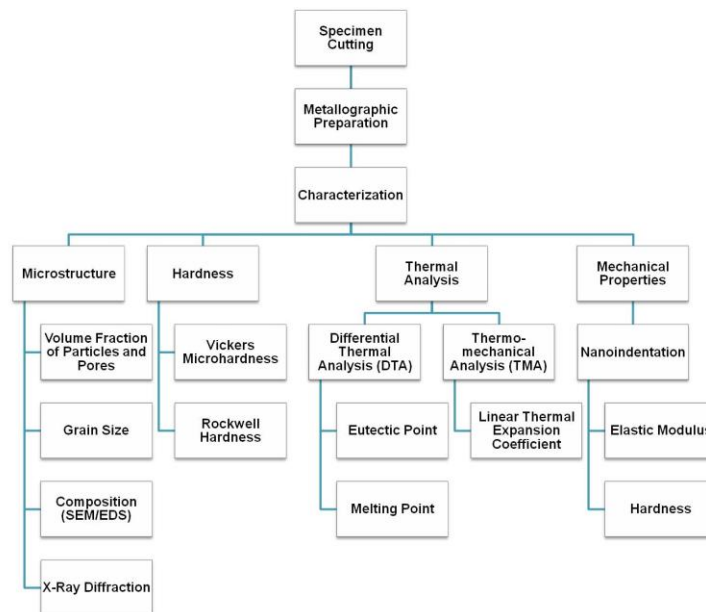


Figure 16 Flow chart of experimental procedure of the bulk material.

### **3.3.1. Specimen Cutting and Sample Dimensions**

Adequate precision in the sample dimensions is one of the most important parameters when fabricating sputtering targets. For this reason and to avoid excessive material loss, the cutting process was performed using wire electrical discharge machining (WEDM). In WEDM a thin single-strand metal wire, usually brass, is fed through the workpiece, submerged in a tank of dielectric fluid, typically deionized water [51]. WEDM is typically used to cut plates as thick as 300mm and to make punches, tools, and dies from hard metals that are difficult to machine with other methods. The wire, which is constantly fed from a spool, is held between upper and lower diamond guides. The guides, usually CNC-controlled, move in the x-y plane. The wire diameter can be as small as 20  $\mu\text{m}$  and the geometry precision is not far from  $\pm 1 \mu\text{m}$ . The wire-cut process uses water as its dielectric fluid, controlling its resistivity and other electrical properties with filters and de-ionizer units. The water flushes the cut debris away from the cutting zone. Flushing is an important factor in determining the maximum feed rate for a given material thickness [51].

The specimens obtained by the process of centrifugal casting were cut according to the three sections indicated in Figure 17, where the sample dimensions and the centrifugal direction are also shown. In this figure, zone 1 (highest particle segregation) is the outermost sample, zone 2 is transitional and zone 3 (particle-depleted matrix) being the closest to the center of rotational axis. Characterization was performed on the outer faces (with respect to the centrifugal force) of the cut specimens. The specimens obtained via vacuum casting were also cut this way, but they were not identified by zone because, as mentioned earlier, it was assumed that they have a homogenous segregation of particles and they were characterized as one zone.

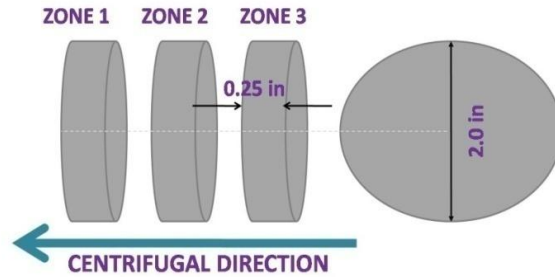


Figure 17 Sample cutting and dimensions with respect to the applied centrifugal force.

### 3.3.2. Metallographic Preparation

Grinding was carried out in all samples with a series of 320, 400, 600, 800 and 1200 grit SiC paper using water as the coolant/lubricant. Polishing was completed using 3  $\mu\text{m}$  monocrystalline diamond suspension and lubricant on a short felt cloth followed by final polishing with a 0.05  $\mu\text{m}$  colloidal silica suspension on short felt cloth. For the metallographic preparation a Buehler Beta manual grinder/polisher was used.

### 3.4. Characterization of Specimens

The physical and/or microstructure evaluations of the fabricated materials were performed using a combination of microscopy techniques with X-ray diffraction. This is described in the next sections.

#### 3.4.1. Microstructure Analysis

The microstructure analysis of these composites was performed using a Nikon Epiphot 2 inverted optical microscope with 5x, 10x, 20x, 50x and 100x objective lenses and differential interferometry contrast (furnished with Nomarski filters). A high resolution digital camera allowed obtaining images that were analyzed using *Image J* public domain package [52]. Thus, a complete microstructure characterization of each sample was completed and involved

measurement of particles volume percent, porosity and the matrix ASTM grain size. Volume percent of the silicon phase, and  $\text{AlB}_2$  and  $\text{AlB}_{12}$  particles were measured from images taken at 100x, using ImageJ.

In order to verify the components present in the composite, a scanning electron microscope (SEM) and energy dispersive X-ray spectrometry (EDS) and X-Ray diffraction were used. Finally, to find the average grain size the samples were etched with 10% NaOH water solution as described in ASTM E340-00<sup>63</sup> for aluminum alloys. The optimal etching time was found to be 35 seconds. Grain size (G) measurement follows the *Intercept Procedure* described in the ASTM Standard E112-96<sup>63</sup>.

### 3.4.2. Hardness

#### 3.4.2.1. Rockwell Hardness

The ASTM standard test method for 15T Rockwell superficial hardness of metallic materials is issued under the fixed designation E 18-07. For the present thesis we selected the 15T Rockwell superficial hardness test; this method uses a 1.588 mm stainless steel ball indenter with a maximum force of 147 N. The LECO Rockwell LR-50 hardness tester in Figure 18 was used to produce a total of forty evenly spaced indentations on each sample.



Figure 18 LECO Rockwell LR-50 hardness tester.

### **3.4.2.2. Vickers Microhardness**

The Vickers hardness test method consists in indenting the test material with a diamond indenter, in the form of a right pyramid with a square base and 136° angle between opposite faces of the tip. The ASTM E 384 standard test method was utilized to determine the Vickers microhardness of the composite matrix. The load and loading time were 490.3 N and 15 seconds respectively. Microhardness measurements were made exclusively on the matrix of the Al-B-Si composite specimens: this means that each indentation avoided hitting the boride particles. A total of twenty evenly spaced indentations were made on each sample. The equipment used here is shown in Figure 19.



Figure 19 Microhardness Tester.

### **3.4.2.3. Nanoindentation**

Nanoindentation was used to determine the mechanical properties of the component phases of the fabricated composites, more specifically, the properties of the particles and matrix individually. This analysis was performed only over the samples with higher concentration of particles. Nanoindentation measurements were conducted performing multi-load indents, which consisted of 5 to 8 loading segments, each up to a partial load and followed by a hold, and, 5 to 8 unloading segments for each test with a Berkovich diamond tip with a sub 0.01  $\mu\text{m}$  radius.

The indents instrumentation used was a G200 Agilent Nanoindenter (Figure 20) equipped with a scanning probe microscope (SPM) tool and an objective lens of 40x that permits to locate the different zones of the matrix and the boride particles.



Figure 20 Agilent G200 Nanoindenter.

### **3.5.1. Thermal Characterization**

#### **3.5.1.1. Differential Thermal Analysis (DTA)**

A Mettler Toledo TGA/SDTA 851<sup>o</sup> was used to measure the thermal evolution of the composites upon heating and cooling under a nitrogen atmosphere. A 7.6-8.1 mg sample in an alumina crucible with 30 $\mu$ L capacity was used for this analysis in a nitrogen atmosphere with 20 mL/min flow. The heating cycles were carried out at 10 $^{\circ}$ C/min from 25 $^{\circ}$ C to 750 $^{\circ}$ C, followed by a cooling cycle from 750 $^{\circ}$ C to 25 $^{\circ}$ C at -25 $^{\circ}$ C/min. DTA curve provides data on phase transformations (revealed by their thermal signals) that have occurred, including melting and solidification events of the fabricated specimens. Figure 21 shows the equipment used for this task.



Figure 21 Mettler Toledo TGA/SDTA 851<sup>e</sup> equipment.

### **3.5.1.2. Thermomechanical Analysis (TMA)**

A thermomechanical analyzer consisting of a specimen holder and a probe that transmits changes in length to a transducer that translates movements of the probe into an electrical signal was used to measure the coefficient of thermal expansion (CTE) of the fabricated composites. CTE measurements of the fabricated specimens were carried out using a probe force of 0.1 N, at a heating rate of 5 °C /min in the 25 to 200°C temperature range. The “Standard Test Method for Linear Thermal Expansion of Solid Materials by Thermomechanical Analysis” E831-03 was used for this analysis. The instrument was a Mettler Toledo TMA/SDTA 840<sup>e</sup>, shown in Figure 22.

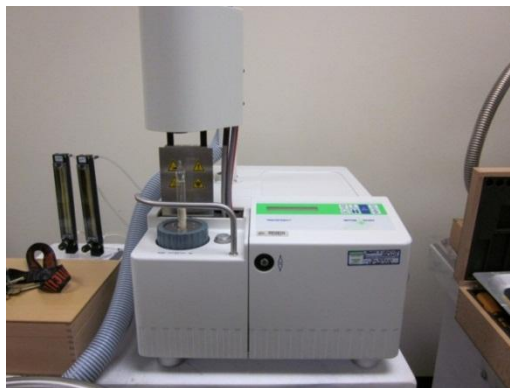


Figure 22 Mettler Toledo TMA/SDTA 840<sup>e</sup>.

## Chapter 4: Results and Discussion

---

### 4.1. Microstructure Analysis

This section is divided in three parts. The first part is dedicated to the microstructure analysis of the vacuum cast and centrifuged samples. This analysis is complemented with electron microscopy and x-ray diffraction studies to confirm the phases present in the composites. The second section is centered in the analysis of the volume percent of particles and pores of the aforementioned specimens by using the image J software. Finally, the third section consists of the analysis on the grain size of each specimen measured following ASTM standards.

The composite matrix is constituted by an Al - 3wt.% Si alloy. Therefore, for the sake of brevity, only the content of boron is reported in the microstructure analyses of the composites. microstructure analysis of the matrix was conducted in vacuum cast samples only for the sake of comparison. In this work the identification of phases was based on the study of the Al-master alloys used in the fabrication of the composites.

#### 4.1.1. Microstructure of Vacuum Cast Specimens

The phases observed in the microstructure of the fabricated specimens are labeled in Figure 23a-b. These representative micrographs were selected to depict the overall appearance of the matrix and to identify the thermodynamically stable phases by comparison with prior research [6-8, 53, 54]. As a result, these micrographs allowed identifying the  $\text{AlB}_2$  and  $\text{AlB}_{12}$  particles. In Figure 23a and Figure 23b show the  $\text{AlB}_2$  and  $\text{AlB}_{12}$  particles clusters, respectively, reinforcing the material while silicon is present in the Al-Si eutectic mixture mainly in the grain boundaries of the composite matrix. The overall appearance of the vacuum cast composite microstructures containing 2 and 3 wt.% $\text{B}_x$  can be observed in Figure 24a through Figure 24d respectively.

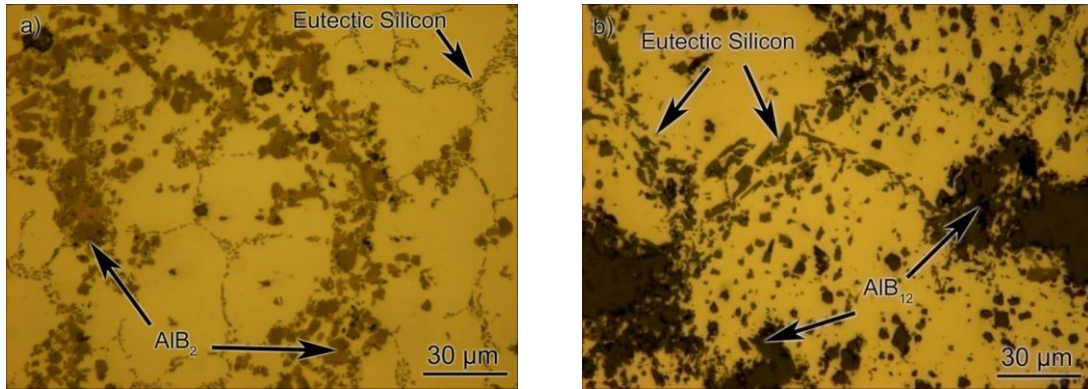


Figure 23 Optical images of composites containing a)  $AlB_2$  particles and b)  $AlB_{12}$  particles.

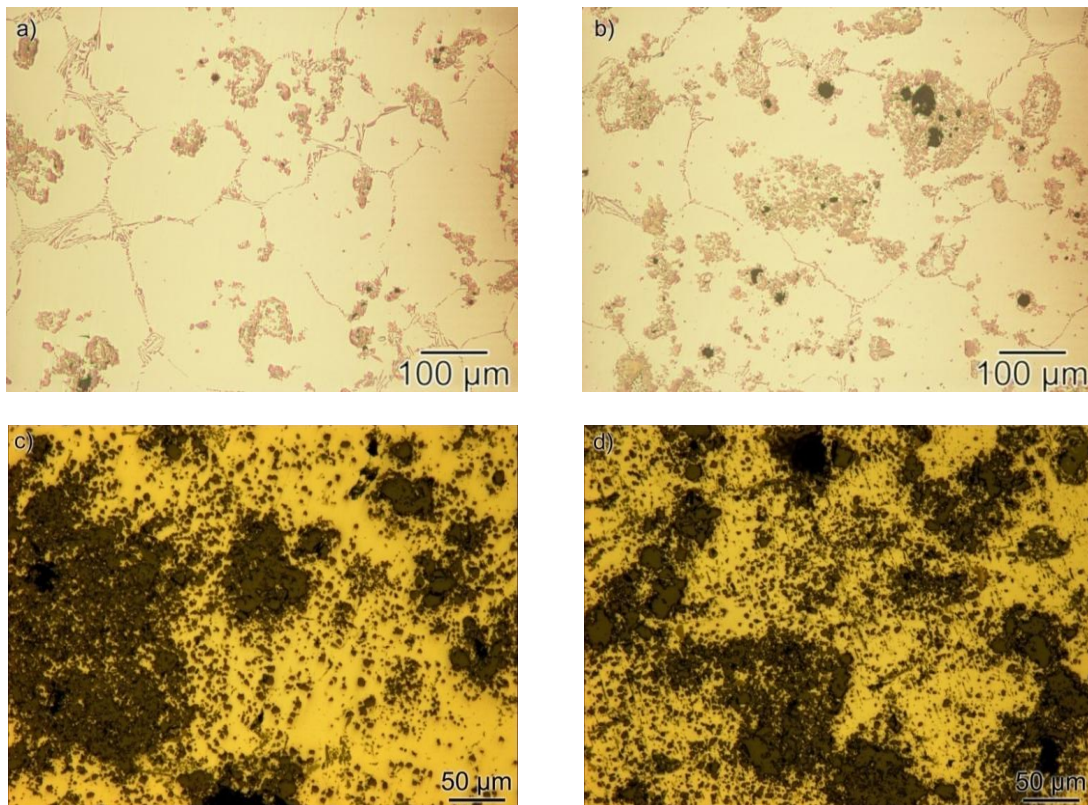


Figure 24 Micrographs of vacuum cast composites with different weight percent of boron a) 2 wt.% $B_2$ , b) 3 wt.% $B_2$ , c) 2 wt.% $B_{12}$  and d) 3 wt.% $B_{12}$ .

#### **4.1.2. Microstructure of Centrifugally Cast Specimens**

The resulting microstructures displaying the composite matrix, the Al-Si eutectic and the boride particles in each zone of the specimens are presented in Figure 25 and Figure 26, respectively. In Figure 25 the increment in the particles volume fraction with the amount of boron in the zone 1 is apparent, as well as in the reinforced areas of the zone 2 (transition) for the specimens containing diboride particles. This occurs because the denser reinforcing particles are segregated by centrifugal forces.

On the other hand, Figure 26 reveals that the specimens containing dodecaboride particles do not present the same trend. In effect, zone 2 is the one with more volume of particles. This unexpected behavior could be attributed to the lower density of  $\text{AlB}_{12}$  particles ( $2.60\text{g/cm}^3$ ) compared with the density of  $\text{AlB}_2$  particles ( $3.19\text{ g/cm}^3$ ) in the molten aluminum matrix (approximately  $2.375\text{ g/cm}^3$ ) [55]. Also, the high thermal conductivity of the graphite mold reduces the solidification time of the centrifugal casting, which could further hamper the movement of the dodecaboride particles under the centrifugal forces.

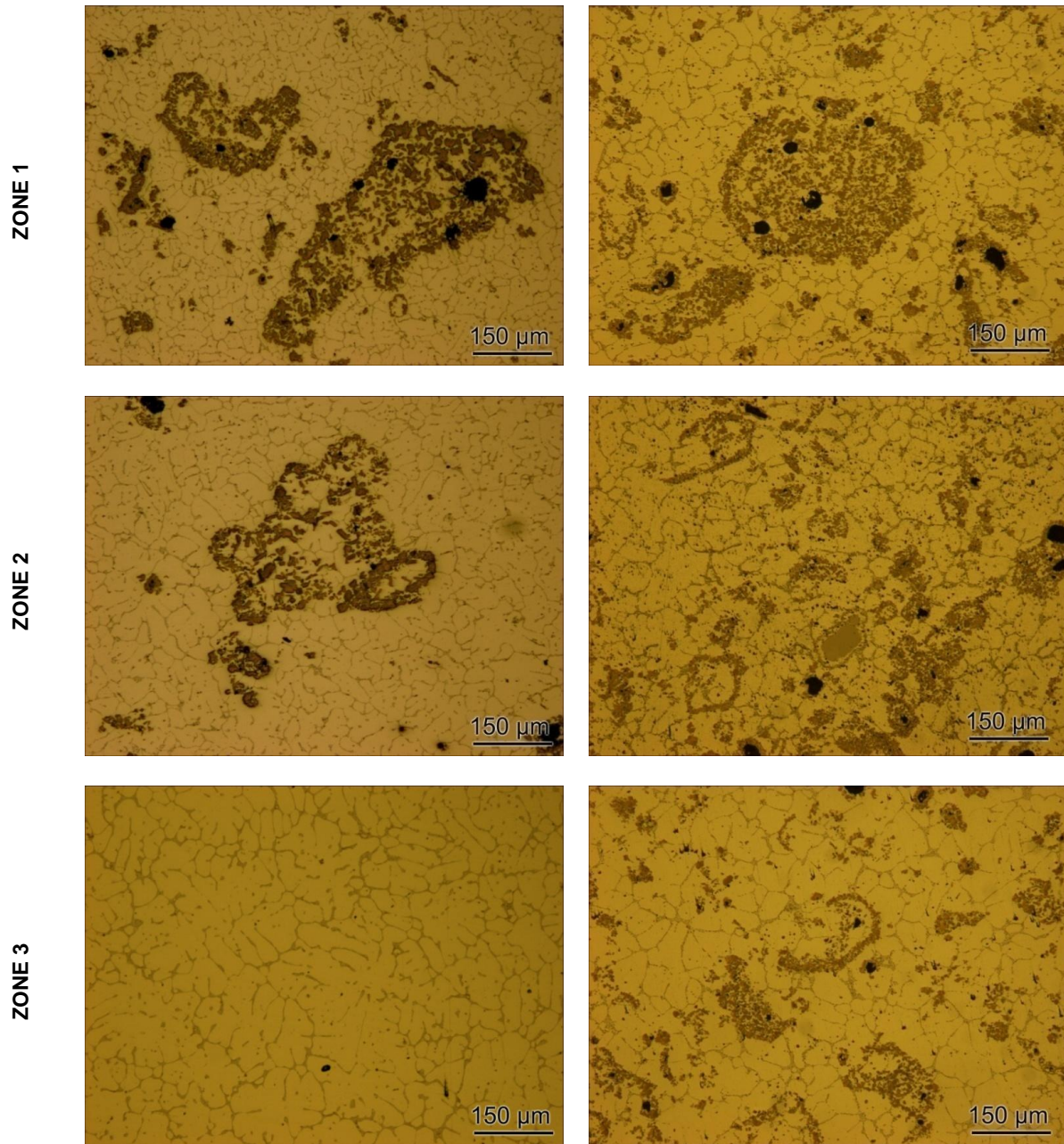


Figure 25 Microstructures of the centrifuged specimens with the three defined zones for samples with different weight percent of diboride particles.

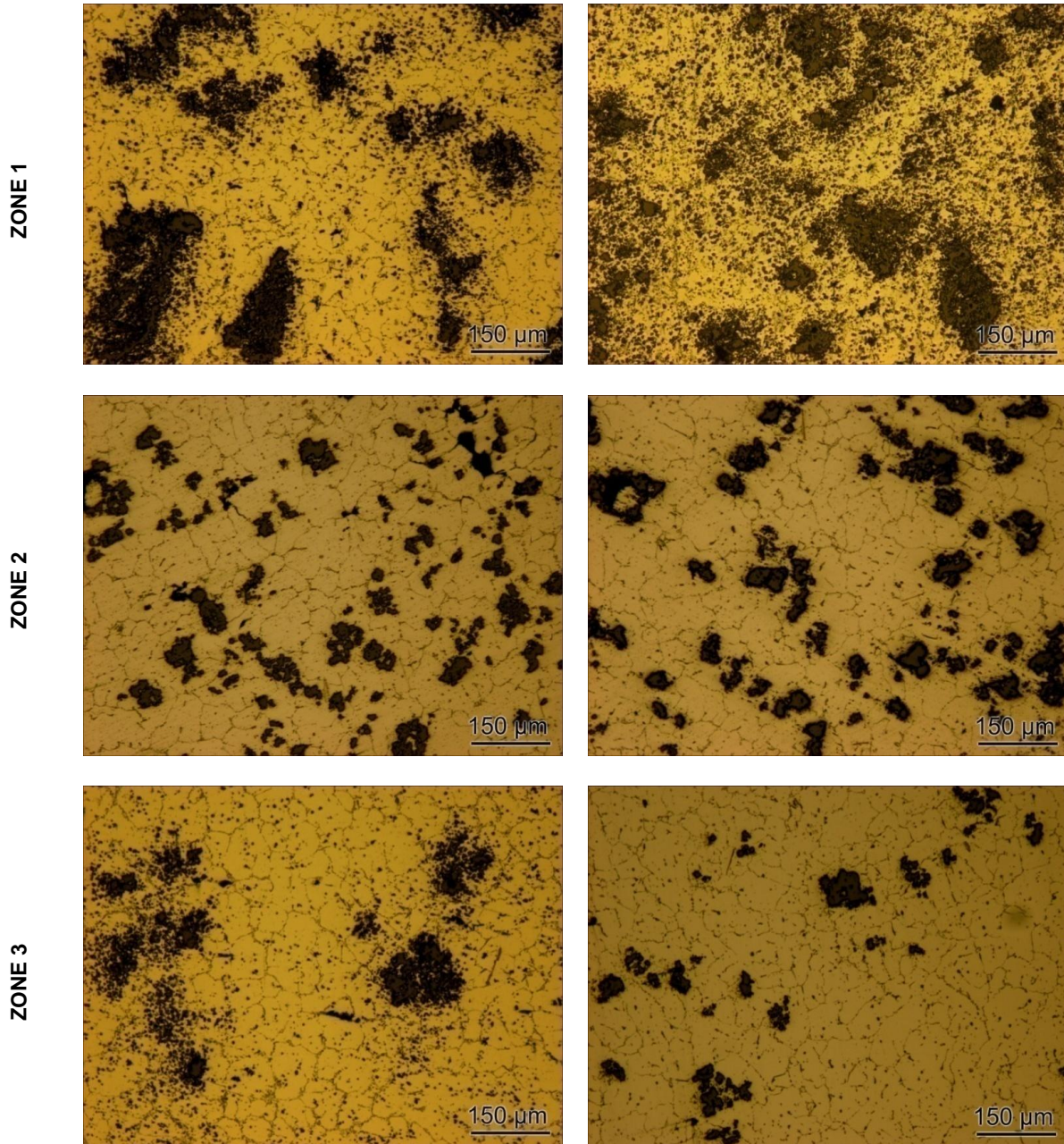


Figure 26 Microstructures in the three defined zones for samples with different weight percent of dodecaboride particles.

### **4.1.3. Scanning Electron Microscopy**

The specimens were also observed in a scanning electron microscope (SEM) furnished with an energy dispersive spectroscopy (EDS) system to corroborate the presence of aluminum, boron, and silicon in the composite component phases, as shown in Figure 27a-d. Figure 27a presents the microstructure of the Al-3wt%B<sub>12</sub>-3wt%Si composite, while Figure 27b is a global EDS spectrum, revealing the presence of boron, aluminum and silicon in the composite, which qualitatively allowed us to determine the elemental composition of both the matrix and the reinforcement particles. Figure 27c presents the microstructure of the Al-3wt%B<sub>2</sub>-3wt%Si composite, while Figure 27d is a global EDS spectrum. As expected, boron signals are stronger in the AlB<sub>12</sub> phase than in the AlB<sub>2</sub> corroborating the nature of the diborides. It should be noted, however, that the boron peak is still very small since the signal from this light element is at the fringes of the detection limit of the EDS system.

By using x-ray mapping the distribution of the constituents present on the composite Al, B and Si is revealed throughout the microstructure, as displayed in Figure 28 and Figure 29 for the dodecaboride and diboride specimens respectively. Those figures provide an overall idea of the result of the elemental mapping: distribution of Al, B and Si on the composites. Silicon is evenly distributed in the matrix grain boundaries of the Al-B-Si composites and also show to have some affinity with AlB<sub>12</sub> particles, as shown in Figure 28.

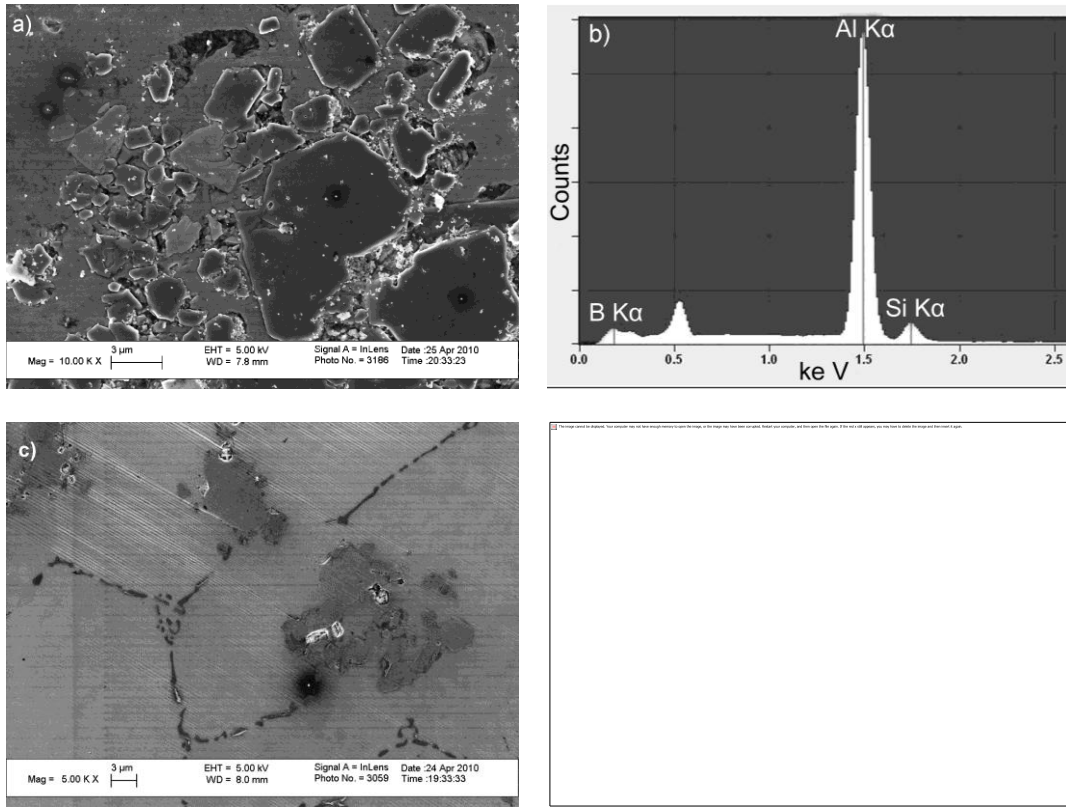
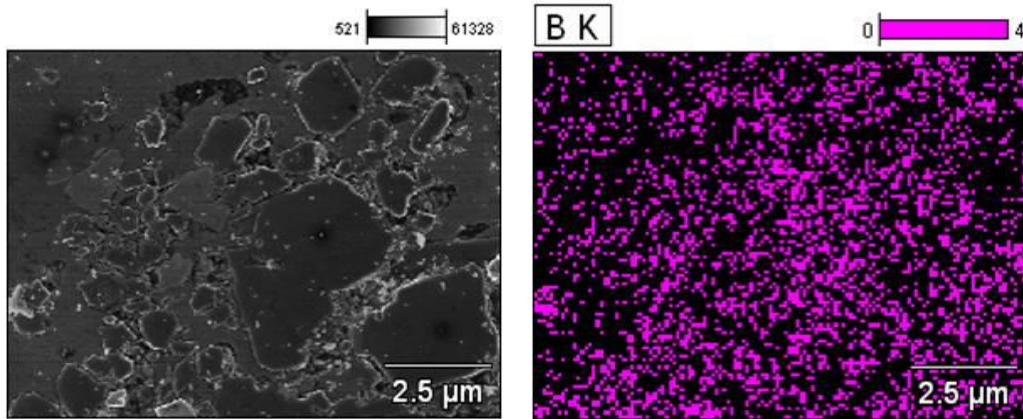


Figure 27 a) SEM image of Al-3wt%B<sub>12</sub>-3%Si, b) Global EDS spectrum obtained on the SEM image area of figure a); c) SEM image of Al-3wt%B<sub>2</sub>-3%Si; d) Global EDS spectrum obtained on the SEM image area of figure c).



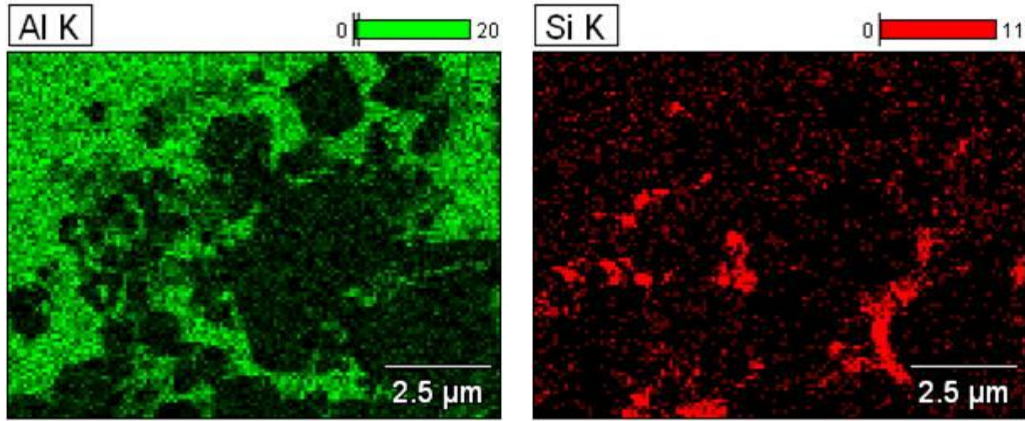


Figure 28 EDS mapping of the Al-3wt%B<sub>12</sub>-3%Si composite.

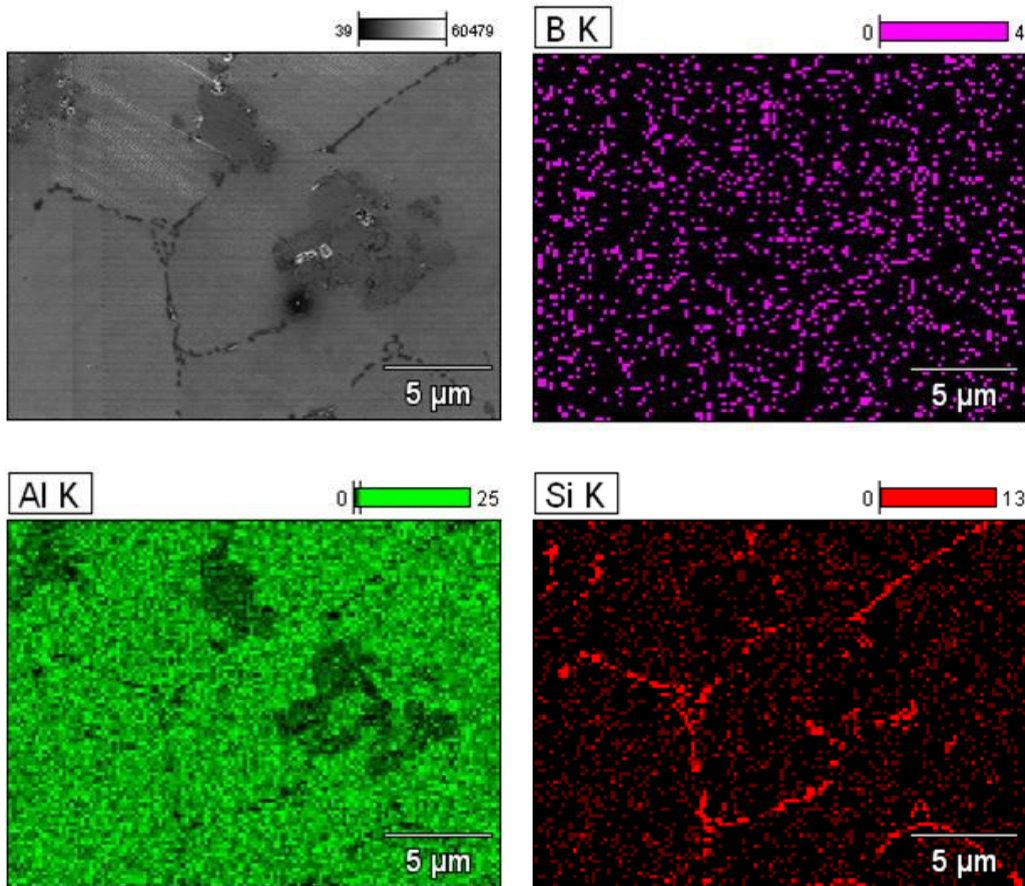


Figure 29 EDS mapping of the Al-3wt%B<sub>2</sub>-3%Si composite.

#### **4.1.4. X-Ray Diffraction**

Representative x-ray diffraction (XRD) graphs of the composites studied are presented in Figure 30 and Figure 31. The range of  $2\theta$  diffraction angle used for this study was from 25 to  $70^\circ$ . The graphs present the spectra obtained from samples from different zones of the centrifuged and vacuum cast specimens. Figure 30 also helped identify the phases present and their corresponding crystallographic planes for the Al-3wt.%B<sub>12</sub>-3wt.%Si specimens. The small peaks are labeled with dashed rectangles as they are barely visible in the overall scans.

Three main peaks of aluminum, namely, (111), (200) and (220) planes at  $38.474^\circ$ ,  $44.723^\circ$  and  $65.100^\circ$ , respectively, are quite apparent in both graphs. For the silicon phase three peaks were found and correspond to the (111), (220) and (311) planes. This data was corroborated with the MDI Jade 8 Software [56]. The diffraction angles corresponding to those peaks are  $28.444^\circ$ ,  $47.305^\circ$  and  $56.125^\circ$ , respectively. Kohn [57], reports AlB<sub>12</sub> peaks from  $2\theta=5^\circ$  to  $40^\circ$  with relative intensity higher than 25%:  $22.607^\circ$  (202) ,  $36.496^\circ$  (242) and  $36.947^\circ$  (341); nonetheless, none of these peaks were immediately detected. This could be due to the complex tetragonal crystal structure of the AlB<sub>12</sub> or maybe because some overlapping with the (111) aluminum peak. Also, small amounts of secondary phases in the alloy make it more difficult to find than other constituents.

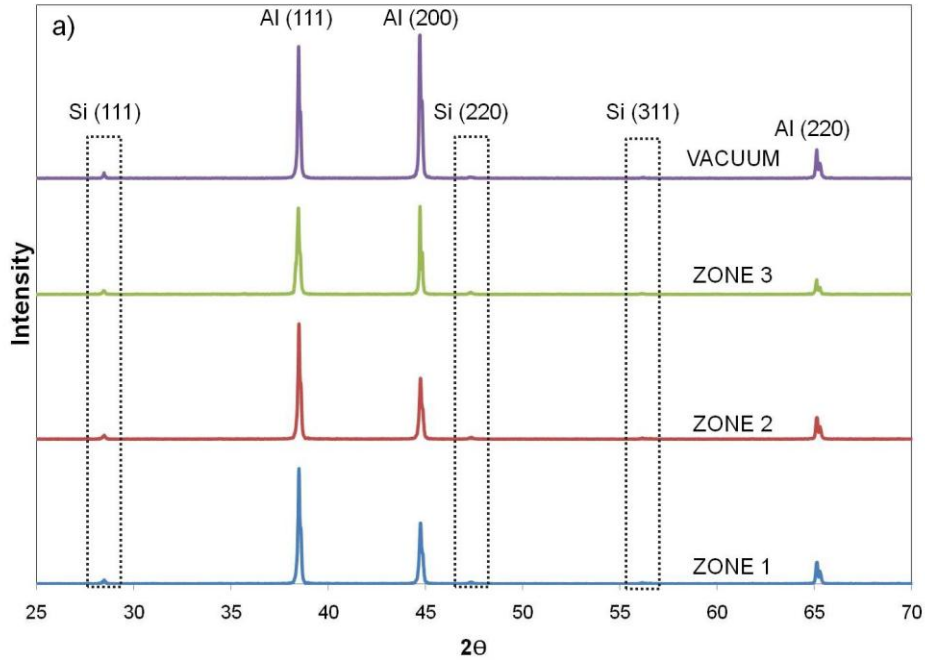


Figure 30 XRD curves showing the phases present on the Al-3wt.%B<sub>12</sub>-3wt.%Si.

Figure 31 shows the results for a specimen containing Al-3wt.%B<sub>2</sub>-3wt.%Si. The aluminum and silicon peaks found matched the ones observed in Al-3wt.%B<sub>12</sub>-3wt.%Si composites. One AlB<sub>2</sub> peak was also discovered by XRD. According to Wang et. al. [58], in the 2θ range from 5 to 40° AlB<sub>2</sub> peaks are reported at 2θ=27.418° (001) and 34.414°. In the present experiment the AlB<sub>2</sub> peak is at 34.414° and corresponds to the (100) plane. Figure 32 shows a close-up XRD graph of this peak.

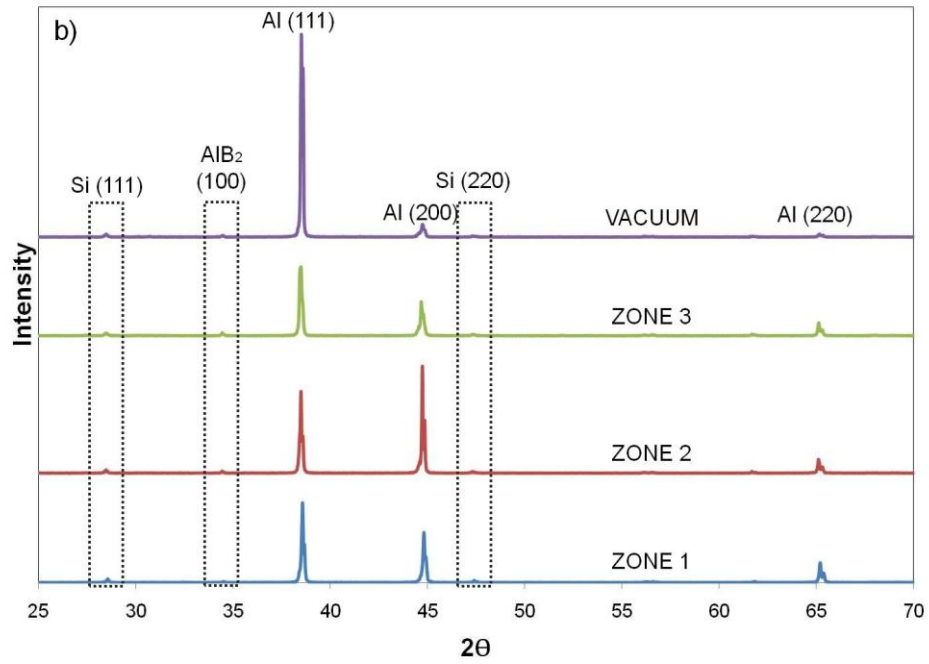


Figure 31 XRD curves showing the phases present on the Al-3wt.%B<sub>2</sub>-3wt.%Si.

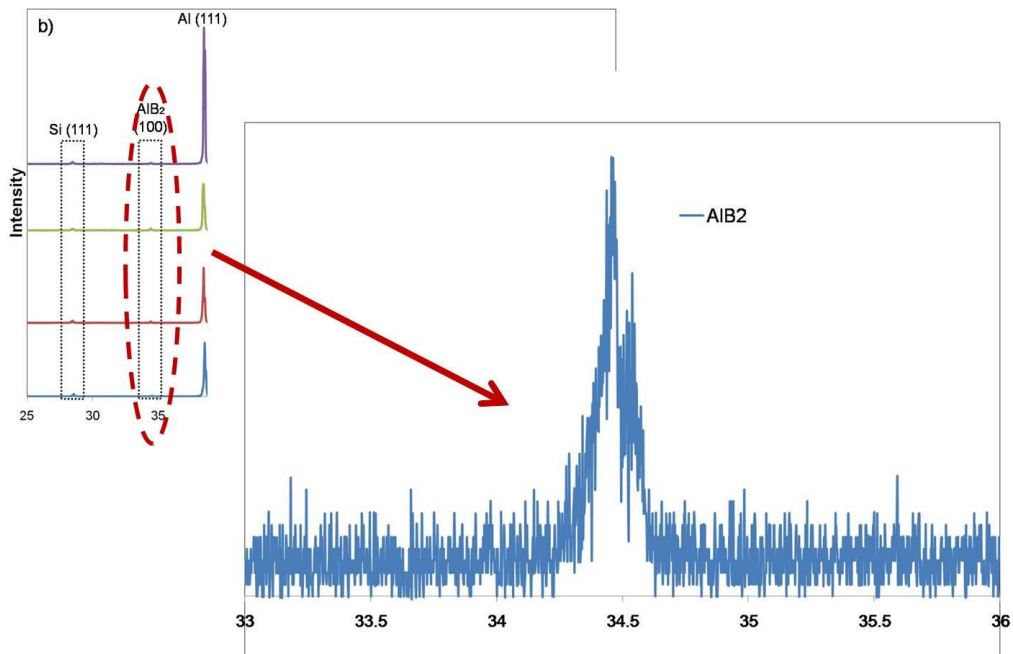


Figure 32 AIB<sub>2</sub> peak.

#### **4.1.5. Volume Fractions of Particles and Pores**

Stereology and quantitative metallography studies have shown that the area fraction of reinforcements obtained (with the mentioned software) is equal to volume fraction, as indicated by Equation 1, which states the equality of volume fraction ( $V_V$ ) to the areal ratio ( $A_A$ ), linear ratio ( $L_L$ ), and point ratio ( $P_p$ ) of the reinforcement phase [59].

$$P_p = L_L = A_A = V_V$$

**Equation 1**

Figure 33a-b present the volume percent of borides and silicon particles for the specimens fabricated via vacuum and centrifugal castings, respectively. Figure 33c shows the volume percent of pores. In Figure 33a-c the error bars represent 95% confidence intervals, while in Figure 33c the negative part of the error bar was omitted, leaving the possibility to find pore free areas in the composites open. Naturally, the volume fraction of boride particles in the composites increased with the weight percent of boron as shown in Figure 33a. Also in this figure we corroborate the behavior observed in the previous section, where the optical micrograph showed the gradient of particles concentration. The volume percent of the silicon phase is shown in Figure 33b, I suggest that higher amounts of Si are present in the specimens containing diboride particles. It is believed that this was an artifact of the image analysis since the diboride clusters are smaller than the dodecaboride clusters occupying more area on the micrograph, which results in less space for the silicon. This implies that the count of silicon particles was more difficult than the boride particles.

Moreover, Figure 33c shows the volume percent of pores present on the fabricated composites and reveals less porosity in the centrifugal samples compared to the vacuum cast samples. Furthermore, the volume percent of pores also increases with the amount of borides (weight

percent of boron) Since several micro pores appear surrounded by particles, such increment in the porosity could be associated to gas entrapment inherited from the Al-B master alloys [60]

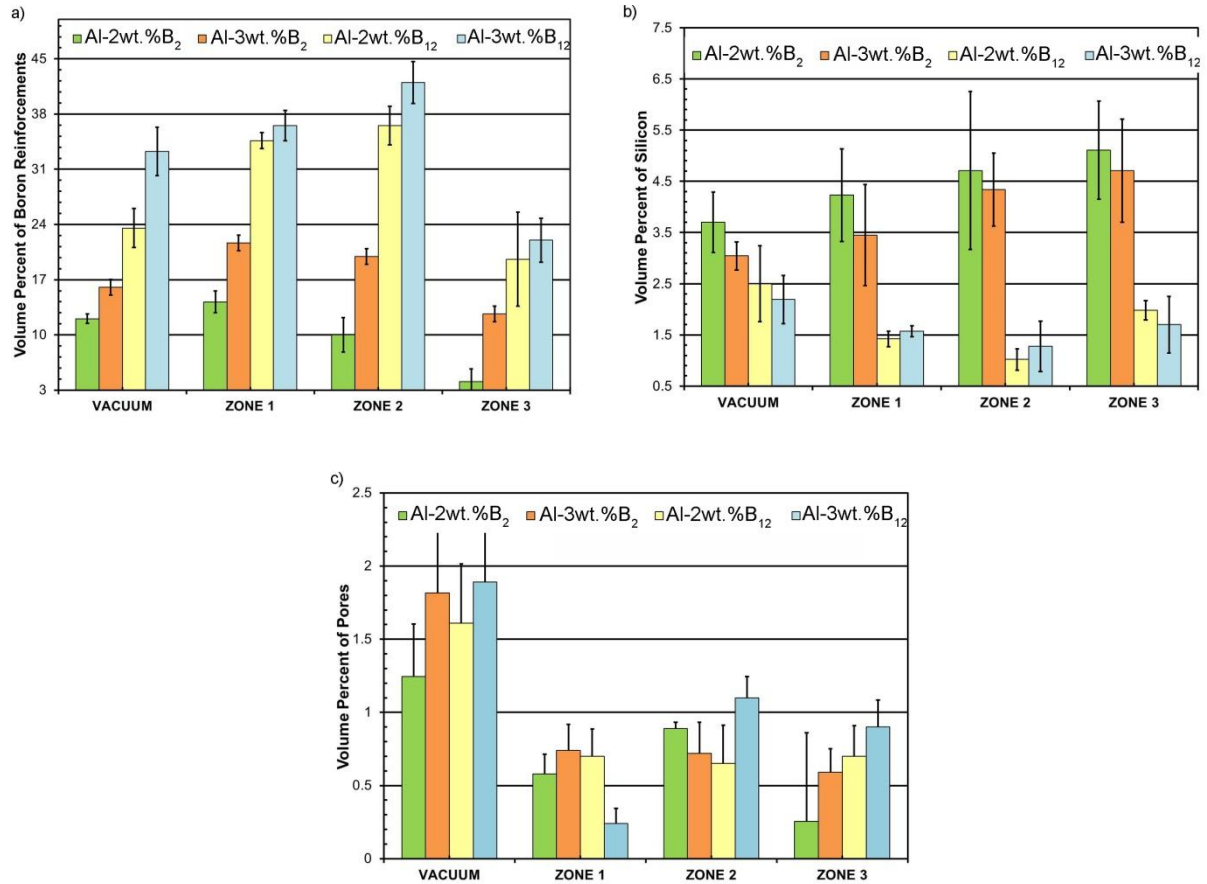


Figure 33 a) Boride particles volume percent as function of wt.%B<sub>x</sub>, b) silicon particles volume percent as a function of wt.%B<sub>x</sub> and c) pores volume percent as a function of wt.%B.

#### **4.1.6 Average Grain Size**

Figure 34 shows the average grain size measured as ASTM G number, here, a large difference in grain size between the centrifugal and vacuum cast samples is apparent. This figure also reveals the decreasing tendency of G values from zone 1 to zone 3 of the centrifugal cast specimens (note that small G values represent larger grain size). In order to corroborate this, an optical comparison of the grain size between the different samples studied is presented in Figure 35 for a characteristic Al-2wt%B<sub>2</sub>-3%Si composite. This micrograph shows a notable reduction in grain size along the centrifugal direction while it confirms the large difference between the grain size of the centrifugal samples and the vacuum cast samples.

This behavior is mostly due to the applied centrifugal acceleration, which was estimated at approximately 30g [61], where  $g$  is the acceleration of gravity. Since the resulting centrifugal force is applied during the composite solidification, the dendritic growth of Al matrix grains is subjected to severe disturbances (facilitated also by the denser AlB<sub>2</sub> and AlB<sub>12</sub> particles movement up to zone 1). The growing dendritic structure then breaks up to produce additional nucleation sites for solid aluminum [62].

This phenomenon, along with the high rate of solidification induced by the centrifugal process and high conductivity of the graphite mold, prevents the formation of large matrix grains. A similar trend was also observed in the AlB<sub>12</sub> -reinforced-composites. Conversely, the matrix grain size of the vacuum cast samples is considerably larger since the solidification cooling rate was slower than the centrifugal samples and nucleation and grain growth proceeded undisturbedly.

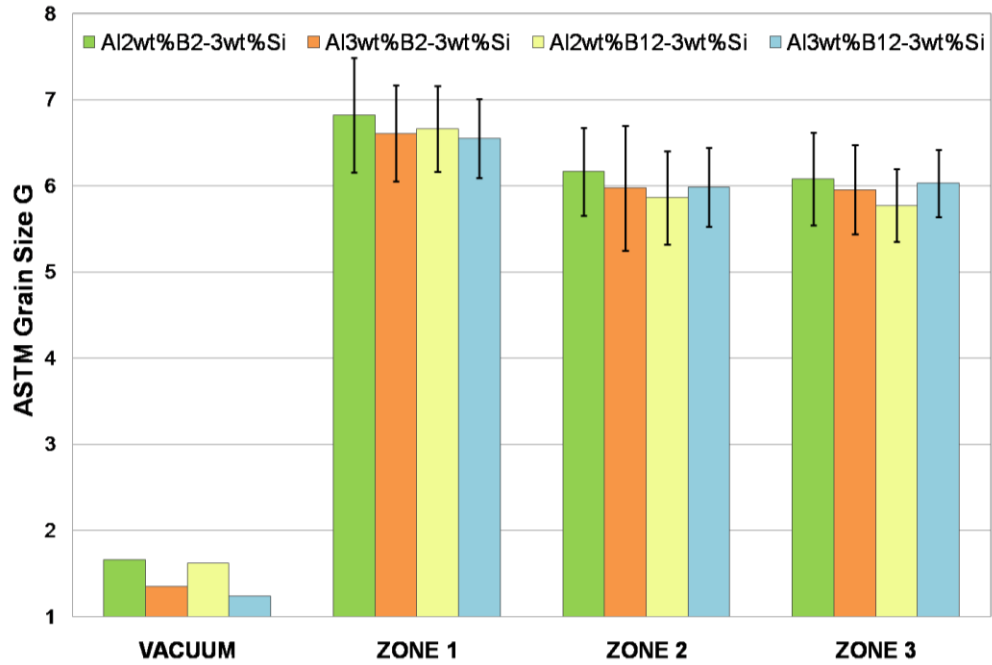


Figure 34 Measured average ASTM grain size G.

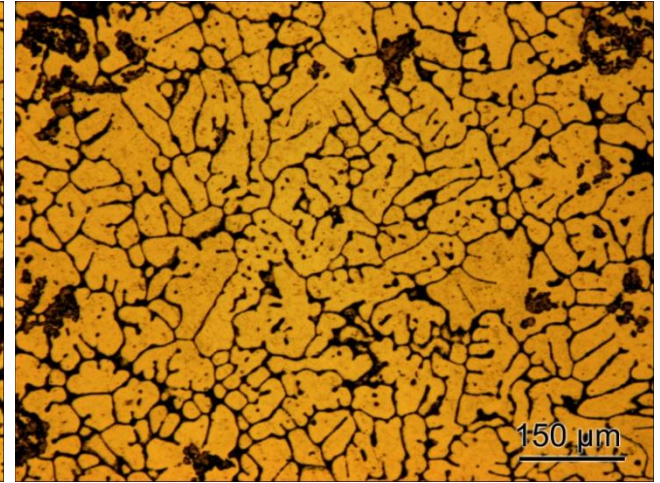
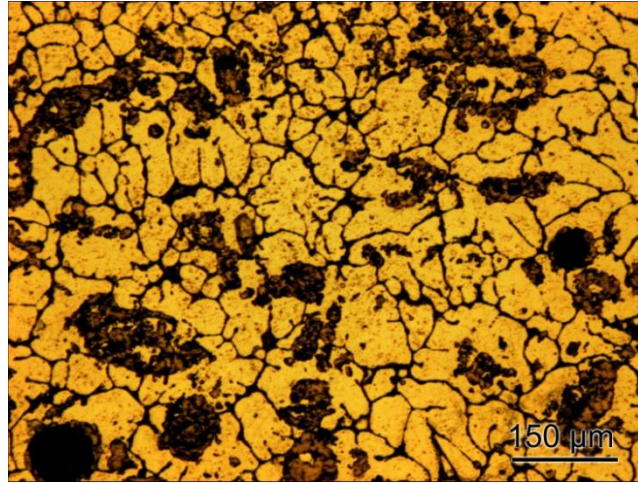
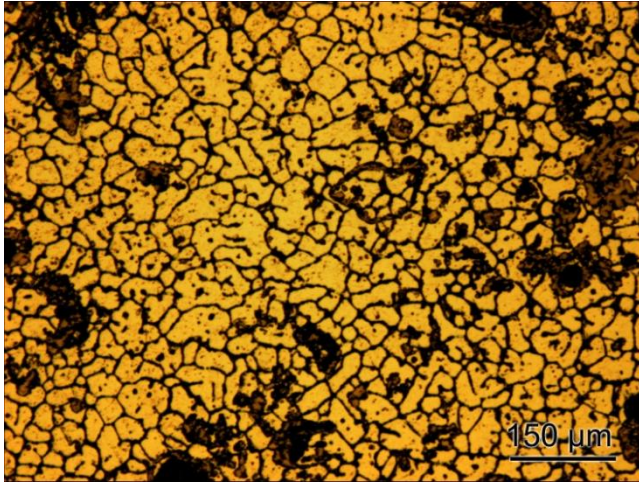
**Centrifugal Casting Direction**



**ZONE 1**

**ZONE 2**

**ZONE 3**



**VACUUM**

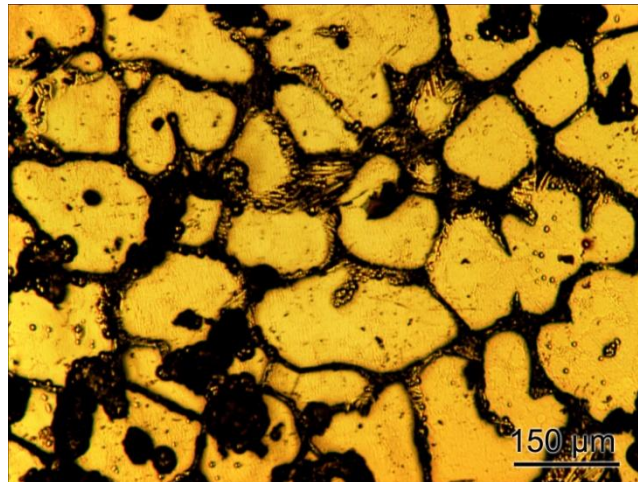


Figure 35 Optical micrographs of grain size distributions throughout centrifugal Al-2wt%B<sub>2</sub>-3wt%Si composite compared with Al-2wt%B<sub>2</sub>-3wt%Si vacuum cast specimen.

## 4.2. Hardness

### 4.2.1. Superficial Rockwell Hardness and Vickers Microhardness

Results of the superficial Rockwell hardness tests conducted on the Al-B-Si specimens are displayed in Figure 36a-b. To a certain extent, these results corroborate the gradual functionality of the composites, as the hardness values on each specimen follow the same pattern as that of the volume percent of reinforcement along the direction of the centrifugal force. In other words, these results are a direct consequence of the segregated aluminum boride particles along the main axis of the cylindrical sample.

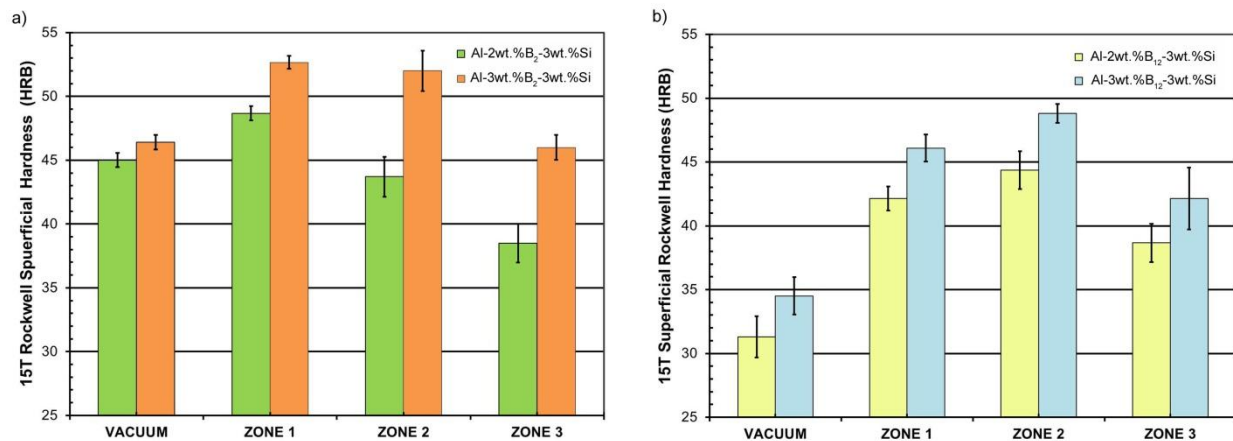


Figure 36 Superficial Rockwell hardness along the longitudinal axis of the centrifugally cast Al-B-Si composites: a) containing AlB<sub>2</sub>, b) containing AlB<sub>12</sub>.

The resulting Vickers microhardness mean values are presented in Figure 37; it is apparent that microhardness did not vary noticeably compared with the trend observed in the superficial Rockwell hardness values. This is because the microindentation tests were done solely on the matrix and from these results we can infer that the hardness of the matrix was mostly unaffected by the segregation of reinforcement particles. This was also observed in an prior investigation [6]. Furthermore, both superficial hardness and microhardness values increased as the percent of boron (and consequently the amount of reinforcement) increased.

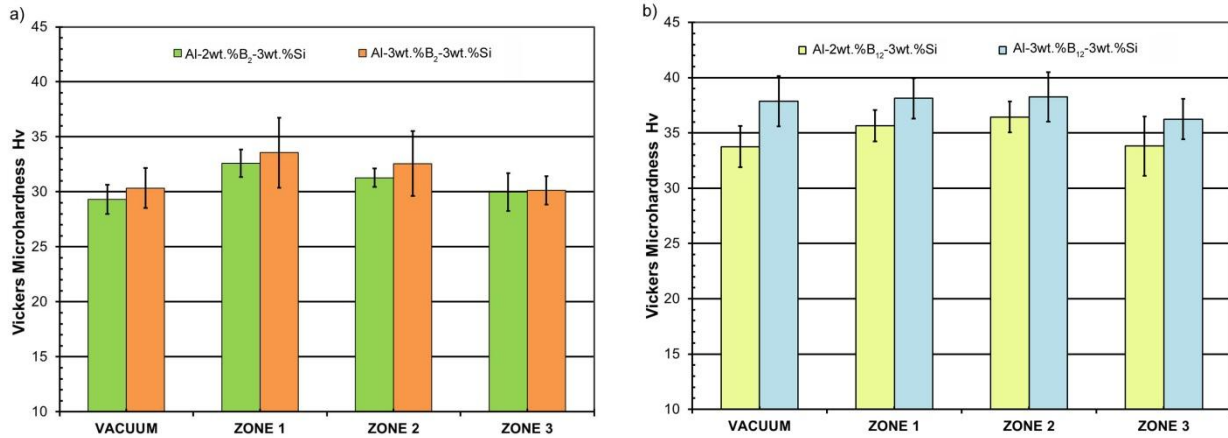


Figure 37 Vickers microhardness along the longitudinal axis of centrifugally cast Al-B-Si composites: a) containing AlB<sub>2</sub>, b) containing AlB<sub>12</sub>.

From these results, we discovered that composite specimens containing AlB<sub>2</sub> particles possessed higher Rockwell hardness than specimens containing solely AlB<sub>12</sub> particles. Nonetheless, at the microscale it was found that the specimens reinforced with AlB<sub>2</sub> particles had smaller Vickers microhardness than the specimens with AlB<sub>12</sub>. These two conflicting findings motivated us to seek for an explanation of the underlying phenomenon that caused this discrepancy. To further investigate these results, using SEM we analyzed two sets of composite specimens containing 3 wt.% B; one with B combined as AlB<sub>2</sub> particles and the other one with AlB<sub>12</sub> particles in three main locations: indentation free zones, near Rockwell indentation zones and on the surface zones affected by the Rockwell indentations.

SEM secondary electron images from the unaltered composites are shown in Figure 38a and Figure 38b. These images (obtained at the same magnification) revealed that samples containing dodecaboride particles exhibited discontinuities along the matrix/particle interface, a defect not present in samples with diboride particles. These cracks could only be detected with the aid of an SEM and not in the optical micrographs. As discussed later, it is believed that the

discontinuities in the interface result from stresses arising from the mismatch in the coefficients of thermal expansion (CTE) between aluminum and the reinforcing particles.

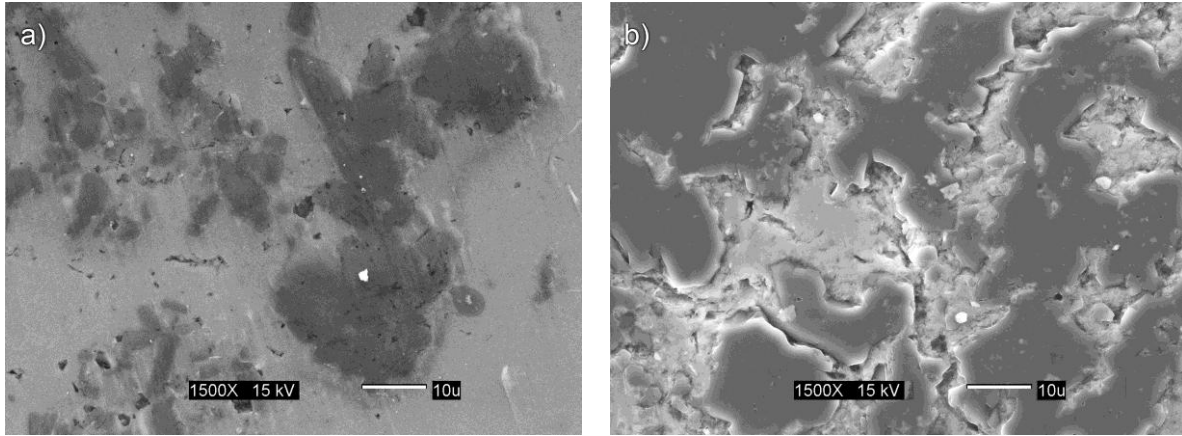


Figure 38. SEM secondary electron images of undamaged areas of Al-B-Si composites a)  $\text{AlB}_2$  and b)  $\text{AlB}_{12}$ .

Additional secondary electron images were obtained from specimens with Rockwell indentation marks, as shown in Figure 39a, b. These figures show the damage caused by the Rockwell indentation is large enough to fracture  $\text{AlB}_{12}$  particles and cause them to detach from the aluminum matrix (Figure 39b). Conversely, as evinced by Figure 39a, the diboride particles did not break upon indentation and remain attached to the matrix. Therefore, Figure 39a and Figure 39b may explain qualitatively the trend observed in Figure 36, where the specimens containing dodecaboride particles showed lower values of Rockwell hardness when compared with specimens with diboride particles. This manifest behavior could be accredited to the weak (or failed) particle/matrix interface that was revealed in Figure 38b by specimens reinforced with dodecaboride particles.

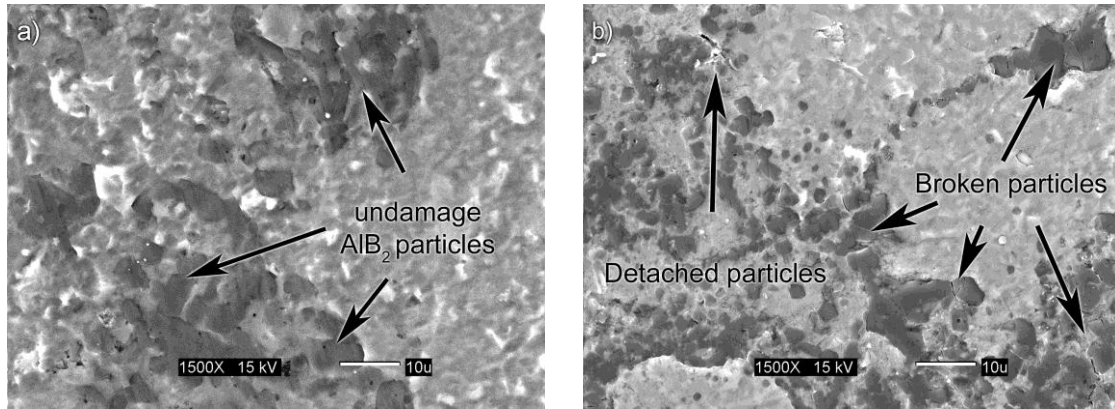


Figure 39 SEM images of Rockwell indentation on both composites studied within the Rockwell indentation mark on a composite containing: a) diboride particles; and c) dodecaboride particles.

#### 4.2.2. Mechanical Properties via Nanoindentation

This section includes the characterization of the matrix and its reinforcements via nanoindentation in representative composite specimens. As a consequence, the elastic modulus (E), hardness (H), and the interaction between reinforcing particles and the matrix were investigated using this advanced technique. As mentioned before, the study of the mechanical properties in MMCs via nanoindentation and finite element analysis have been the object of intensive studies [63-66]. This existing information provides solid theoretical background to the experimental approached hereby reported.

The composite matrix analysis consisted of fifteen nanoindentations on three regions of the microstructure: the matrix itself, the matrix grain boundaries and the matrix in the vicinity of the particles (25  $\mu\text{m}$ ). The load used to this purpose was 250mN applied via a Berkovich diamond tip. The particle analysis included five different loadings and fifteen indents per loading. Previous works have shown that the surface area of AlB<sub>2</sub> particles has a bigger influence on the required pressure to push-in the particle into the matrix [66]. For this reason the particles were selectively chosen to have more or less the same surface area. Fifteen indents were completed in zone 1 of the centrifuged Al-3wt.%B<sub>2</sub>-3wt.%Si composite and on zone 2 of the centrifuged Al-

3wt.%B<sub>12</sub>-3wt.%Si specimen. The purpose of this test has been to investigate the effect of the phases present (silicon and borides) on the hardness of adjacent aluminum matrix and the overall composite.

The effect of the silicon was measured at the grain boundaries (location of the eutectic silicon). The results of the analysis performed on the aluminum matrix are presented in Figure 40. This figure shows the elastic modulus as a function of the hardness at three different zones of the matrix for the samples containing diboride and dodecaboride particles. The results reveal that the elastic modulus increases as the tip indents the matrix closer to the boride particles. Also it was found a slight decrease on E when the indent is at the grain boundaries. Furthermore, the matrix hardness is also higher in the vicinity of the particles while the hardness of the grain boundaries is higher than the matrix. This demonstrates the effect of eutectic silicon which affects the mechanical properties of the grain boundaries.

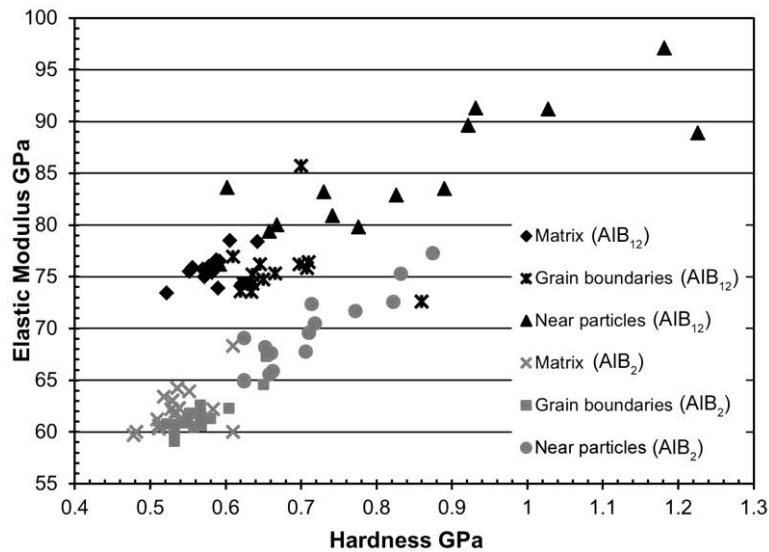


Figure 40 Elastic modulus as a function of hardness obtained via nanoindentation from different localizations of composites containing diboride and dodecaboride particles.

Those findings are supported by prior research, Olivas, Swadener and Shen [65] investigated via nanoindentation, investigated the load effect of the reinforcement contained in a metal matrix

compared to the matrix-strengthening by the surface residual stresses, as a result, the improvement of the yield strength of metal matrix near the particle. Additionally, this figure goes in hand with the Composite Sphere Model developed previously [63]. The author of this work assumed a circular ceramic particle bordered by plastic and elastic zones of the matrix, as shown in Figure 41. Their study used finite element analysis to determine dislocation density of the matrix based on the effective plastic strain arising due to the thermal residual stresses (difference of thermal expansion between matrix and the particle) and volume fraction of the composite. Moreover, the particle analysis was performed on selectively chosen particles of the same surface area. Different loadings from 4 to 8 mN and 60 to 100 mN were used for this purpose. The first was selected following the test experiment presented in another work [66].

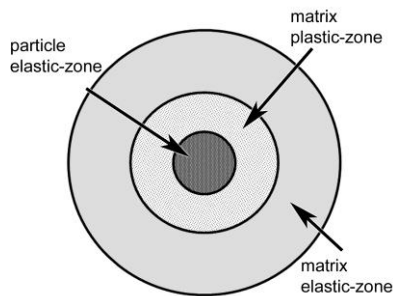


Figure 41 Schematic of the Composite Sphere Model used in [63].

The results of this indentation analysis are shown in Figure 42a-b. As seen in both graphs, the elastic modulus of the  $\text{AlB}_2$  and  $\text{AlB}_{12}$  particles remained within the same range of values in both graphs, with an average elastic modulus of 250.40 GPa and 487.84 GPa, respectively. The hardness data showed the same trend of the elastic modulus and the measured values were 15.87 GPa and 42.29 GPa for the  $\text{AlB}_2$  and  $\text{AlB}_{12}$  particles respectively. These values were then contrasted with measurements on  $\text{AlB}_2$  and  $\text{AlB}_{12}$  single crystals available in the literature [67, 68] and it was discovered that there has been no deterioration of those mechanical

properties of the particle upon processing. From these results it is possible to conclude that the  $\text{AlB}_{12}$  containing composite is an even better alternative than the  $\text{AlB}_2$ -reinforced one.

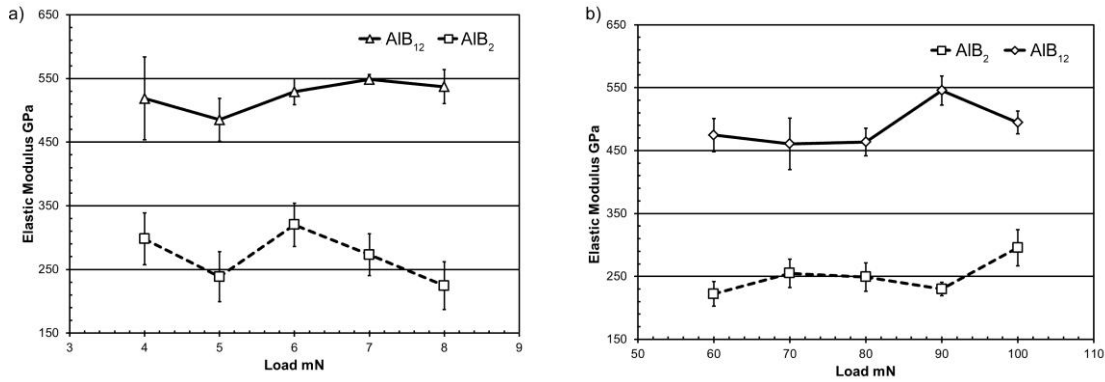


Figure 42 Elastic Modulus of  $\text{AlB}_2$  and  $\text{AlB}_{12}$  particles via nanoindentation at different range of loadings a) 4-8mN and b) 60-70mN.

As a summary of the results obtained in the previous parts and for support reasons, we performed an array of indents around the boride particles. The array was set up to indent the particle, the matrix and the grain boundaries. The array had four rows and seven columns equally spaced at  $25\mu\text{m}$ . The load used in this part was 70mN, where it has eight segments of load and unload. Figure 43a show the optical micrograph of the indentation array performed over the sample containing diborides and Figure 43b the one with dodecaboride particles.

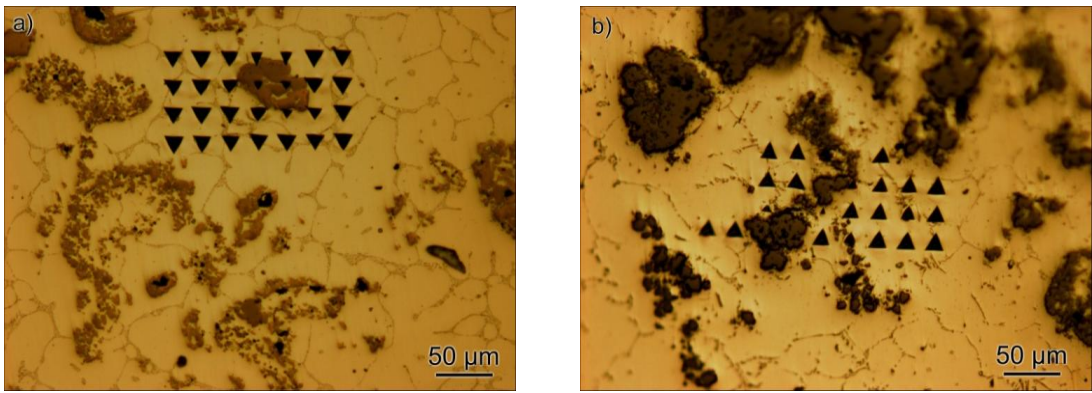


Figure 43 Optical micrographs of the array performed over the borides samples where includes the indent locations around and over the particles a)  $\text{AlB}_2$  sample b)  $\text{AlB}_{12}$  sample.

The results of the indents were plotted using MATLAB software, which also allowed for interpolation of results. The distribution of the elastic modulus and hardness through the array of indents are shown in Figure 44a-d and Figure 45a-b, respectively. These figures present 3D surfaces graph plots for the samples containing diboride and dodecaboride particles respectively. As expected, these figures corroborate the results obtained from the indents analysis performed over the matrix in section 4.2.1. In the literature surveyed it was found that the nanoindentation hardness of aluminum alloys increases in compression and decreases in tension [65]. From these findings it is possible to infer that the boride particles studied in this thesis, are in compression with respect to the aluminum matrix because of the tendency to increase hardness as it approaches to the particle due to the difference on thermal expansion coefficient, volume fraction of particles, dislocation energy and the residual stresses surrounding the particles.

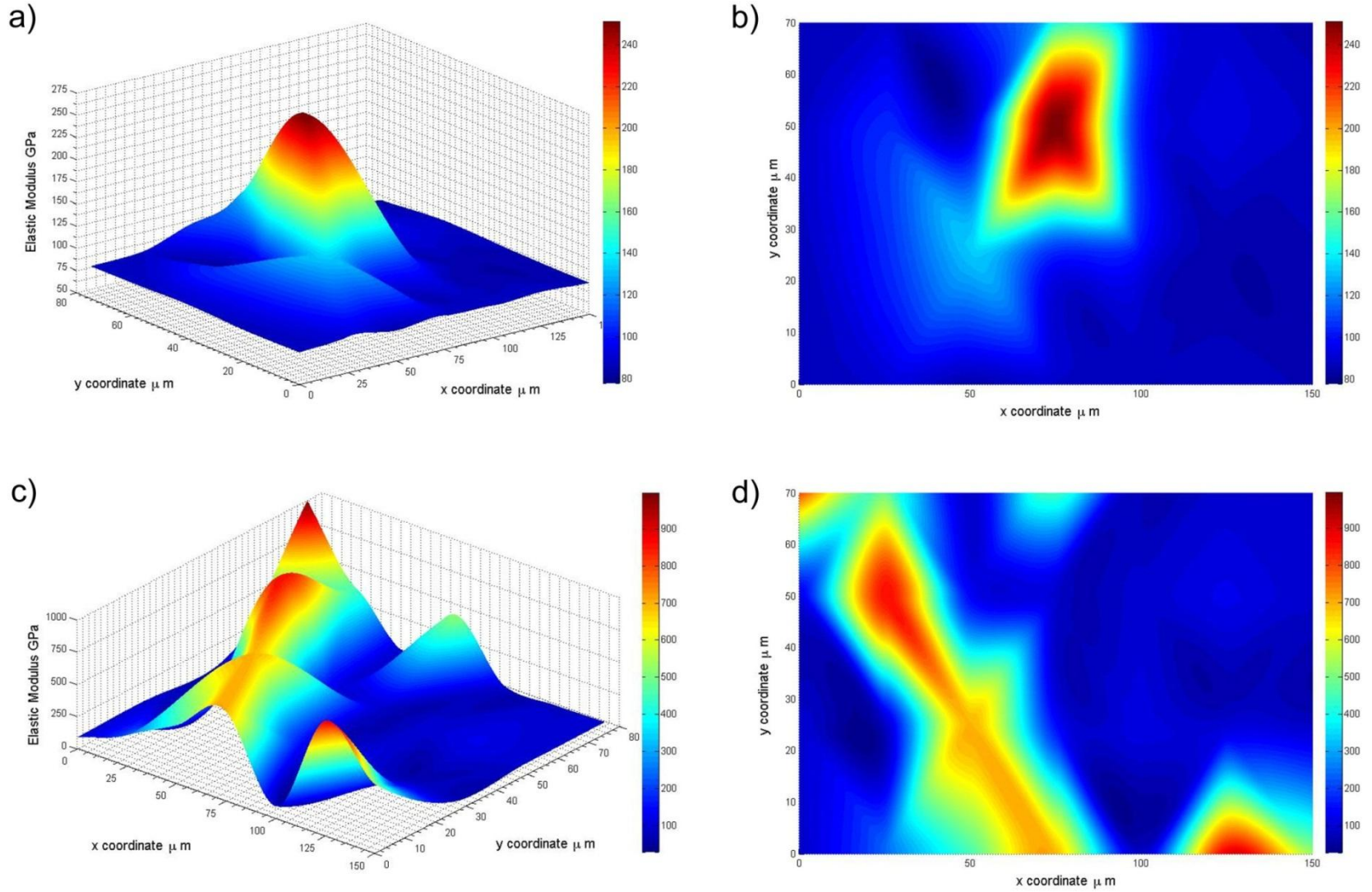


Figure 44 MATLAB plots of the evolution of the elastic modulus at different locations in the array, a) elastic modulus distribution near an  $AlB_2$  particle: b) contour plot of (a): c) elastic modulus distribution near an  $AlB_{12}$  particle: and d) contour plot of (c).

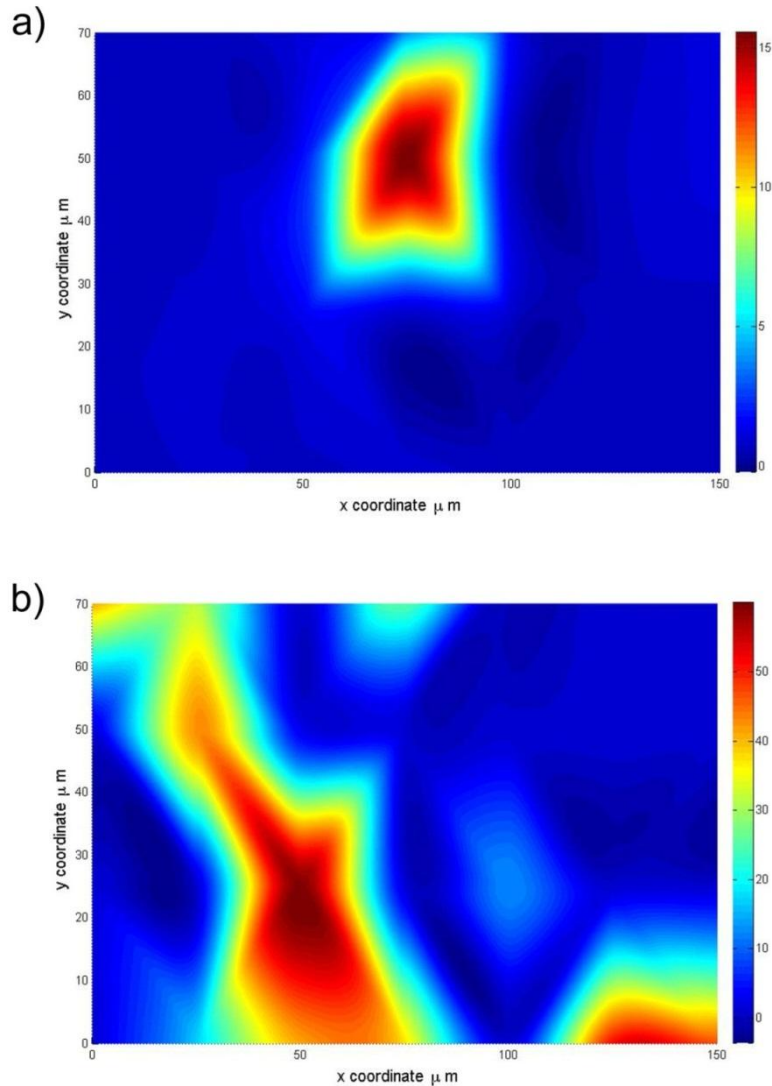


Figure 45 Contour plots of hardness distribution array near particles: a) AIB<sub>2</sub>; and b) AIB<sub>12</sub>.

### 4.2.3. Discrepancy between hardness measurements

When the experimental data is analyzed as a whole, it becomes apparent that the studied composites respond differently at different scales in terms of hardness results. Specifically, the nanoindentation and microindentation experimental data showed that higher hardness values were observed in the matrix of the Al-Si/AIB<sub>12</sub> specimens. On the other hand, at the macroscale bulk hardness our results revealed that the Al-Si-/AIB<sub>2</sub> specimens possessed the higher overall hardness, i.e. combining the strength of both matrix and reinforcements. This discrepancy in

the results could be explained in part by the different techniques employed to measure hardness. Nanoindentation and microindentation are performed over specific points on the surfaces; while macroindentations are performed at arbitrary areas and they cover more surfaces. Bulk indentations are the result of the overall composite performance.

Nonetheless, we believe that most of the apparent discrepancy must arise from the contribution of the composite constituents as well as the behavior of the reinforcement/matrix interface. Moreover, the difference in thermal expansion between the matrix and the reinforcing particles could have a greater impact in this discrepancy. Unfortunately there is scarce information about CTE values of both borides even at room temperature. The only value reported in the literature was the coefficient of thermal expansion for  $\text{AlB}_2$  [69]. From this reference it could be noticed that diboride CTE is significantly lower than aluminum [70].

Furthermore, it is known that both borides have very different melting points:  $1,655 \pm 50$  °C for  $\text{AlB}_2$  and  $2,163 \pm 50$  °C for  $\text{AlB}_{12}$  [31]. This large difference in melting points also agrees with the significant disparity in measured elastic modulus obtained from the nanoindentations results in this research. The larger stability and subsequent stiffness of the dodecaboride led us to infer that its CTE is significant lower than that of the diboride. As a consequence, we believe that the substantial mismatch in CTE between solid aluminum and the dodecaboride particles upon cooling could have caused a stress concentration between the  $\text{AlB}_{12}$  particles and the aluminum matrix. Since  $\text{AlB}_2$  has a higher CTE than  $\text{AlB}_{12}$  smaller stress concentrations are attained in the Al-Si/ $\text{AlB}_2$  composites [71]. Higher stress concentrations would then cause an increase in the dislocation density around the particles which could strengthen the matrix near the interface and, if the local ultimate strength, is exceeded this could lead to the formation of cracks at that interface. Nonetheless, we believe that more extensive studies using nanoindentation and modeling is required to confirm this conjecture.

### 4.3. Thermal Characterization

#### 4.3.1. Differential Thermal Analysis (DTA)

##### 4.3.1.1. Centrifuged and Vacuum Cast Specimens

Characteristic DTA graphs recorded for the centrifugal and vacuum cast samples of Al-2wt%B<sub>2</sub>-3wt%Si composite are presented in Figure 46. During the heating stage the DTA curves exhibited two endothermic peaks: the first peak corresponds to the melting of the Al-Si eutectic (observed with optical microscopy) and the second one, to the Al matrix melting. The characteristic onset temperatures of the DTA curves representing phase transformations (eutectic and matrix melting) were determined by the intersection of the extrapolated baseline and the tangents at the inflection point on the leading edge of the peak (onset determination). There is no apparent difference among DTA curves recorded for the three zones studied from the centrifuged specimens neither for the vacuum cast specimens.

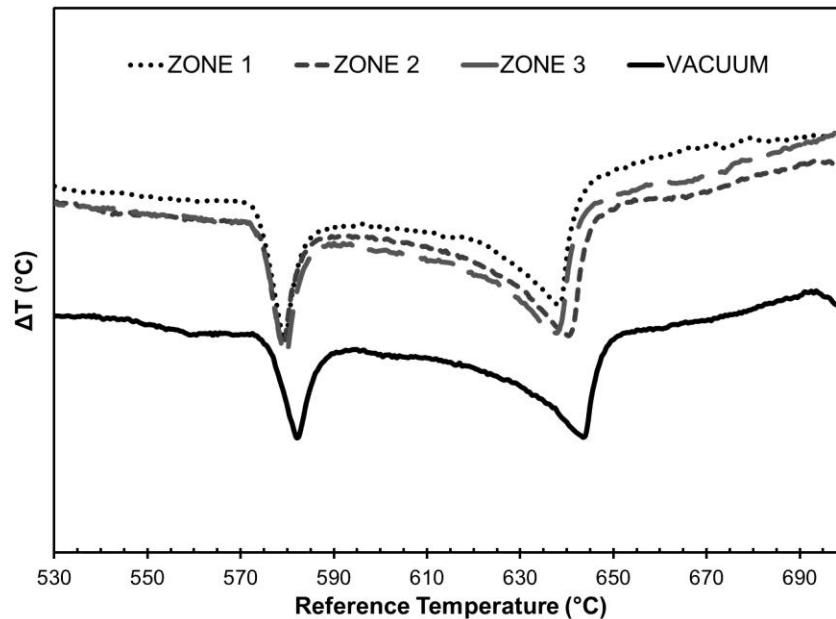


Figure 46 DTA thermograms for the centrifugal and vacuum cast samples upon heating. The first endothermic peak corresponds to the Al-Si eutectic melting and the second one to the matrix melting of Al-2wt%B<sub>2</sub>-3wt%Si composites.

For the sake of comparison using the same DTA parameters we also ran specimens of pure aluminum, Al - 3wt.% B<sub>2</sub> (the same composite without silicon), and Al - 3wt.% Si (binary alloy without boride reinforcements), as shown in Figure 47. Clearly the Al-Si eutectic melting signal is present, as expected, while the melting temperature of the Al matrix is lowered by the presence of silicon. To further verify this, Figure 48 intends to analyze the effect of the diboride and dodecaborides particles on the matrix melting point. From these DTA thermograms we can infer that AlB<sub>2</sub> and AlB<sub>12</sub> particles do not significantly affect the matrix melting point. Table 4 and Table 5 summarize the eutectic and melting ranges respectively. Table 6 shows the reference data obtained experimentally for comparison purposes.

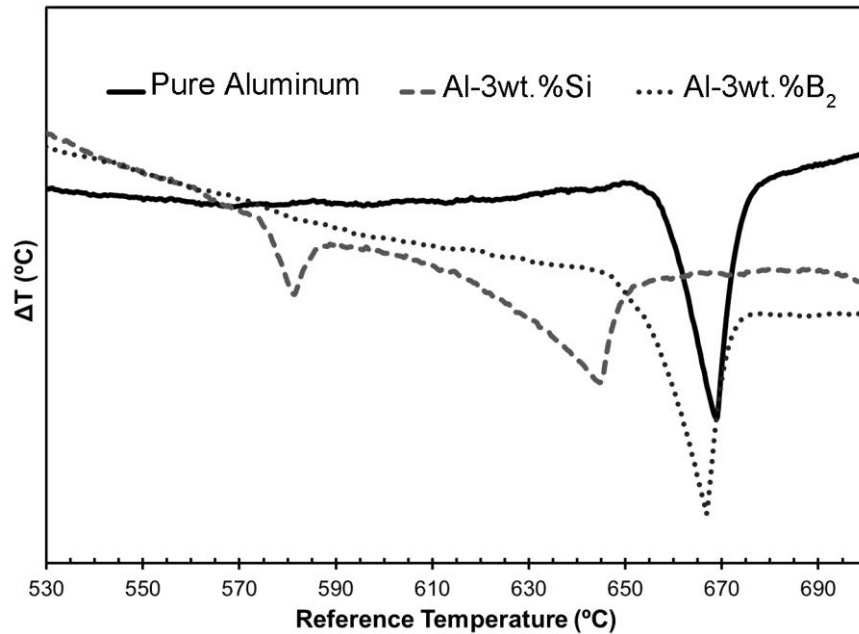


Figure 47 DTA curves of Al-3wt%Si, Al-3wt%B<sub>2</sub> and pure aluminum obtained for reference purposes.

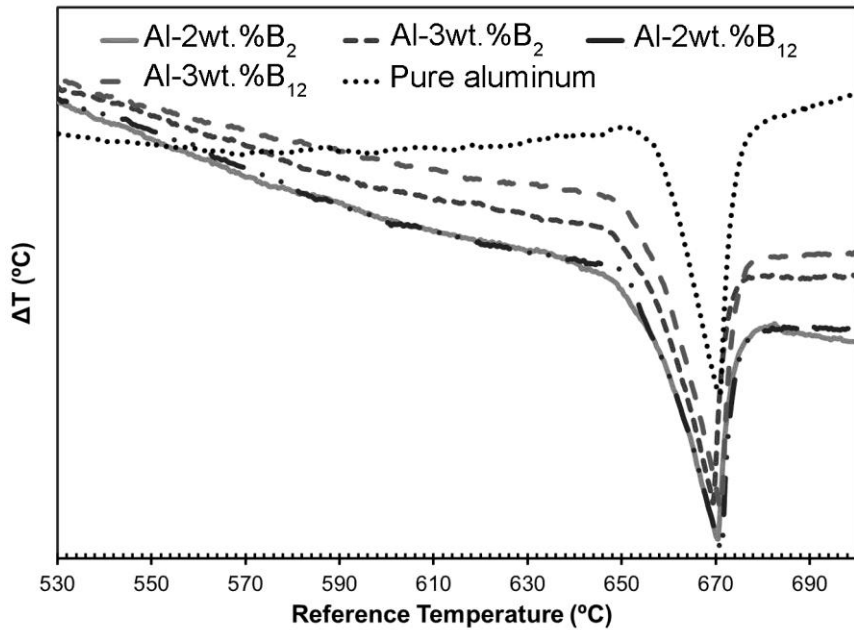


Figure 48 DTA thermograms obtained upon heating to study the influence of boron on the melting of the composites.

Table 4 Eutectic range as measured on the DTA curves.

SAMPLE	Al-2wt%B <sub>2</sub> -3wt%Si (°C)	Al-3wt%B <sub>2</sub> -3wt%Si (°C)	Al-2wt%B <sub>12</sub> -3wt%Si (°C)	Al-3wt%B <sub>12</sub> -3wt%Si (°C)
ZONE 1	574-580	576-583	574-584	575-581
ZONE 2	575-581	577-577	575-585	577-582
ZONE 3	575-578	575-583	574-583	575-578
VACUUM	574-577	576-581	574-579	575-582

Table 5 Melting range measured on the DTA curves.

SAMPLE	Al-2wt%B <sub>2</sub> -3wt%Si (°C)	Al-3wt%B <sub>2</sub> -3wt%Si (°C)	Al-2wt%B <sub>12</sub> -3wt%Si (°C)	Al-3wt%B <sub>12</sub> -3wt%Si (°C)
ZONE 1	630-649	622-648	624-650	627-648
ZONE 2	625-649	629-647	628-649	626-651
ZONE 3	626-647	624-649	624-647	632-645
VACUUM	626-644	625-649	626-645	632-643

Table 6 Eutectic and matrix melting signals measured on the reference specimens.

Phase	Pure Aluminum (°C)	Al-3wt%Si (°C)	Al-2wt%B <sub>2</sub> (°C)	Al-3wt%B <sub>2</sub> (°C)	Al-2wt%B <sub>12</sub> (°C)	Al-3wt%B <sub>12</sub> (°C)
Eutectic	none	577	none	none	none	none
Matrix melting point	657-667	627-643	654-666	654-667	653-666	655-667

**4.3.1.2. Effect of Boron and Silicon on the Thermal Properties of Al-Si-B Composites**

In the previous section it was found that 3 wt.% of AlB<sub>2</sub> and AlB<sub>12</sub> particles do not significant affect the matrix melting point when compared with pure aluminum. To validate and confirm the aforementioned statement, a more in-depth study was performed. To accomplish this, new samples were prepared with 3 wt.% silicon and varying boron levels from 0 to 3 wt.%. Figure 49 shows the results of DTA curves obtained from dodecaboride-containing specimens. These results reveal that the boron percent of the composite do not show a consistent tendency in the reduction of the matrix melting temperature. Therefore, due to the small increase in boron percentage, no significant melting temperature decrease can be directly associated with increasing amounts of boron in the composites.

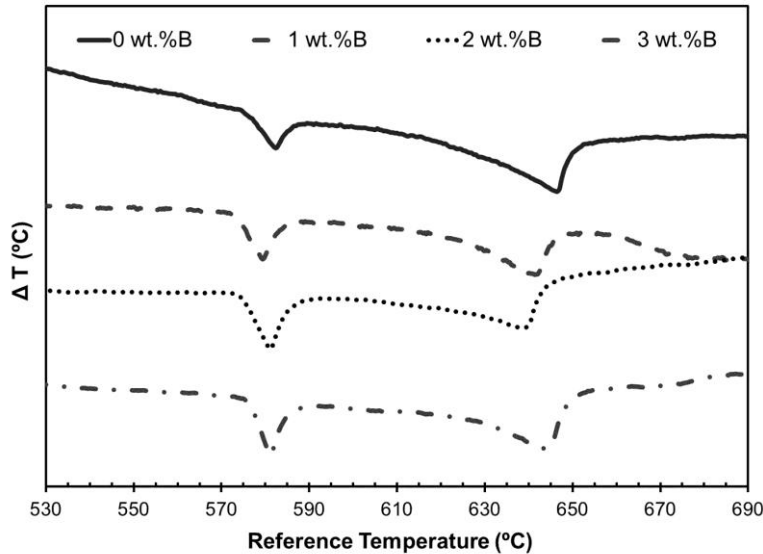


Figure 49 DTA thermograms showing the effect of boride particles on the matrix melting point.

To study the effect of silicon on the thermal properties behavior of the Al-Si-B composites additional samples were also fabricated, in this case, containing 3 wt.% of boron and varying silicon from 0 to 3 wt.%. The resulting DTA curves are presented in Figure 50 for the composites containing diboride particles. This figure shows how the matrix melting point decreases as a function of silicon percent on the composites. This behavior appears in the graph as a displacement to the left of the melting (endothermic) peak. This figure also shows the evolution of the eutectic peak from 0 to 3 wt.% silicon. For the samples containing dodecaboride particles the same behavior was observed.

In closing, from the analysis of these DTA curves it is confirmed that silicon is the major responsible on the decreasing tendency of the matrix melting point on the fabricated composites.

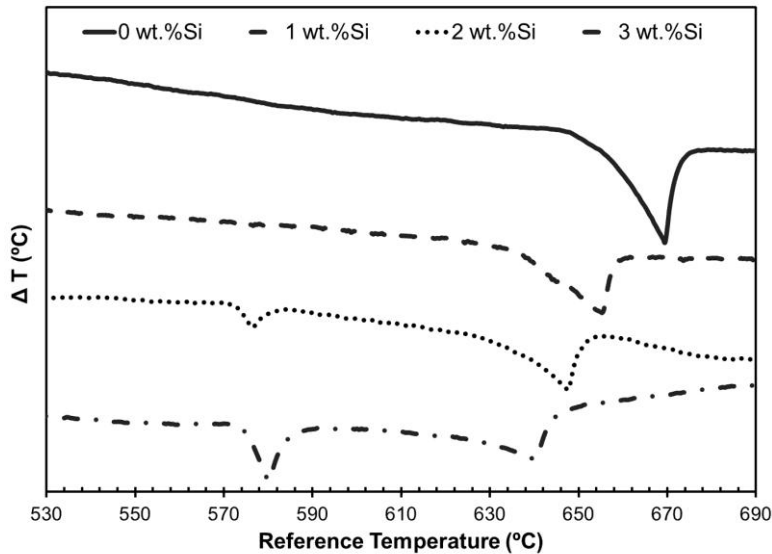


Figure 50 DTA thermograms of the influence of silicon percent in Al-3wt.%B<sub>2</sub> composites.

#### 4.3.2. Coefficient of Thermal Expansion (CTE) via Thermomechanical Analysis

Following the ASTM E831-03 standard three samples were analyzed of each specimen to obtain a better approximation to the actual behavior. The average CTE for commercially pure

aluminum is  $24 \times 10^{-6} \mu\text{m}/\text{m}^\circ\text{C}$  [72]. Experimentally with a Mettler Toledo TMA/SDTA 841 we found that as received pure aluminum has CTE of  $29.4 \mu\text{m}/\text{m}^\circ\text{C}$ . From the surveyed literature we found that aluminum alloys has a CTE that varies from 24 to  $31 \mu\text{m}/\text{m}^\circ\text{C}$  and also that its CTE is affected by the presence of silicon (CTE  $2.5\text{-}3.6 \mu\text{m}/\text{m}^\circ\text{C}$  [73]) and copper (CTE  $16.4\text{-}20.5 \mu\text{m}/\text{m}^\circ\text{C}$  [74]), which reduces expansion, and magnesium, which increases it [72]. However, it is not well known how the presence of borides and silicon affects the CTE. For this reason, we also measured the CTE of the Al - 3wt.% Si binary alloy:  $23.7 \mu\text{m}/\text{m}^\circ\text{C}$ . We used this value, rather than the CTE of the as-received pure aluminum, as the reference material to compare it with the CTEs of the composites containing borides.

Figure 51 shows the measured CTE values as a function of the volume percent of boride particle on centrifuged and vacuum cast specimens. It is evident that the CTE decreases as the volume percent of boride particles increases. When compared with the CTE of the reference sample (Al 3wt.%Si), the CTE of the composites containing boride particles is higher. The CTE of the centrifuged specimens has a tendency to decrease in the centrifugal direction, as presented in Figure 52. Therefore, zone 1 has the minimum CTE of all of the specimens studied; then zone 2 and zone 3 present increasing values of CTE. The vacuum cast specimens show a CTE between the values obtained for zone 2 and zone 3.

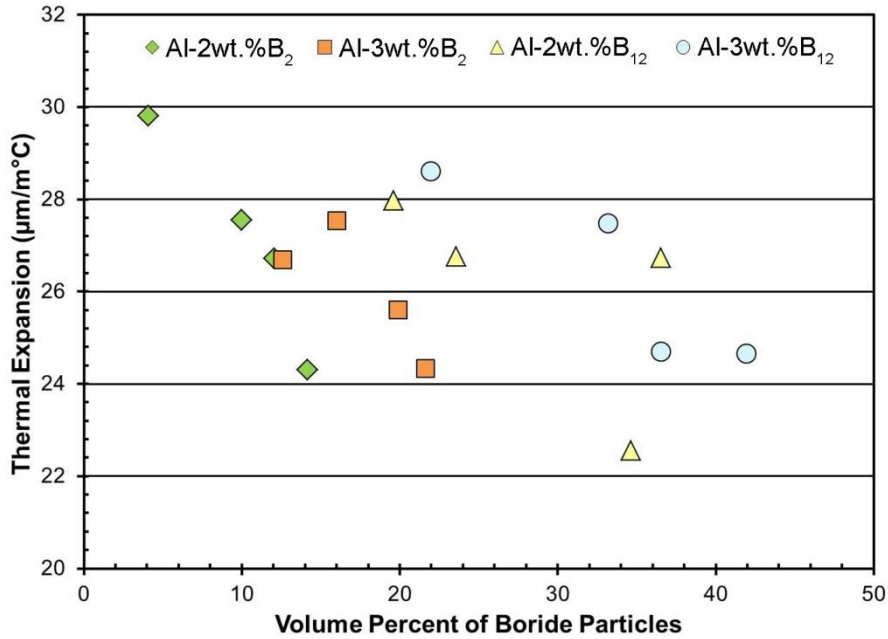


Figure 51 CTE of centrifuged and vacuum cast specimens as a function of reinforcement volume percent.

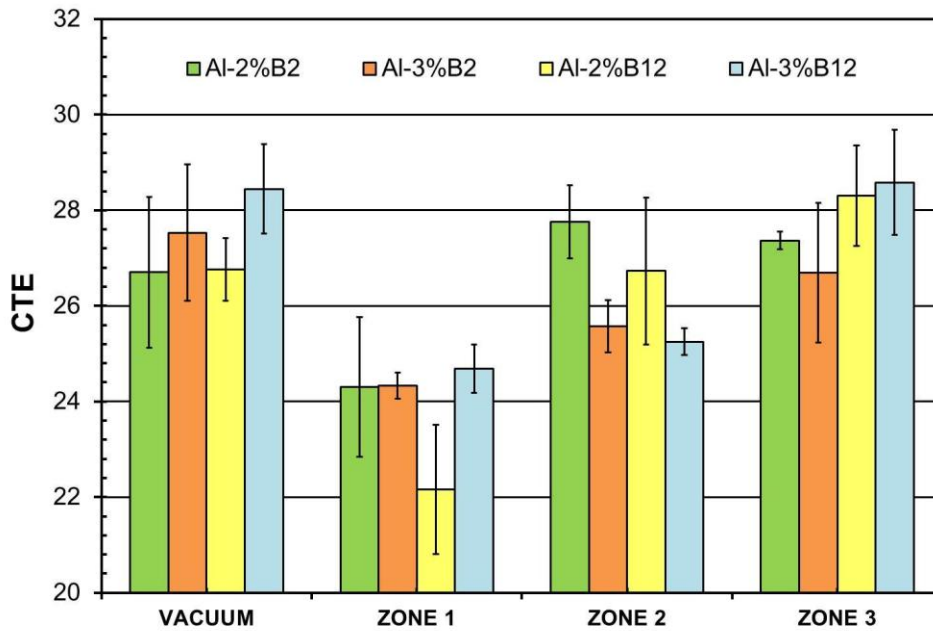


Figure 52 CTE of centrifuged and vacuum cast specimens.

In addition we also measured the CTE of samples with boron and silicon concentrations varying from 0 to 3 wt.%. The purpose of these measurements was to study more in detail the effect of

silicon and boride particles when one element is kept constant while the other varies. Figure 53 shows the CTE of the gravity cast samples as a function of the boron percent and demonstrates that the CTE increases for higher boron levels. On the other hand, Figure 53 also shows how the CTE varies when the silicon percent rises from 0 to 3 wt.%. As expected, the CTE decreases as the volume percent of silicon increases [75, 76]. Those figures help to conclude that the CTE also depends on the method of fabrication of the sample because the centrifuged samples present a thermal expansion behavior completely different from the vacuum and gravity cast samples.

In the revised literature [77-80], it has been reported that the CTE varies inversely with the grain size. In a previous section (4.1.6.) it was discussed how the grain size of the centrifuged samples varied along the direction of the centrifugal force while zone 1 was the one with the smallest grain size. Through research presented in this segment it was discovered that the reinforcement amount in zone 1 is responsible of the decreasing tendency of the CTE on the centrifuged samples regardless of the grain size.

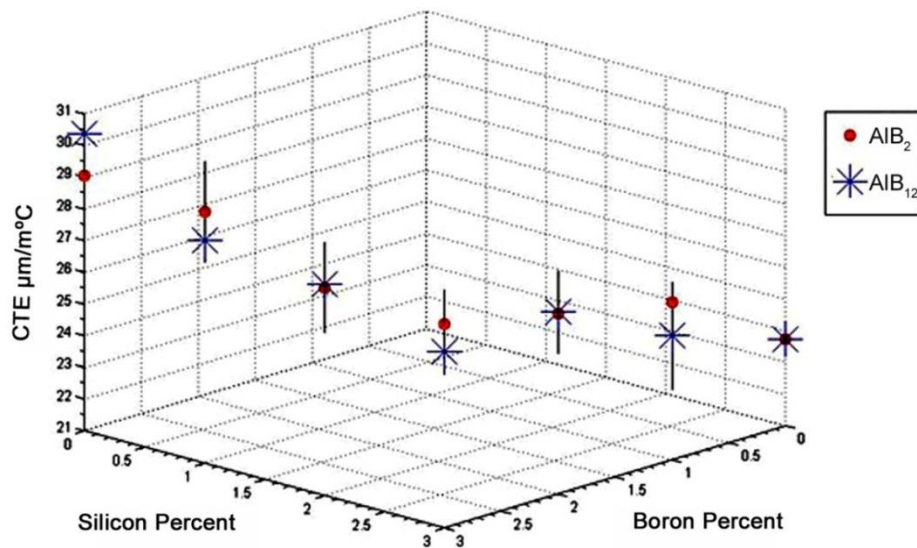


Figure 53 CTE of gravity cast samples as a function of silicon and boron percent.

## **Chapter 5: Methodology of Fabrication and Characterization of the Hybrid Composites**

---

As mentioned in Chapter 1, the ultimate goal of the project of which this thesis is part, has been to fabricate a hybrid material made of a metal based composite (thin film) by using the fabricated target and a polymer. The polymer used is polystyrene-isobutylene-styrene (SIBS), and is provided by a parallel research group led by Dr. Agnes Padovani (UPRM General Engineering Department). The subsequent paragraphs describe some of the details of the polymer used and its fabrication. Finally, a brief description of the sputtering system, process parameters and the targets selected, and also, a brief description of the characterization techniques used is provided.

### **5.1. Polymer Description and Method of Fabrication**

Poly-(Styrene-IsoButylene-styrene) commonly known as SIBS is tri-block copolymers with potential application in fuel cells, sensors, and electronics. The copolymer is derived from two monomers, styrene and isobutylene, which form the structure presented in Figure 54. The resulting triblock copolymer is of the form ABA. Polystyrene gives the mechanical stability or strength to the polymer while polyisobutylene provides SIBS with low temperature flexibility. The percentage by weight of the constituent polymers of SIBS for this particular research is 70% polyisobutylene and 30% polystyrene.

SIBS are commonly used in chemical and biological protective clothing for soldiers and fuel cells since it is a proton exchange membrane, which is able to conduct protons and is impermeable to hydrogen and oxygen. In the following paragraph a brief discussion of the production of the thin film, using SIBS, is discussed.

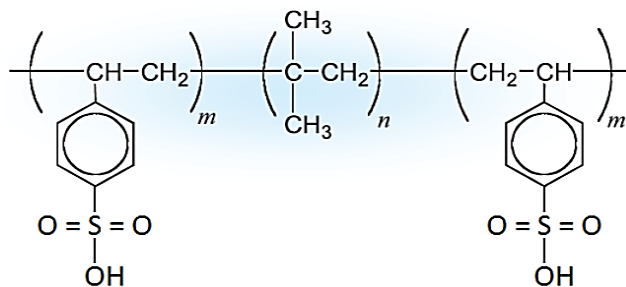


Figure 54 Poly(styrene-isobutylene-styrene) ABA structure.

SIBS thin films are deposited using a Brewer Science CEE Spin Coater on silicon wafers as substrates. First, the substrate is loaded and centered into the spin coater, which uses vacuum to hold the substrate in place. Next, the S-SIBS solution is deposited on top of the substrate and it is spun at a 200 rpm for 10 seconds so the solution is evenly distributed over the substrate. After this, the substrate is spun at 2000 rpm for 30 seconds. The final step is heating the substrate on a hot plate to evaporate any remaining solvents from the film. The concentration of the polymer solution and the spin speed can be varied in order to modify the resulting film thickness of 1.5  $\mu\text{m}$ . It is important to mention that the fabrication and characterization of this polymer is beyond of the scope of this thesis.

## 5.2. Description of Sputtering System

The magnetron sputtering system used was an AJA International ATC Orion. It possesses a configuration on-axis with three magnetron sputter guns for two modes sputtering process: direct current (DC) and radio frequency (RF) magnetron, as shown in Figure 55a. Some of the main features in this sputtering system are identified on that figure. This system can deposit all types of materials such as an electrical conductor and dielectrics. Electrically conductive materials, such as the fabricated targets and aluminum in this case, typically use a DC power source, in which the target acts as the cathode in a diode system [81]. Sputtering of dielectrics, such as

ceramic materials, and more specifically aluminum diboride ( $\text{AlB}_2$ ), requires an RF power source to supply energy to the argon atoms. Figure 55b shows two fabricated targets on the two DC guns and the  $\text{AlB}_2$  target on the RF gun.

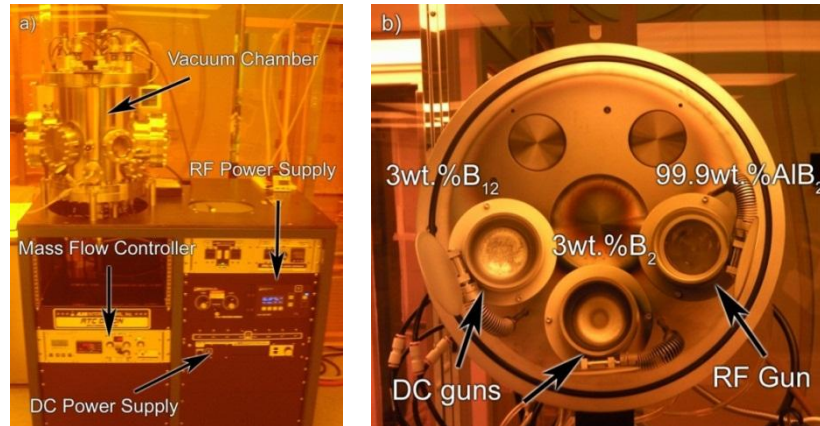


Figure 55 Sputtering System Description.

### 5.3. Sputtering Process

The thin films are deposited via sputtering (physical vapor deposition), a process by which a thin film of material (in the present case the aluminum matrix composite) is deposited on a substrate (polymer). The sputtering process follows a sequence of steps: 1) the material to be deposited is converted into vapor by physical means (a magnetron); 2) the removed atom is transported across a region of low pressure from its source to the substrate (polymer); and 3) the vapor undergoes condensation on the substrate to form the thin film..

### 5.4. Experimental Setup

As mentioned in Chapter 2, sputtering is a deposition technique that uses energetic ions, typically  $\text{Ar}^+$ , to bombard the target. In the process, atoms are knocked loose from the surface of

the target and are transported to the substrate where deposition occurs. Figure 56 shows the open window front view of the sputtering equipment as the sputtering process takes place.

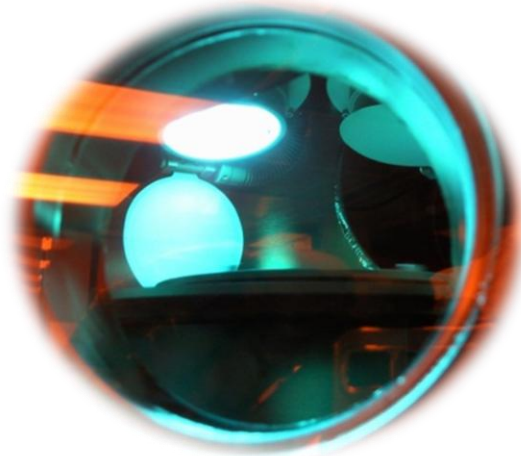


Figure 56 Photograph of Sputtering Process.

## **5.5. Selection of the Target Material**

In order to produce the thin films, five targets were selected to be tested in the sputtering equipment. Four of them came from the fabricated targets via centrifugal casting and the other was purchased from AJA International (aluminum target) for comparison purposes. The centrifuged targets were selected because of their improved higher concentration of particles.

The tested targets are listed below:

- Al-2wt.%B<sub>2</sub>-3wt.Si zone 1
- Al-3wt.%B<sub>2</sub>-3wt.Si zone 1
- Al-2wt.%B<sub>12</sub>-3wt.Si zone 2
- Al-3wt.%B<sub>12</sub>-3wt.Si zone 2
- Pure aluminum

Note that the pure aluminum film was intended as a reference, not as a potential final material.

## 5.6. Deposition Parameters and Fabrication Process of the Films

There are many parameters involved in the deposition of films by magnetron sputtering and the complex interrelations among all these parameters require them to be adjusted carefully in order to optimize the quality of the films. For this work, the optimization of the deposition parameters was based on the work of Barron [22]. Afterwards, these parameters were adjusted to the specific necessities and the sputtering setup used in this work. The sputtering parameters used for the present thesis are shown in Table 7.

Table 7 Sputtering Parameters.

Discharge power	200 to 450 W
Argon mass flow	12.8 sccm
Sputter pressure	2 mTorr
Pre-sputtering time	5 min
Sputtering time	30 min

First, the films were deposited onto glass slide substrates for the characterization of the film without the presence of the polymer. The samples were left 7 to 9 hr (determined experimentally) in vacuum to avoid aluminum oxidation on the films. The distance between the substrate and the target guns was 44 cm and the rotation velocity of the substrate was 40 rpm. In order to test the selected targets, the main focus of this approach was initially to determine at which discharged power the constituents present in the targets are being effectively deposited.

For the films containing the polymer substrate, the same sputtering parameters were used but the power adjustment. Here, the target materials were deposited at a maximum power of 450W (determined experimentally Chapter 6). It is known that sputtered films deposited with high deposition rates at low pressure are linked to high specular reflectance, as the compressive

films deposited under the conditions presented in Table 7 provide low surface roughness values and uniform grain structure [22].

## 5.7. Thin Film Characterization

Analytical techniques utilized for this work can be divided into two categories:

- Morphological analysis: Techniques for investigating the microstructure of thin films, specifically grain size, grain structure, film thickness, and surface topography.
- Mechanical properties study: Mechanical responses of the material based on the morphology, chemical composition, and fundamental structure of the thin film.

The following subsections contain an overview of each analytical technique employed for this study, brief discussions of the pertinent theory as well as equipment details.

### 5.7.1. Experimental Procedure

Figure 57 shows the films characterization steps followed in this thesis.

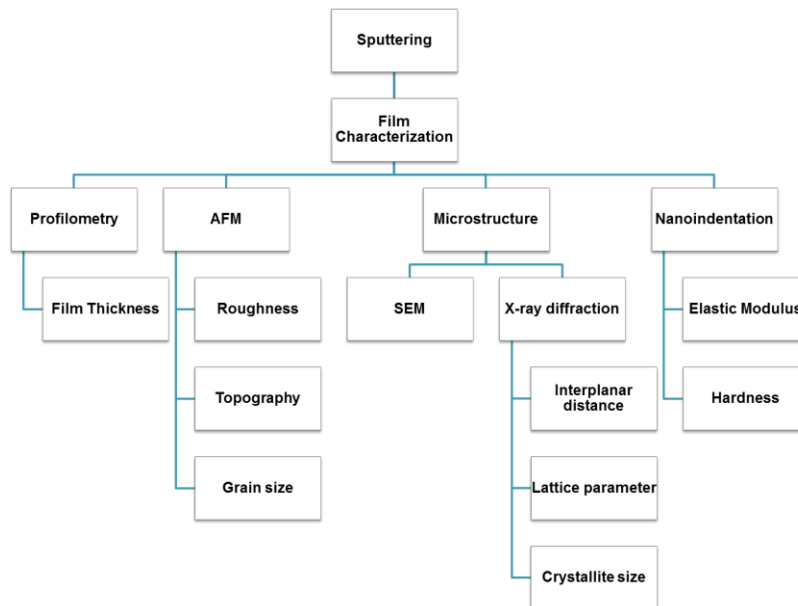


Figure 57 Experimental procedure flow chart of film characterization.

## **5.7.2. Morphology:**

### **5.7.2.1. Thickness Measurement**

The film thickness of metals is generally more difficult to measure than insulating thin films. Insulating thin films are semitransparent, thus can be easily measured using optical techniques such as spectroscopy, interferometry, and ellipsometry [46]. As a result non-optical techniques such as x-ray reflectivity (XRR), ultrasonic laser sonar, and profilometry are employed [46] in metals. Of the above techniques, profilometry is most commonly used in laboratory applications due to its fast and cost effective operation.

Profilometry describes a class of techniques for measuring surface topography. A probe, typically a sharp diamond-tipped stylus or a laser, is scanned across a sample surface in a straight line. Stylus based profilometers can be accurate to a resolution of roughly 1 nm. The primary drawback to the profilometry technique is that a step must be patterned into the film to allow for the measurement of film thickness.

The equipment used in this work, shown in Figure 58, is a Tencor P6 stylus profilometer system with a maximum scan length of 200 mm and a z-axis resolution of 2.5 nm.

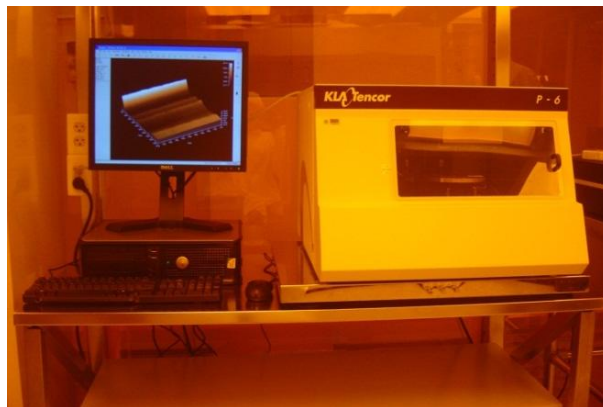


Figure 58 KLA Tencor P-6.

### 5.7.2.2. Atomic Force Microscopy

In an atomic force microscope (AFM) the height movements of the probe are used to reconstruct an image of the sample surface with resolution on the order of an angstrom. For an AFM the sharp tip is mounted on a cantilever. The tip is fabricated from silicon nitride of single crystal silicon, and is mounted to a silicon cantilever [82]. The equipment used to perform this task is shown in Figure 59. In this thesis, the AFM was used to measure the roughness, grain size and topography of the fabricated thin films.

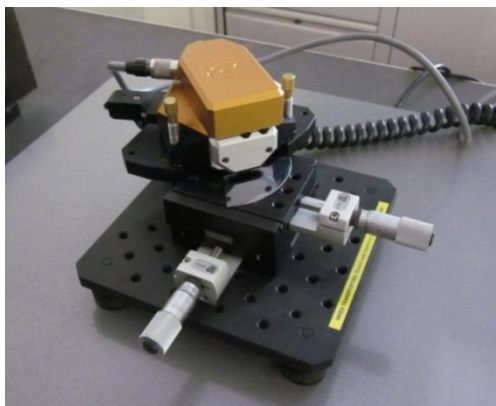


Figure 59 Photograph of the EasyScan atomic force microscope.

### 5.7.2.3. X-ray Diffraction

X-ray diffraction was used to determine the constituent phases present in the films. Also, the interplanar distance, the lattice parameter, and the crystallite size were measured from the sputtered films with this technique. To calculate the interplanar distance ( $d$ ) Equation 2 was used. The lattice parameter ( $a$ ) was determined with Equation 3 and the crystallite size was calculated with the Scherrer equation shown in Equation 4.

$$d = \frac{\lambda}{2\sin\theta}$$

Equation 2

$$a = d\sqrt{h^2 + k^2 + l^2}$$

Equation 3

$$t = \frac{0.9\lambda}{B\cos\theta}$$

Equation 4

where, the  $\lambda$  is the  $K\alpha$  wavelength of Cu (0.154178 nm) and  $\theta$  the diffraction angle in radians,  $(h,k,l)$  are the Miller indices of the corresponding plane and B is the full width at the half maximum of the representative peak. The equipment used for this analysis was previously described in Chapter 3.

### **5.7.3. Mechanical Characterization: Nanoindentation**

Indentation techniques such as the Knoop and Vickers techniques have been commonly used to measure microscale hardness of materials [45]. These techniques are not sufficient for many thin film studies due to the required large sample thickness. The nanoindentation technique was previously discussed on Chapter 3. Here, the elastic modulus of the newly-developed composite is of particular importance because this is a key parameter in determining the resonant frequency of MEM resonators.

## **Chapter 6: Results and Discussion**

---

This chapter includes the preliminary characterization of the thin films obtained via sputtering. These films were fabricated and characterized, as discussed in Chapter 5. Profilometry, AFM, XRD, SEM and nanoindentation were the equipment and/or techniques used to complete the microstructure and mechanical characterization of the films. This film analysis also covered basic characterization of the SIBS polymer for better understanding of some polymer properties and for comparison purposes.

As mentioned in Chapter 5, glass substrates were selected for the first stage of the study upon which the aluminum films were deposited. Therefore, the purpose of this preliminary analysis was to characterize the film deposited on the SIBS and on other substrates.

### **6.1. Morphology and Thickness Measurement**

As mentioned in Chapter 5, film thickness was measured with a Tencor T6 profilometer. The scans were completed at five different locations along the film step. As mentioned in the previous chapter, in order to measure the film thickness a masking vacuum tape was used to cover some area of the substrate. When the tape was removed the film had a step where the tape impeded the deposition (shadowing). The length of the profile scan, 20,000  $\mu\text{m}$ , was selected to eliminate the effect of the shadow resulting from the presence of the vacuum tape used to produce the film step. Figure 60 shows the deposited film thickness as a function of the sputtering power. Pure aluminum films were thicker than the boride-containing films due to the difference in preferential sputtering. Also, the increase in boron percent decreased the film thickness for the same sputtering power level. Additionally, the films produced with the targets

containing diboride particles were thinner than dodecaboride-containing ones obtained at the same power level.

This behavior could be explained considering the difference in preferential sputtering of the constituents of the target material. Preferential sputtering can occur at the start when a multicomponent solid target is bombarded and there is no solid state diffusion. If the energy transfer is more efficient to one of the target components, and/or it is less strongly bound to the solid, it will sputter more efficiently than the other [83]. The difference in the preferential sputtering strongly depends on the binding energy of the components of the target. In the literature we found that aluminum has higher sputtering yield than boron and silicon which implies that at that deposition rate aluminum would deposit faster than silicon and much faster than boron. The presence of boron in the fabricated targets is on the form of  $\text{AlB}_2$  and  $\text{AlB}_{12}$  particles, which led us to infer that aluminum borides will deposit faster than silicon.

Afterwards, in order to support these findings we analyzed the target surfaces (after sputtering) of the pure aluminum and the fabricated targets using SEM. This gave us better idea of what was occurring on the targets that helped understanding the difference in sputtering yield; which was responsible for the difference in film thickness. Figure 61 shows SEM micrographs of the sputtered zone from the targets after 200, 250, 300, 350, 400 and 450 W for 30 min of discharge power.

The aluminum target (Figure 61a) showed a uniform surface when compared with the targets containing boride particles. Figure 61 b and c show the effect that the boride particles had during the sputtering process; the aluminum grains surround the boride particles are almost completely removed from the target and the boride particles seem to be less affected by the ionized Ar. Figure 62 shows the magnified region presented in Figure 61c where one could

appreciate the plasma erosion of the boride particles. These figures were the first evidence that indicate we could be depositing boride nanoparticles on the thin films.

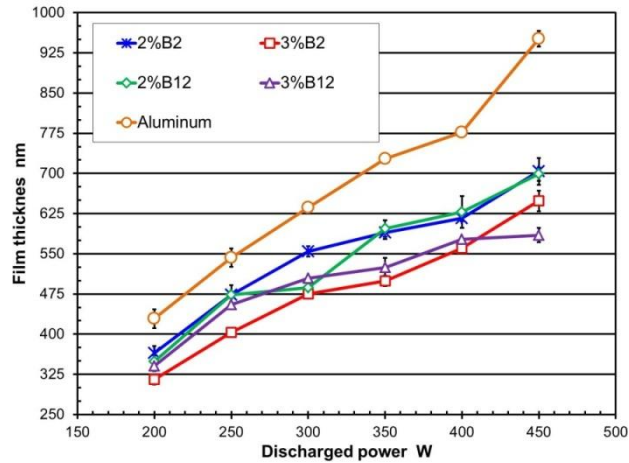


Figure 60 Film thickness as function of the discharged power.

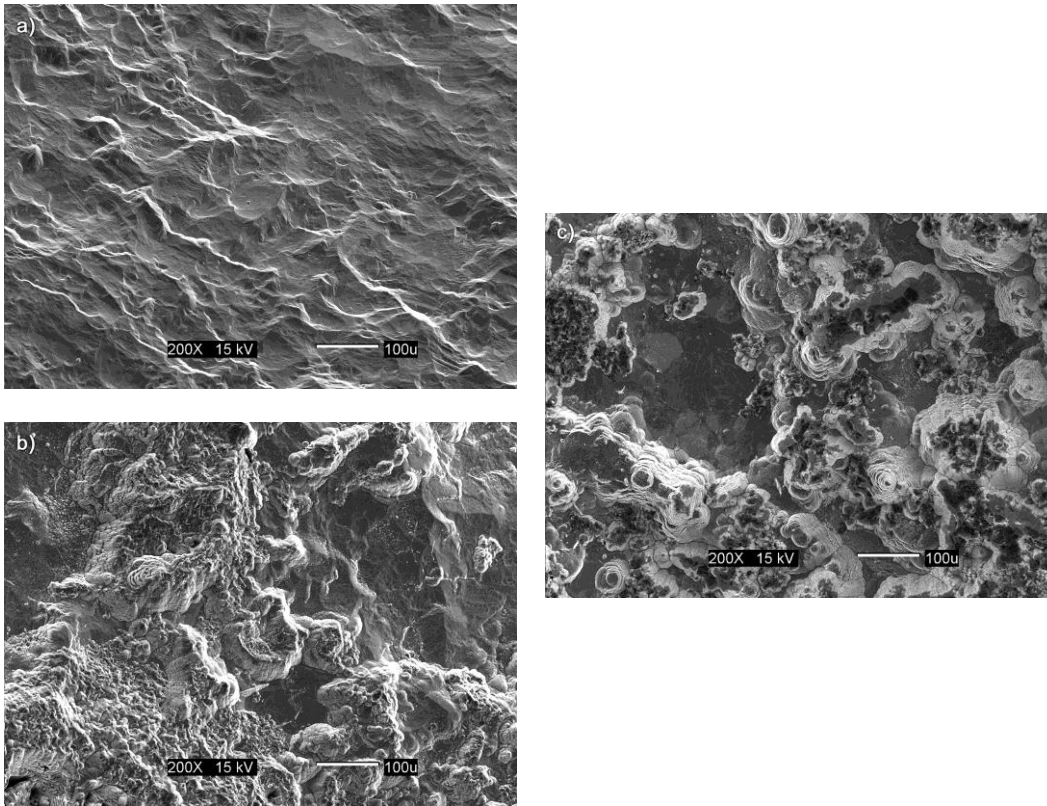


Figure 61 SEM micrographs of the targets used after sputtering: a) aluminum; b) diboride containing target material c) dodecaboride containing target material.

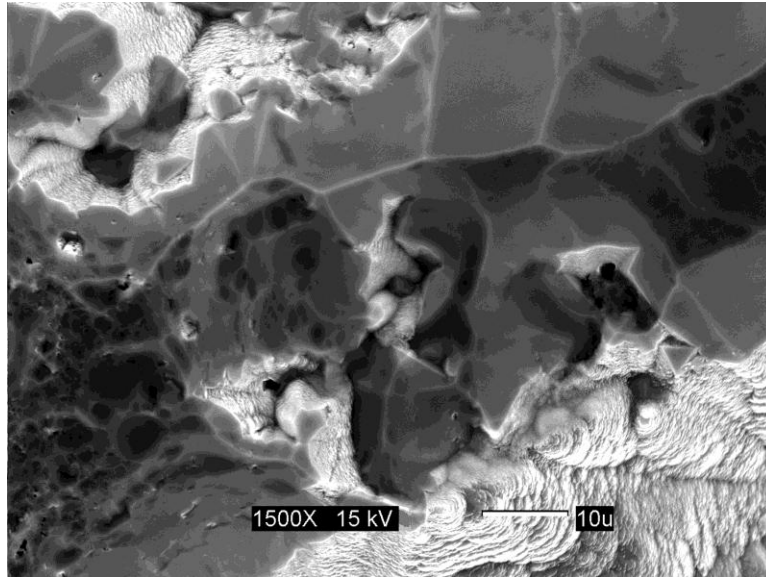


Figure 62 Dodecaboride particle eroded by the Ar plasma during the sputtering process.

## 6.2. Film Roughness

Nowadays the progressive reduction in size in electronic devices requires smoother surfaces that could stand large electrical current densities. For this reason surface roughness of metallic thin films are of a great importance, from a fundamental point of view as well as from application perspectives.

Surface roughness is a measure of the texture of a surface. It is quantified by the vertical deviations of a real surface from its ideal flat form. If these deviations are large, the surface is rough; if they are small the surface is smooth. Roughness is typically considered to be the high frequency, short wavelength component of a measured surface [84].

Onoda et al. determined that the roughness of the underlying substrate can be transferred to sputtered aluminum thin films and manifested itself in the reflectivity of the film [85]. Additionally, depositions of identical films onto different substrate materials resulted in varying

grain size, resistivity, stress, and hardness [86]. The crystal orientation of the underlying substrate can also alter the preferred grain orientation of the sputtered films [46].

Roughness plays an important role in determining how a real object will interact with its environment because it influences the resistivity, reflectivity, performance and quality of the produced films. For that reason, in this part of the thesis we focus on the surface roughness expressed as root mean square (RMS) as measured by the AFM equipment described in Chapter 5.

### **6.2.1. Surface Roughness of films deposited over glass substrates**

AFM images were produced at the maximum allowable area of the equipment, i.e.  $12,186 \mu\text{m}^2$ , and on the films deposited over glass substrates with a load of  $25\mu\text{N}$  to measure the surface roughness of the deposited films. Five scans were used to this purpose. The roughness was measured for films produced with six deposition discharge power levels: from 200 to 450W. Figure 63 shows the measured surface roughness of the films deposited over glass slides as a function of the discharge power. As expected, the roughness of the deposited films decreases as the discharge power increases for almost all of the targets used. This figure revealed that the aluminum films possess the lowest roughness values while the highest roughness values are in the films produced by targets containing dodecaboride particles (Al-Si/AlB<sub>12</sub>). Lower surface roughness was observed on the films made with the diboride-containing target than the dodecaboride-containing films. This analysis was performed in order to obtain the power discharge that results in the lowest roughness values, in this case, 450W. Figure 64 shows characteristic AFM images of the scans used to measure surface roughness of films produced with targets of pure aluminum, Al-Si/AlB<sub>2</sub> and Al-Si/AlB<sub>12</sub> at various powers discharged.

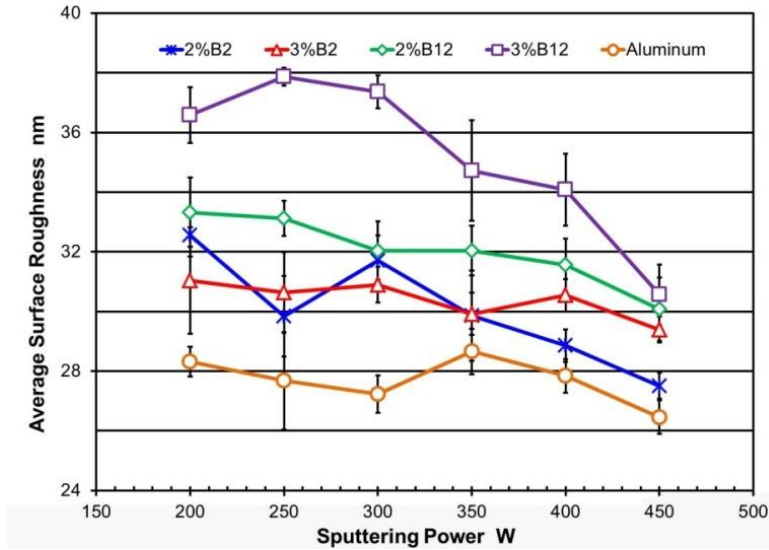


Figure 63 Roughness of the film deposited.

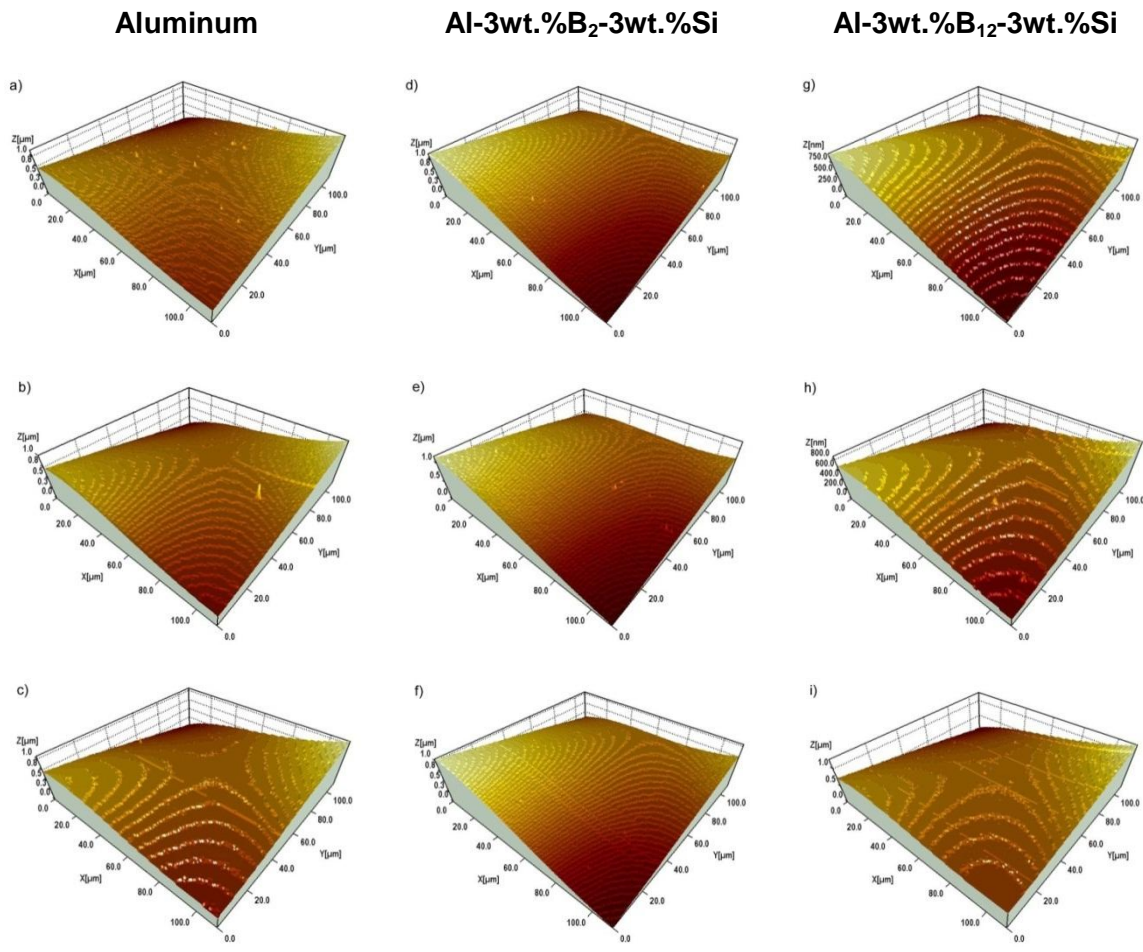


Figure 64 Summary of AFM image of films surfaces used for roughness measurements.

### 6.2.2. Surface Roughness of Films Deposited on the Polymer Substrate

From the previous section, 450 W was the power discharged upon sputtering that was selected to deposit the films using SIBS as substrate. The roughness of the polymer was measured to reveal the effect of the substrate surface morphology on the films. The results of the roughness analysis are shown on Figure 65, which indicates that the pure aluminum film presented the lowest roughness value despite (or counteracting) the roughness of the polymer while the films produced with the fabricated composite targets showed the higher surface roughness.

Figure 65 also shows that roughness increases with the percent of boron (and, as a consequence, boride particles) present in the target material. When comparing these roughness values with the ones obtained on glass substrates at the same discharged power, the results reveal that the polymer substrate almost doubled the film roughness values.

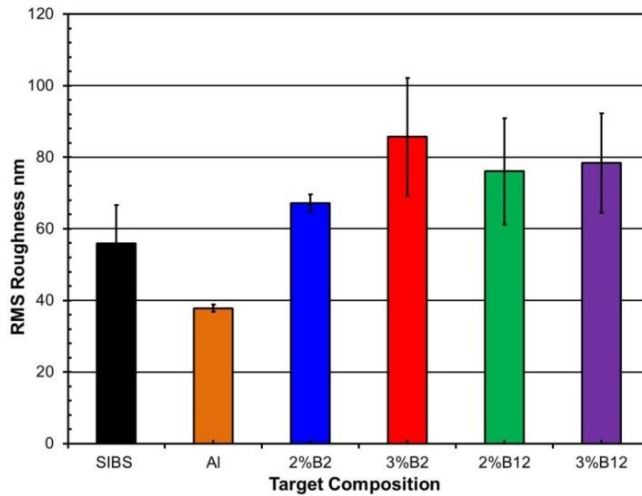


Figure 65 AFM-measured RMS roughness values for sputtered alloys.

The AFM scans on films deposited on SIBS substrates at 450W (Figure 66) corroborated that pure aluminum films are smoother than the other two films; this is mainly due to the higher film thickness. Diboride- and dodecaboride-containing films have higher surfaces irregularities

relative to the roughness increment found in Figure 65. The literature indicates that the high rate of deposition causes relatively low levels of gas impurity incorporation into the aluminum film. Grains tend to be small, with domed surface topography and low levels of surface roughness [46].

Moreover, the topography of the substrate does affect the structure of the deposited thin film. This behavior was observed on the films deposited over the glass slides and was assumed that at this power discharge the film deposited over the polymer substrate will also show lower surface roughness.

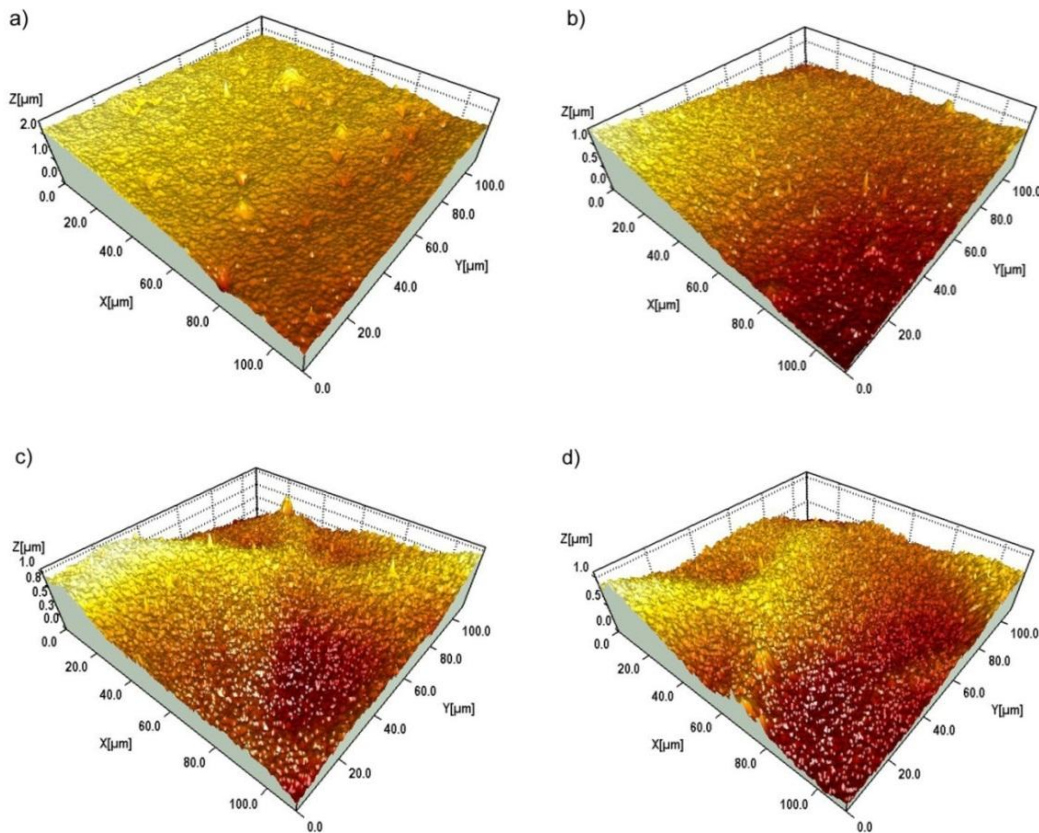


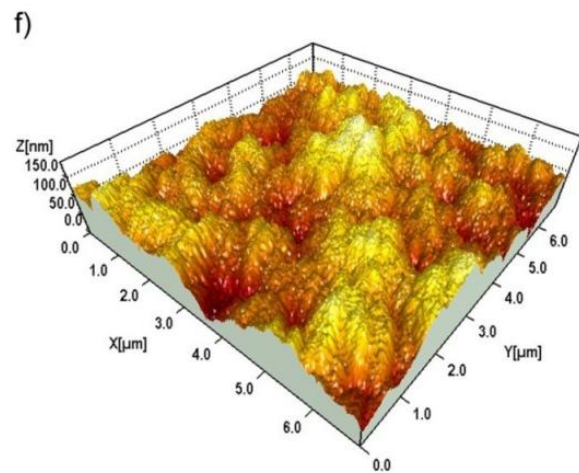
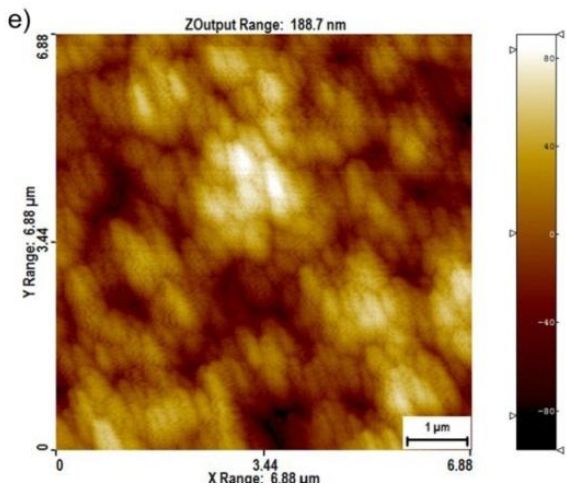
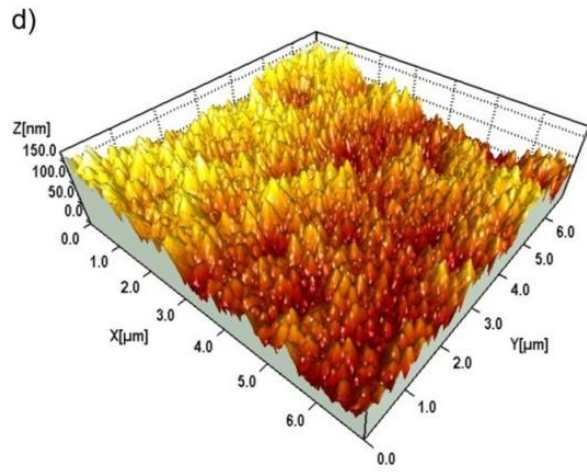
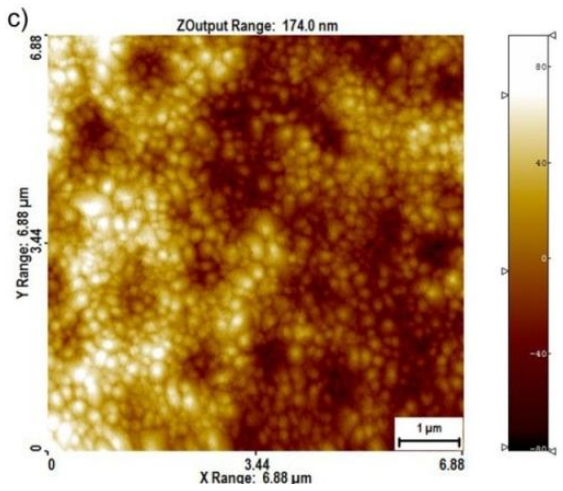
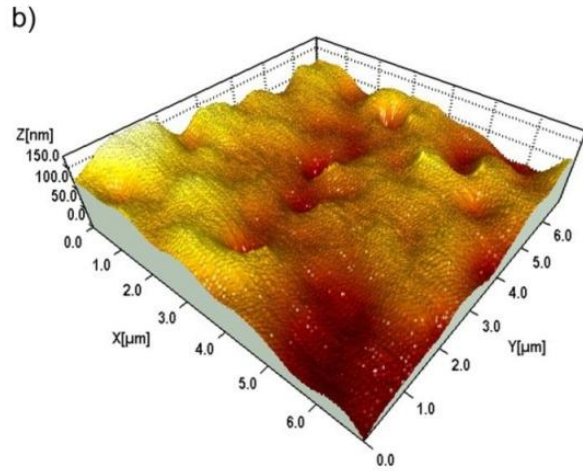
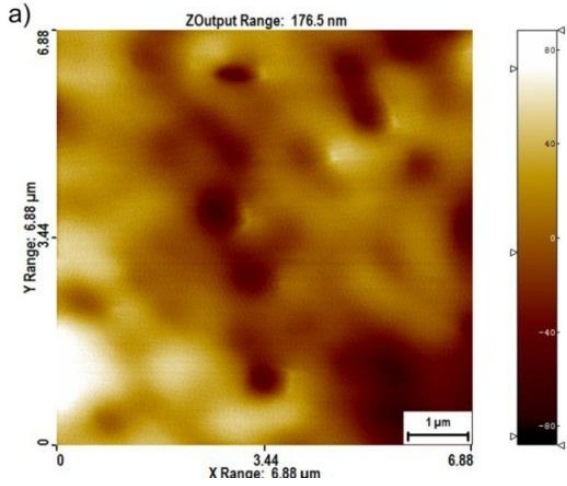
Figure 66 Surfaces AFM images of: a) SIBS film, b) aluminum film, c) Al-Si/AlB<sub>2</sub> film and d) Al-Si/AlB<sub>12</sub> film.

### **6.3. Films Topography Study Using AFM**

Figure 67 a through h show AFM images of the films topography as deposited on the SIBS polymer. To maximize the instrument x-y resolution the scans were performed over a  $47.3 \mu\text{m}^2$  area (minimum allowed by the instrument) with a z-range of  $0.313 \mu\text{m}$  and a load of  $25 \mu\text{N}$ . The AFM analysis permitted to detect the presence of pores in the deposited films. Figure 67a shows the polymer topography (i.e. prior to deposition), where the presence of pores is evident and Figure 67b shows an isometric view of the surface in Figure 67a. Those pores, which result from the evaporation of toluene and hexilalcohol (solvents) through the SIBS curing process, have an impact on the film surfaces where deposition occurs.

Figure 67 c through d show AFM images of the films obtained with the pure aluminum target (control specimen). These figures indicate that the resulting aluminum film consists of small grains of about  $150\text{nm}$ . Figure 67 e through f show the top view of the film surface obtained using the  $\text{Al-3wt.\%B}_2\text{-3wt.\%Si}$  target and its isometric view, respectively. These figures revealed that this film has a larger grain size than the pure aluminum film. Moreover, the film topography obtained from the  $\text{Al-3wt.\%B}_{12}\text{-3wt.\%Si}$  target is very different from the one obtained with the pure aluminum and the dodecaboride-containing targets.

Figure 67 g through h show grains that cannot be clearly resolved with the AFM equipment. It is possible that the film is somewhat amorphized. Also, Figure 67 e through f and Figure 67 g through h do not have enough resolution when compared to the images obtained from the aluminum target, a decrease in electrical conductivity of the film could be the reason of that phenomenon due to the presence of the polymer.



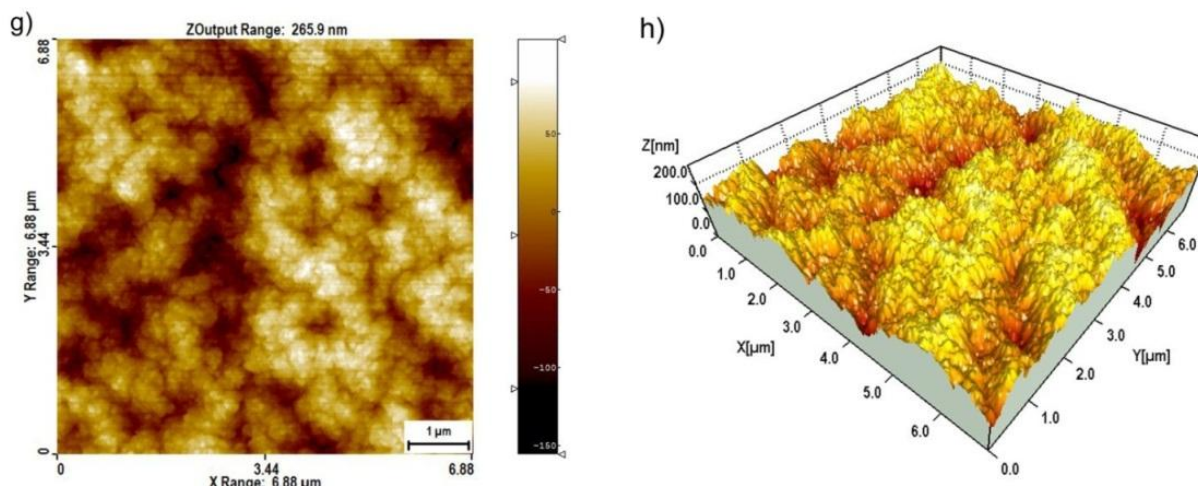


Figure 67 Topographical AFM images of polymer substrate and films produced via sputtering, a) SIBS image: b) perspective image of (a): c) Aluminum film image: d) perspective image of (c): e) Al-Si/B<sub>2</sub> film image: f) perspective image of (e): g) Al-Si/B<sub>12</sub> film image: h) perspective image of (g).

#### 6.4. X-Ray Diffraction Analysis

The films deposited over glass slides were not useful for the analysis of the diffraction patterns because the film thickness was much lower than the thickness of the substrate and the x-rays penetrated through the film. As a result, only the signal of the amorphous material showed up in the diffraction patterns. For this reason, the films were also deposited over (111) silicon wafers to improve the diffraction profiles of the produced films. According to the literature, silicon wafers are not proper substrates for aluminum because that the FCC metal does not attach to the silicon wafer; the literature suggest to deposit first a thin layer of chrome or to grow silicon oxide in order to favor the aluminum/silicon attachment [87]. Nonetheless, in the present research we discovered that the films produced with the composite targets attached well to the bare silicon wafers. Here we can speculate that constituents of the aluminum alloys improve the adhesion with the silicon wafer.

#### **6.4.1. XRD: Silicon Substrates**

The analysis of the films deposited over silicon substrates was performed with a Rigaku Ultima III XRD with the focus modulus. The specimens were analyzed from the  $2\theta$  range 10 to  $60^\circ$ . All the films had a dominant (111) orientation characteristic at  $38.474^\circ$  for pure aluminum. For this reason we only focus in the analysis of that peak. Figure 68a-b show the diffraction profiles of the produced films while, Figure 68a displays the diffractogram obtained from to the aluminum target and Figure 68b shows the diffraction profiles of the films produced with the fabricated targets.

The (111) aluminum peak (Figure 68) is slightly shifted to the left (lower  $2\theta$ ), while in the films produced with the composite target the same Al peak shifts to the right (Figure 68). These shifts could have caused by the stresses present in the films. It could be infer that the aluminum film showed tensile stress while the films produced with the fabricated targets has a compressive stress [88].

Additionally, the aluminum peak showed larger and thinner peak when compared to the shorter and wider peaks of the films produced with the fabricated targets (for the same step size and dwelling time in the diffractometer). Also, the peak intensities were higher on the aluminum film, for this reason they are presented on separated graphs. The film fabricated with the Al-Si/2wt.%AlB<sub>2</sub> target showed the weakest (111) peak of all samples. The reduction of the (111) peak is an indicator of increased disorder in the film. The peak intensity reflects the total scattering and is directly dependent on the distribution of particular atoms in the structure.

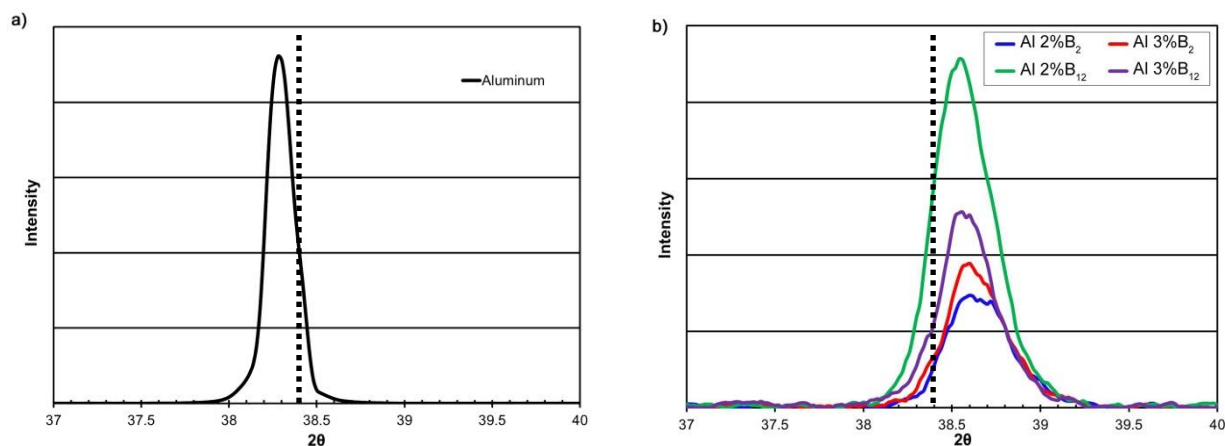


Figure 68 Diffraction profiles of the films deposited over the silicon substrates: a) aluminum target and b) fabricated targets.

In order to verify this, the interplanar distance ( $d$ ), the lattice parameter ( $a$ ) and the crystallite size of the fabricated films were measured for the (111) peak. The results are summarized on Table 8. Higher interplanar distance, lattice parameter and crystallite size were observed in the aluminum film, while the films produced with the fabricated target has half the crystallite size and lower values of interplanar distance and lattice parameters. From literature, it was expected that the aluminum film showed higher crystallite size because it's higher film thickness [89]. Table 8 shows the calculated value of the aluminum standard for comparison purposes evaluated also at (111) peak. The measured lattice parameter of the aluminum and Al-Si/3wt.%AlB<sub>2</sub> films were 0.4072 nm and 0.4038 nm showed the largest deviation in lattice parameter when compared to the value of 0.4049 nm reported for pure aluminum. This is indicative of strain imparted on the lattice by the residual stress mechanisms. Additionally, the Al-Si/2wt.%AlB<sub>12</sub>, Al-Si/3wt.%AlB<sub>12</sub> and Al-Si/2wt.%AlB<sub>2</sub> showed the lower deviation in lattice parameter.

From these results, it is expected that there will be some systematic error in the reported lattice parameter, regardless of how exact the sample orientation is in the sampler holder. To avoid

this, it is common to fit the lattice parameter to 5 or more peaks, but this was not done in this case.

Table 8 Computed Al lattice parameters of the sputtered films.

Film peak (111)	2 $\theta$ (degree)	d (nm)	a (nm)	crystallite size (nm)
Al	38.279	0.2353	0.4072	55.4093
Al-2%B <sub>2</sub>	38.581	0.2335	0.4042	25.1758
Al-3%B <sub>2</sub>	38.619	0.2333	0.4038	25.1771
Al-2%B <sub>12</sub>	38.559	0.2337	0.4044	25.2401
Al-3%B <sub>12</sub>	38.579	0.2335	0.4042	26.7884
Aluminum Standard	38.474	0.2342	0.4048	----

#### 6.4.1.1 Comparison between AFM analysis and the measured crystallite size

3.5  $\mu\text{m}$  X 3.5  $\mu\text{m}$  AFM images were used to generate estimates of grain size for each film as shown in Figure 69a-c. The pure aluminum film has grains that are approximately 250 nm in diameter. The films produced with the fabricated targets exhibit almost a 25% reduction in grain size. When comparing the crystallite sizes calculated via the Scherrer equation and the images obtained with AFM, it is possible to see that there is a significant difference between them. The AFM images showed higher grain size. This could be due to the lack of resolution of the equipment; while the Scherrer equation showed lower grain size values, AFM images might not clearly shown the grain size of the films, but they serve as a good tool for the qualitatively comparison between them. The AFM images corroborate the pure aluminum film with higher grain size and the Al-Si/2wt.%B<sub>12</sub> with the smaller grain size.

Since the Scherrer technique is based on the broadening of XRD peaks, it requires the assumption that crystallite size is the only parameter contributing to line broadening. However, all deposited thin films exhibit some magnitude of residual stress, an additional parameter that causes line broadening. To eliminate the two parameters, the analysis of multiple XRD peaks is

necessary. This was not done for this dataset, thus some underestimation of crystallite size is expected. Moreover, the AFM images could be used for qualitatively comparison purposes, where they corroborate the tendency to decrease grain size when the boride particles are present.

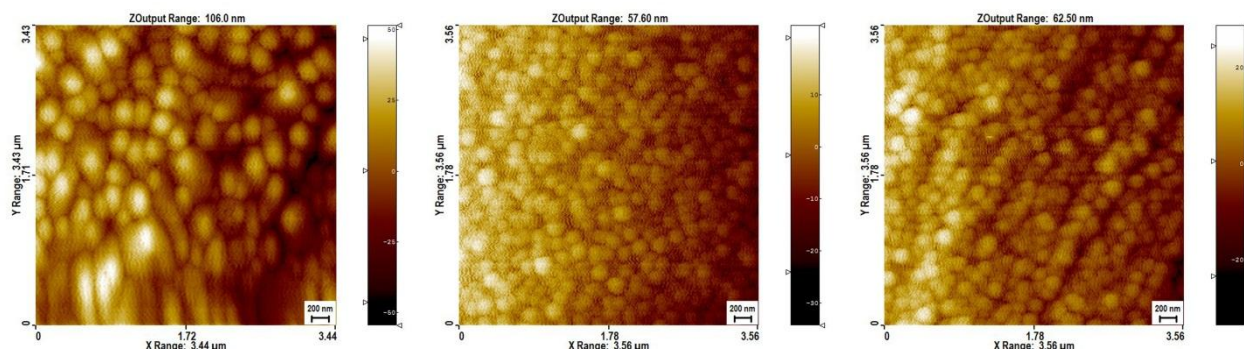


Figure 69 AFM images of the films deposited over silicon wafers: a) aluminum; b) Al-Si/3wt.%AlB<sub>2</sub>; c) Al-Si/3wt.%AlB<sub>12</sub>.

#### 6.4.2. XRD: Polymer Substrate

The first X-ray diffraction experiments were completed on the films deposited over the polymer substrate. Three specimens with the same chemical composition were evaluated with the Siemens D500 diffractometer described in Chapter 3. First, the films were analyzed from 2θ range from 10° to 65°, as shown in Figure 70. The first peak corresponds to the SIBS and the second one to the (111) plane of aluminum from the sputtered films.

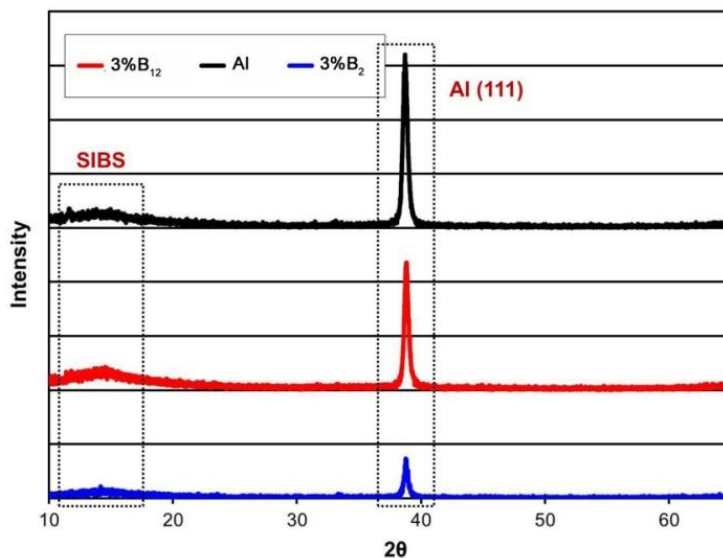


Figure 70 Characteristic peaks of the sputtered films deposited over SIBS.

Figure 71a and Figure 71b show the diffraction profiles of only the main aluminum peak, i.e. (111) plane, as evaluated within a small  $2\theta$  range. These diffractograms evince some aluminum amorphization in the films produced with the composite targets (Figure 71b). This amorphization occurs when there are extensive crystal imperfections on the small grain structure leading to the broadening of the aluminum peak. Nonetheless, we do not discard some peak broadening caused by lattice strain. To determine whether the peak broadening observed on the composite films was due to imperfections of the crystallites, a preliminary study of the crystal structure was performed with the data obtained from XRD. The interplanar distance, the lattice parameter and the crystallite size were calculated with the equations described in Chapter 6. The results are summarized in Table 9.

The results from Table 9 confirm the broadening of the diffraction profile due to imperfections of the crystallite size and also, showed the aluminum film with higher deformation in the lattice parameter. This deformation are in agreement with the results in Figure 71a where the sharp peaks originated by the (111) Al plane are shifted with respect to an Al standard (Joint

Committee on Powder Diffraction Files, JCPDF) shown in dashed lines. Based on considerations from the surveyed literature we believe that the peak shift is mostly caused by the film stresses [90]. Taking this into account, we could conclude that despite being deposited onto a polymeric membrane the pure aluminum film possess higher stresses than the composite films. This behavior was corroborated with the analysis performed over the films deposited on silicon wafers.

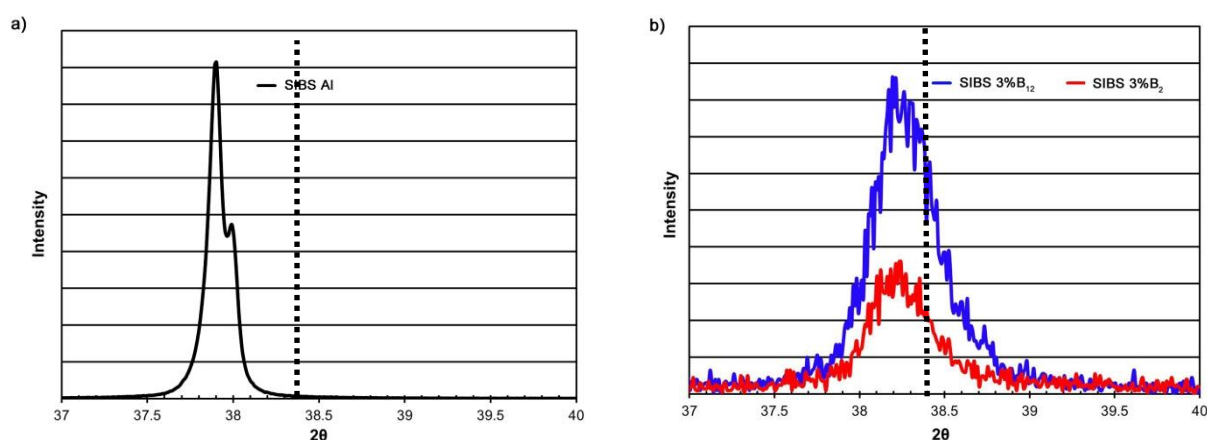


Figure 71 XRD of the films deposited over SIBS substrates: a) aluminum target and b) fabricated targets.

Table 9 Analysis of the diffractograms from films deposited on polymers substrates.

Film peak (111)	Angle (2θ)	d (nm)	a (nm)	crystallite size (nm)
Al	37.916	0.2371	0.4107	60.0085
Al-2%B <sub>2</sub>	38.599	0.2332	0.4040	23.0523
Al-3%B <sub>2</sub>	38.499	0.2338	0.4050	25.3649
Al-2%B <sub>12</sub>	38.541	0.2358	0.4084	24.5395
Al-3%B <sub>12</sub>	38.453	0.2341	0.4055	22.1113
Aluminum Standard	38.474	0.2342	0.4053	---

#### 6.4.2.1. Grain Size of Films Deposited Over Polymer Substrates

Characteristics images (Figure 72) taken at 65000x with a field emission SEM and analyzed with the Image J software were used to measure the grain size of the films deposited on

polymer substrates. Figure 72a shows the pure aluminum film populated with finer grains and bearing a well-defined grain structure. On the other hand, the films produced with the fabricated targets show irregular growth patterns in grains resembling flakes (Figure 72 b and Figure 72c). This figures were not useful for the calculation of the grain size, because of the irregularity of the grain from the films obtained from the fabricated targets. However, from the results of the crystallite size it is expected the pure aluminum to possess higher grain size while the films produced with the fabricated target bear the smaller grain size.

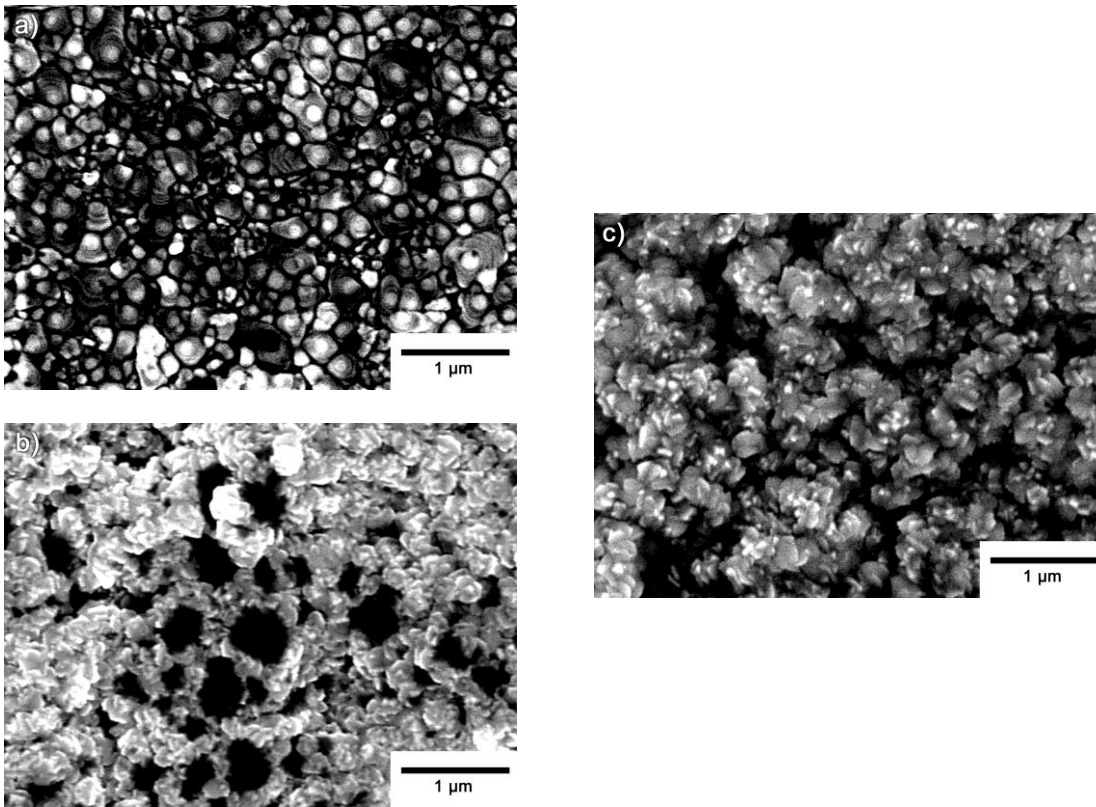


Figure 72 Characteristic field emission SEM micrographs used to measure the grain size of the produced films.

## **6.5. Mechanical Properties of the Deposited Films**

The indentation response of a thin film on a substrate is a complex function of the elastic and plastic properties of both the film and substrate and the compliance of the indenter material. The

standard methods that are used for extracting properties from the measured load–displacement data were developed primarily for monolithic materials [91]. These same methods are often applied to film/substrate systems for determining film properties without explicit consideration of how the substrate influences the measurements. In order to measure ‘film-only’ properties, a commonly used rule of thumb is to limit the indentation depth to less than 10% of the film thickness [91].

The mechanical properties of the deposited films were measured with the G200 nanoindentation system. From section 6.1 we used the measured data (film thickness) to perform 20 nanoindentations at 10, 15, and 20% of the film thickness. Considering that substrate influence nanoindentation results from thin film materials [92-94], we completed the nanoindentation analysis on films deposited on both types of substrates; glass slides and SIBS. The nanoindenter was operated in the continuous stiffness mode (CSM) for thin films and the indentations were made using a constant nominal strain rate of  $0.05 \text{ s}^{-1}$ . Poisson’s ratio was assumed to be that of aluminum, and all reported values are an average of twenty separate indentations.

It is important to mention that the approach presented hereby only uses the data output provided by the nanoindenter software without taking into account the raw data to perform a more intensive analysis of the elastic modulus and hardness obtained from the films. The following subsection includes the results of the nanoindentation analysis performed on the films deposited on glass substrates

### 6.5.1. Films on Glass Slide Substrates

Characteristic load vs displacement curves are shown in Figure 73. This figure shows the indentations performed with a maximum depth of 20% of the film thickness for films produced with the 3wt.% dodecaboride-containing target. As shown in Figure 74a and Figure 74b, the films produced with the composite targets possessed higher elastic modulus and hardness than the aluminum film. These figures also showed that the elastic modulus and hardness of the films slightly increased as the boron percent increased. Although, there is no physical evidence (via high resolution electron microscopy) of the presence of boride nanoparticles on the film microstructure, the results from the nanoindentation analysis and Figure 62 reveal that this increase in elastic modulus and hardness indicate that there is indeed presence of boride nanoparticles on the deposited films.

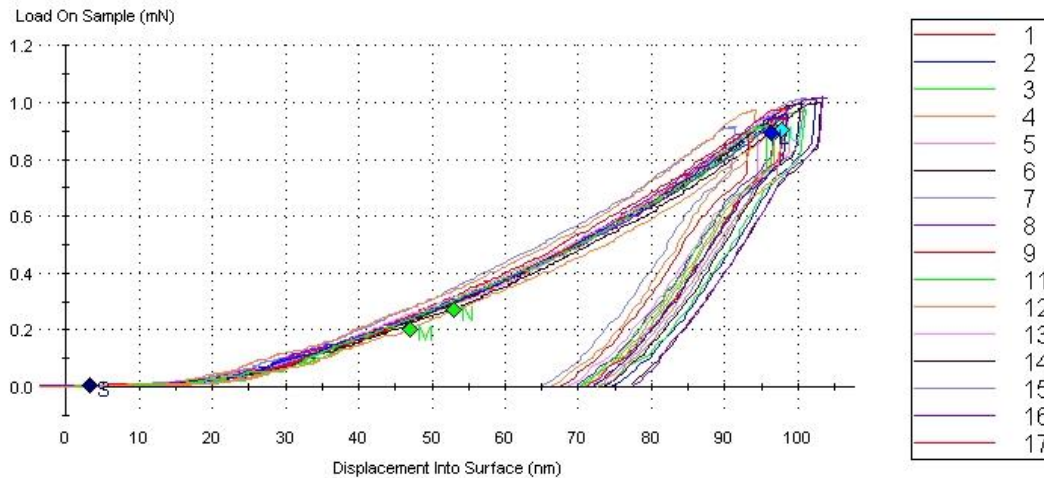


Figure 73 Characteristic load vs displacement curves for films produced with dodecaboride containing target.

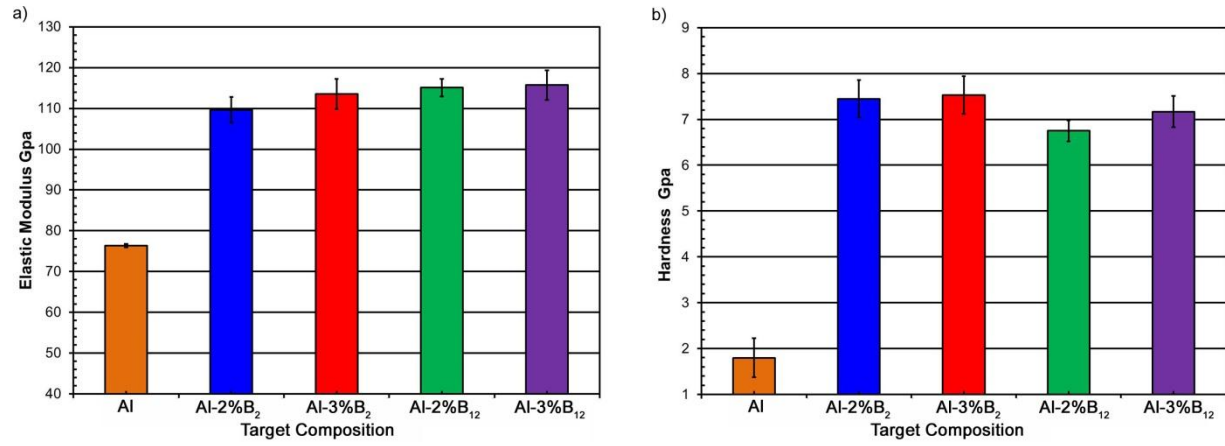


Figure 74 Nanoindentation results of the produced films deposited over glass slides substrates a) Elastic modulus and b) hardness.

## Chapter 7: Conclusions and Future Work

---

### 7.1 Conclusions

Al-B-Si sputtering targets were produced via centrifugal and vacuum casting. Centrifugal casting was selected as the main processing route because of the particular particle distribution that can be obtained from this casting technique. In effect, gradual particle segregation particle segregation was observed along the centrifugal force direction. Vacuum casting was selected as an alternative processing method and was used for comparison purposes in the present thesis. In this thesis we confirmed that for the new material system or composite centrifugal casting, with experimentally fine-tuned parameters, it was useful to segregate better the diboride particles than the dodecaboride ones. Also with this technique the physical and mechanical properties were improved compared with the vacuum cast samples. Additional important conclusions are as follows:

- Optical microscopy revealed that the measured volume fraction of the fabricated specimens showed samples containing aluminum diborides with higher particle density at zone 1 (zone of maximum centrifugal force) and samples containing dodecaboride particles with higher particle segregation at zone 2. This implies higher hardness in those zones. This behavior was then corroborated with measured values of Rockwell hardness.
- X-ray diffraction and EDS analysis confirmed the presence of the constituents on the composites. As expected, at least qualitatively, the presences of aluminum dodecaboride and aluminum diboride particles were confirmed using EDS analysis. On the other hand, one aluminum diboride peak was observed on x-ray diffraction while no peak was found for the dodecaboride containing samples. Stronger signals of aluminum and silicon were also observed on both techniques.

- The Rockwell hardness values for the diboride centrifuged samples were consistent with the trend observed when analyzing the particle volume fraction where they showed a tendency to increase along the centrifugal direction. As expected, the composites containing dodecaboride showed the higher Rockwell hardness values at zone 2 corroborating also the results obtained from the analysis of volume fraction. The Rockwell results of the vacuum cast samples showed Rockwell hardness values within the range of hardness values measured on the different zones of the centrifuged samples. Also Rockwell values were proportional to the increase of boron percent and diboride containing composites have higher Rockwell hardness values than dodecaboride specimens.
- Vickers microhardness values showed no significant variation between the different zones of the centrifuged samples and vacuum cast composites. Nevertheless, the specimens containing dodecaboride particles were found to have higher matrix microhardness than the  $\text{AlB}_2$  composites.
- Via nanoindentation the elastic modulus and hardness were determined on the matrix and particles of two characteristic samples of the centrifuged composites. The analysis performed on the matrix showed higher elastic modulus and hardness on the dodecaboride composite, corroborating the results obtained from the Vickers microhardness experiments of the matrix performed on the same specimens. Also, in both composites, a tendency to increase in those properties was found as the indents approached the borides particles. Moreover, when the results of elastic modulus and hardness obtained from the particle analysis were compared with experimental values found in literature, both sets of values appear to be in agreement.
- The measured grain sizes of the centrifuged specimens were larger (ASTM grain size) than the vacuum cast specimens. The difference between them is almost six ASTM

numbers. Smaller grain size values were obtained in zone 1 on the four compositions studied. This difference in grain size is attributed to both high centrifugal force and high rate of solidification caused by the high thermal conductivity of the graphite mold.

- DTA curves showed the presence of two endothermic peaks upon heating. The first peak corresponds to the presence of aluminum-silicon eutectic point and the other one to the Al matrix melting point. Here, no significant differences in thermal signals were discovered between the centrifuged and vacuum cast samples. In general, the matrix melting range was reduced up to 3% to 7%, as it was affected primarily by the amount of silicon in the matrix.
- CTE was determined with a thermo-mechanical analyzer for the fabricated composites. The centrifuged samples at the zone 1 displayed a smaller coefficient of thermal expansion compared to the other zones and the vacuum cast specimens. This is due to higher concentration of boride particles on those zones because of the higher CTE of the reinforcements compared with the aluminum matrix.

Testing of the centrifuged targets was essential to this thesis because it was pertinent to prove the reliability of the target to be proposed for the MEMS industry. The targets were initially subjected to different discharging power in the sputtering system, in order to obtain optimum film quality. The surface roughness was the parameter selected to indicate what discharge power produced lower roughness values. Three types of substrates were used for this purpose: glass slides, silicon wafers and SIBS. Initially, silicon wafers were not selected as potential candidates for film substrates, because aluminum does not adhere well to the silicon wafer, but it was discovered that the fabricated targets possessed good adhesion with the wafer due to the presence of the other constituents in the target. The results of this preliminary characterization performed on the films are summarized below:

- The difference in sputtering yield of the components present in the fabricated targets showed to have significant impact on the difference in film thickness. The pure aluminum target has the higher sputtering yield when compared to the fabricated targets. Also, the dodecaboride-containing films showed higher film thickness than diboride specimens. Here, the difference in film thickness has an important role, as film thickness grows the effect of substrates decreases on the film properties because the structure of the underlying substrate can be transferred to film.
- To determine the optimum discharged power that results in lower surface roughness, the films were deposited varying the discharged power from 200 to 450W. The roughness analysis showed 450W as the discharge power with the optimum film characteristic. The films produced with the pure aluminum target are less rough than the films produced with the fabricated targets regardless of the substrates in which were deposited. This behavior was mostly attributed also to the difference in film thickness.
- The topography of the films deposited over the polymer substrate was measured with AFM and showed pure aluminum films with finer grains than the films produced with the fabricated targets. Also, from this analysis the AFM images obtained from the fabricated target did not show the same image resolution as the pure aluminum film. It was assumed that this behavior was due to decrease in the electrical conductivity of the film. This decrease might be due to the lower film thickness, which increases the effect of the polymer substrate, a dielectric material. The topography of the films deposited over silicon substrates showed the same trend, but the silicon wafers improved the image resolution of the AFM images. These AFM images films showed also the aluminum with more defined grain the films produced with the fabricated targets.
- X-ray diffraction was used to determine the crystal structure of the films. The results showed all the specimens to have a preferred (111) orientation of the aluminum peak.

The interplanar distance, the lattice parameter and the crystallite size were determined with this technique for films deposited over silicon and polymer substrates. The crystallite sizes corroborate measurements done on AFM images where larger grain sizes were observed in the pure aluminum films. Smaller crystallites were measured using the diffraction patterns of the fabricated targets. The films deposited over polymer substrate and produced with the fabricated targets showed some aluminum amorphization. Also the intensity of the (111) aluminum peak decreases as the boron percent increases in the films produced with the fabricated targets. This behavior is revealed through the broadening of the diffraction profiles and higher deformation of the crystallites.

- The elastic modulus and hardness of the films deposited over glass slides were higher on the film produced with the fabricated targets compared with pure aluminum films. Although there is no physical evidence of the boride nanoparticles on the films, the nanoindentation results suggest their presence.

This thesis successfully proposes the fabrication, characterization and testing of centrifuged Al-B-Si sputtering targets for applications in thin films. Although the films produced were preliminary characterized it is recommended to get a more refined and detailed analysis than the one performed here, in order to propose them as good candidates for MEMS applications.

## **7.2 Future Work**

As mentioned, this thesis includes three main stages: the fabrication, characterization and testing of sputtering targets. From these stages the ones that would need some optimization and future work are the characterization and testing ones. On the other hand, the fabrication stage was optimized experimentally and it does not need additional studies.

In terms of the characterization the specimens would require complementary research in the study of the mechanical properties with nanoindentation and finite element numerical methods in order to determine and corroborate what was discovered in Chapter 4. Also, to further understand the mechanical behavior of the fabricated composites it is recommended to perform impact, tensile, wear and fatigue test to corroborate those findings.

Additionally, in this thesis the fabrication and preliminary characterization of the sputtered thin films with the centrifuged targets (testing stage) were reported. However, this needs more extensive studies to achieve the full optimization of film quality. This could be completed by a subsequent annealing to decrease the film roughness and residual stresses. Also, with XRD we discovered that the films deposited over the silicon substrates showed film stresses in compression. This needs to be corroborated by analyzing the radio of curvature of the films using a profilometer technique.

Finally, the mechanical properties and the film adhesion of the films deposited over the polymer substrate need to be studied with nanoindentation in order to have a better understanding of the overall hybrid composite behavior.

## References:

1. Suresh, S., Mortensen, A., *Fundamentals of functionally graded materials : processing and thermomechanical behaviour of graded metals and metal-ceramic composites*. 1998, London: IOM Communications Ltd.
2. Watanabe, Y., Fukui, Y., *Microstructures and Mechanical properties of Materials Science*. Thermal Analysis of Solidification in a Centrifugal Casting for Composite Materials Containing Particle Segregation. Vol. 4. 2000. 51-93.
3. Kang, C.G., Rohatgi, P.K. , *Transient Thermal Analysis of Solidification in a Centrifugal Casting for Composite Materials Containing Particle Segregation*. Metallurgical and Materials Transactions, 1996. **27B**: p. 277-285.
4. Adelakin, T.K., Suárez, O.M, *Study of Boride Reinforced Aluminum Matrix Composites Produced via Centrifugal Casting*. Materials and Manufacturing Processes, 2011 [In print]. **26**.
5. WANG Kai., X.H.-s., ZOU, Mao-hua., LIU Chang-ming. , *Microstructural characteristics and properties in centrifugal casting of SiCp/Zr104 composite*. Journal of Transaction of Nonferrous Metal Society of China. , 2009. **19**: p. 1410-1415.
6. Melgarejo-Pinto, Z.H., *Fabrication and Characterization of Functionally Graded Al/AlB<sub>2</sub> Matrix Composites for High Wear Aerospace Application Using Centrifugal Casting*, in *Mechanical Engineering*. 2006, University of Puerto Rico, Mayagüez Campus: Mayagüez. p. 129.
7. Adelakin, T.K., *An Experimental Study of Aluminum Boride Particles Distribution in Centrifugally Cast Al/AlB<sub>x</sub> Composites*, in *Mechanical Engineering*. 2009, University of Puerto Rico, Mayagüez Campus: Mayagüez. p. 102.
8. Calderón, H.E., *Effect of Cyclic High Loading Rates on the Fatigue Strength of Aluminum-Based Composites*, in *Department of Civil Engineering*. 2009, University of Puerto Rico - Mayaguez Campus: Mayaguez. p. 117.
9. Suárez, O.M., *Mechanical Properties of a Novel Aluminum Matrix Composite Containing Boron*. Journal of the Mechanical Behavior of Materials, 2001. **12** (4): p. 225-237.
10. Mirkovic, D., Gröbner, J., Schmid-Fetzer, R., *Experimental study and thermodynamic re-assessment of the Al-B system*. Journal of Alloys and Compounds, 2004. **384**: p. 168-174.
11. Jackson, M.J., and Graham, I. D. , *Mechanical Stirring of Al-B alloys*. Journal of Materials Science Letters (1994). **13**: p. 754-756.
12. Nafisi, S. and R. Ghomashchi, *Grain refining of conventional and semi-solid A356 Al-Si alloy*. Journal of Materials Processing Technology, 2006. **174**(1-3): p. 371-383.
13. Nafisi, S. and R. Ghomashchi, *Boron-based refiners: Implications in conventional casting of Al-Si alloys*. Materials Science and Engineering: A, 2007. **452-453**: p. 445-453.
14. Lee, Y.C., et al., *The effect of grain refinement and silicon content on grain formation in hypoeutectic Al-Si alloys*. Materials Science and Engineering A, 1999. **259**(1): p. 43-52.
15. Melgarejo-Pinto, Z.H., Suárez, O.M, and Sridharan, K., *Wear resistance of a functionally-graded aluminum matrix composite*. Scripta Materialia, (2006). **55**: p. 95-98.
16. Warmuzek, M., *Aluminum-Silicon Casting Alloys Atlas of Microfractographs*. Vol. 1. 2004: ASM International. 1-9.
17. Rooy, E.L., *Aluminum Foundry Products*. ASM Handbook. 1990, Metal Spark, Ohio: ASM International. 1327.
18. Terwagne G., B., F., *Aluminium and silicon determination on two Si±Al sputter targets used for magnetron sputtering*. Nuclear Instruments and Methods in Physics Research 1999. **B 158** p. 683-688

19. Jeong, S.H., Kho, S., Jung, D., Lee, S.B., Boo, J.-H., *Deposition of aluminum-doped zinc oxide films by RF magnetron sputtering and study of their surface characteristics*. Surface & Coatings Technology, 2003. **174-175**: p. 187-192.
20. Kim, S.K., Ahn, Y.H., *Electrical resistance of Ti-B-Al-O thin films deposited by r.f. magnetron sputtering*. Thin Solid Films, 2000. **377-378**: p. 772-775.
21. Sirghi, L., Popa, G., Hatanaka, Y., *Heating of polymer substrate by discharge plasma in radiofrequency magnetron sputtering deposition*. Thin Solid Films, 2006. **515**: p. 1334–1339.
22. Barron, L.W., *High-Reflectance, Sputter-Deposited Aluminum Alloy Thin Films for Micro-Electro-Mechanical Systems*, in *Materials Science & Engineering Department*. 2005, Rochester Institute of Technology: Rochester, NY. p. 231.
23. Jones, R.M., *Mechanics of Composite Materials*. 2 ed. 1999, Philadelphia, PA: Taylor & Francis, Inc. 507.
24. Chawla, N., and Chawla, K.K., *Metal Matrix Composites*. 2006, United States: Springer Science + Business Media, Inc. 397.
25. Clayne, T.W., Withers, P.J., *An Introduction to Metal Matrix Composites*. 1993, Cambridge: Cambridge University Press.
26. Ray, S., *Review Synthesis of Cast Metal Matrix Particulate Composites*. Journal of Materials Science 1993. **28(20)**: p. 5397-5413.
27. Kaufman, J.G., Rooy, E.L., , *Aluminum Alloy Casting*. 2004, Materials Park, OH: ASM International. 325.
28. Cornell, R., and Bhadeshia, H.K.D.H. *Aluminum-Silicon Casting Alloys*. Phase Transformations & Complex Properties Research Group 1999 [cited; Available from: <http://www.msm.cam.ac.uk/phasetrans/abstracts/M7-8.html>].
29. Fjellstedt, J., Jarfors, A., and El-Benawy, T., *Experimental investigation and thermodynamic assessment of the Al-rich side of the Al-B system*. *Materials and Design*, (2001). **22**: p. 443-449.
30. Hofmann, W., Janiche, W., *The structure of aluminum boride, AlB<sub>2</sub>*. Z. Phys. Chem, 1936. **B31**: p. 214-222.
31. Giardini, A.A., Kohn, L. Toman, L., Eckart, D.W., *Boron: Synthesis, Structure and Properties*. 1960, New York: Plenum Press. 140-158.
32. Duschaneck H., R.P.J., *The Al-B (Aluminum-Boron) System*. Journal of Phase Equilibria, 1995. **15(5)**: p. 543-552.
33. Tondel, G.H., and Arnberg, L. , *Grain Refinement of Hypoeutectic Al-Si Foundry Alloys by Addition of Boron Containing Silicon Metal*. Journal of the Minerals Metals & Materials Society, ed. S.K. Das. 1993, Warrendale, PA, . 783-790.
34. Gröbner, J., D. Mirkovic, and R. Schmid-Fetzer, *Thermodynamic aspects of grain refinement of Al-Si alloys using Ti and B*. Materials Science and Engineering A, 2005. **395(1-2)**: p. 10-21.
35. Hirai, T., *Functional Gradient Materials*. Processing of Ceramics, ed. R.J.e.a. Brook. Vol. 17B. 1996, Weinheim, New York, NY. 293-341.
36. Ogawa, T., et al., *Theoretical study on fabrication of functionally graded material with density gradient by a centrifugal solid-particle method*. Composites Part A: Applied Science and Manufacturing, 2006. **37(12)**: p. 2194-2200.
37. Watanabe, Y., A. Kawamoto, and K. Matsuda, *Particle size distributions in functionally graded materials fabricated by the centrifugal solid-particle method*. Composites Science and Technology, 2002. **62(6)**: p. 881-888.
38. Fukui, Y., *Fundamental Investigation of Functionally Gradient Material Manufacturing System using Centrifugal Force*. Vol. 34. 1991: JSME International Journal. 144-148.

39. Mattox, D.M., *Handbook of Physical Vapor Deposition (PVD) Processing*. Film Formation, Adhesion, Surface Preparation and Contamination Control. 1998, Park Ridge, NJ: Noyes Publications. 878.
40. Usui, H., Tanaka, K. *Vacuum Deposition*. [cited; Available from: <http://www.tuat.ac.jp/~usuilab/English/depo.html>.
41. *Ion Plating Process*. 2004 [cited; Available from: [www.ocj.co.jp/english/products/coat\\_t/coat\\_t.htm](http://www.ocj.co.jp/english/products/coat_t/coat_t.htm).
42. Molhave, K., *DC Plasma Sputtering*, in *OpenSource Handbook of Nanoscience and Nanotechnology*, DCplasmaSputtering.jpg, Editor. 2009.
43. Smith, D.L., *Thin Film Deposition: principle and practice*, ed. S.S. Chapman, Suzane, W.B. 1995, United States of America: McGraw-Hill. 599.
44. Onishi, T., E. Iwamura, and K. Takagi, *Morphology of sputter deposited Al alloy films*. *Thin Solid Films*, 1999. **340**(1-2): p. 306-316.
45. Askeland, D., Phule, P. , *The Science and Engineering of Materials*. 5 ed. 2006: Thomson. 849.
46. Ohring, M., *The Materials Science of Thin Films*. 2 ed. Deposition and Structure. 2002, San Diego, CA: Academic Press. 783.
47. Onoda, H., Narita, T., Touchi, K., Hashimoto, K., *Effects of insulator surface roughness on Al-alloy film properties and electromigration performance in Al-alloy/Ti insulator layered interconnects*. *Journal of Vacuum Science B*, 1996. **14**(3): p. 2645-2665.
48. Lita, A. and J. Sanchez, *Effect of the underlayer on the microstructure and surface evolution in Al-0.5wt.%Cu polycrystalline thin films*. *Journal of Electronic Materials*, 2002. **31**(1): p. 55-65.
49. Wilson, R.J. and B.L. Weiss, *A review of the properties of aluminium alloy films used during silicon device fabrication*. *Vacuum*, 1991. **42**(12): p. 719-729.
50. Nahar, R.K. and N.M. Devashrayee, *On the specular reflectivity of rf sputtered AlSi alloy thin films*. *Vacuum*, 1986. **36**(4): p. 223-225.
51. Jameson, E., *Electrical Discharge Machining 2001*: Society of Manufacturing Engineers 344.
52. Rasband, W. *ImageJ - Image Processing and Analysis in Java*. 1997 [cited; Available from: <http://rsb.info.nih.gov/ij/download.html>.
53. Olaya-Luengas, L., *Characterization of Squeeze-Cast AlB<sub>12</sub>/Al and AlB<sup>2</sup>/Al Composites*, in *Mechanical Engineering*. 2009, University of Puerto Rico: Mayaguez. p. 87.
54. Hidalgo, R.G.I., *Tribological Characterization of Al-Cu-Mg-B Composites Subject to Mechanical Wear*, in *Mechanical Engineering*. 2009, University of Puerto Rico: Mayaguez. p. 97.
55. *Handbook of Aluminum Physical Metallurgy and Processes*, ed. D.S.M.G.E. Totten. 2003, New York: M. Denkker, Inc. 339.
56. *MDI Jade Software Material Data Inc.*: Livermore, CA.
57. Kohn, E., *Analytical Chemistry*. Vol. 32. 1960. 296.
58. Wong-Ng, W., McMurdie, H., Paretzkin, B., Hubbard, C., Dragoo, A., . ICDD Grant-in-Aid 1988 [cited].
59. *ASM Handbook*. Metallography and Microstructure, ed. G.F. Vander-Voort, Lampman S.R., and Sanders, B.R. . Vol. 9. 2004, Materials Park, Ohio: ASM International. 123-134.
60. Aniban, N., R.M. Pillai, and B.C. Pai, *An analysis of impeller parameters for aluminium metal matrix composites synthesis*. *Materials & Design*, 2002. **23**(6): p. 553-556.
61. Gutierrez, G., Suárez, O.M., and Giordano, M.A., *Numerical Modelling of Centrifugal Casting of Functionally-Graded Aluminum Matrix Composites Reinforced with Diboride Particles*. *Asociación Argentina de Mecánica Computacional*, (2007). **26**: p. 2612-2622.
62. Wei, C.N., Bor, H.Y., Ma, C.Y., and Lee, T.S. , *A study of IN-713LC superalloy grain refinement effects on microstructure and tensile properties*. *Materials Chemistry and Physics*, (2003). **80**: p. 89-93.

63. Ramakrishnan, N., *An Analytical Study on Strengthening of Particulate Reinforced Metal Matrix Composites*. Acta Materialia, 1996. **44**(1): p. 69-77.
64. Rodríguez, J., Garrido-Maneiro, M.A., Poza, P., Gómez-del Río, M.T., *Determination of Mechanical Properties of Aluminum Matrix Composites*. Materials Science and Engineering, 2006. **A 437**: p. 406-412.
65. Olivas, E.R., Swadener, J.G., Shen, Y.-L., *Nanoindentation measurements of surface residual stresses in particle-reinforced metal matrix composites*. Acta Materialia, 2006. **54**: p. 263-268.
66. Melgarejo, Z.H., et al., *Study of particle-matrix interaction in Al/AlB<sub>2</sub> composite via nanoindentation*. Materials Characterization, 2010. **61**(2): p. 135-140.
67. Xue Jiang, J.Z., Aimin Wu, Yizhen Bai, and Xin Jiang, *Mechanical and electronic properties of B12-based ternary crystals of orthorhombic phase*. Journal of Physics: Condensed Matter 2010. **22**: p. 1-8.
68. Shein, I.R., and Ivanovskii, A.L, *Elastic properties of mono- and polycrystalline hexagonal AlB<sub>2</sub>-like diborides of s, p and d metals from first-principles calculations*. Journal of Physics: Condensed Matter, 2008. **20**: p. 1-10.
69. Zhou Xiao-Lin, L., Chen Xiang-Rong, and Zhu Jun, *Structural and thermodynamic properties of AlB<sub>2</sub> compound*. Chinese Physics. Society, December 2006 **15**(12): p. 3014-3018.
70. *Thermal Properties of Metals*, ASM International: Materials Park, Ohio, USA.
71. Arsenault, R.J.a.S., N. , *Dislocation Generation due to Differences between the Coefficients of Thermal Expansion*. Materials Science and Engineering, 1986. **81**: p. 175-187.
72. International, A., *Thermal Properties of Metals*, ASM International: Materials Park, Ohio, USA.
73. MatWeb. *Material Property Data*. [cited; Available from: <http://www.matweb.com/search/DataSheet.aspx?MatGUID=7d1b56e9e0c54ac5bb9cd433a0991e27&ckck=1>.
74. MatWeb. *Material Property Data* [cited; Available from: <http://www.matweb.com/search/DataSheet.aspx?MatGUID=9aebe83845c04c1db5126fada6f76f7e>
75. *Aluminum-Silicon Alloys*. 2010 [cited 2010 November]; Available from: <http://www.keytometals.com/Article80.htm>.
76. Elomari, S., Skibo, M. D., Sundarajan, A., Richards, H., *Thermal Expansion Behavior of Particulate Metal-Matrix Composites*. Composites Science and Technology, 1998. **58**: p. 369-376.
77. Lu, K. and M.L. Sui, *Thermal expansion behaviors in nanocrystalline materials with a wide grain size range*. Acta Metallurgica et Materialia, 1995. **43**(9): p. 3325-3332.
78. Liu, Y., et al., *Grain growth and grain size effects on the thermal expansion properties of an electrodeposited Fe-Ni invar alloy*. Scripta Materialia, 2010. **63**(4): p. 359-362.
79. Sui, M.L. and K. Lu, *Thermal expansion behavior of nanocrystalline Ni---P alloys of different grain sizes*. Nanostructured Materials, 1995. **6**(5-8): p. 651-654.
80. Zhang, H. and B.S. Mitchell, *Thermal expansion behavior and microstructure in bulk nanocrystalline selenium by thermomechanical analysis*. Materials Science and Engineering A, 1999. **270**(2): p. 237-243.
81. Tseng, F.G. *Lecture 6. Physical Vapor Deposition*. Advance Micro System Fabrication and Lab 2001 [cited 2010 11/06/2010]; Available from: <http://www.ess.nthu.edu.tw/~fangang/download/Micro%20System%20Fabrication%20and%20Experiment/LEC6-PVD.pdf>.
82. Morita, S., Wiesendanger, R., Meyer, E., *Non-contact Atomic Force Microscopy*. NanoScience and Technology, ed. P. Avouris, Klaus von Klitzing, D., Sakaki, H., Wiessendager, R. 2002, Germany: Springer.

83. *Sputtering*. 2011 [cited; Available from: <http://en.wikipedia.org/wiki/Sputtering>].
84. *Surface Roughness*. 2011, Wikipedia.
85. Onoda, H.N., Tadashi; Touchi, Kenshin; Hashimoto and Keiichi, *Effects of insulator surface roughness on Al-alloy film properties and electromigration performance in Al-alloy/Ti insulator layered interconnects*. Journal of Vacuum Science & Technology B: Microelectronics and Nanometer Structures, Jul 1996. **vol.14**(4): p. 2645-2655.
86. Kylner, C. and L. Mattsson, *Enhanced optical performance of aluminum films by copper inclusion*. Thin Solid Films, 1999. **348**(1-2): p. 222-226.
87. Najarian, S., J. Dargahi, and A.A. Mehreizi, *Artificial Tactile Sensing in Biomedical Engineering*. 2009, New York, USA: McGraw-Hill 233.
88. Fernández, I., *Stress and nanostructure control for the development of magneto-electro-mechanical micro-devices.*, in *Physics*. 2008, Instituto de Microelectrónica de Madrid: Tres Cantos. p. 131.
89. Shaaban, E.R., Afify, N. and El-Taher, A. , *Effect of film thickness on microstructure parameters and optical constants of CdTe thin films*. Journal of Alloys and Compounds, 2009. **482**: p. 400-404.
90. Quintana, O., A.I., and Corona, J.E. , *Thickness effects on aluminum thin films*. Superficies y Vacío, 1999. **9**: p. 280-282.
91. Oliver, W.C.a.P., G.M. , *An improved technique for determining hardness and elastic modulus using load and displacement sensing indentation experiments*. Journal of Materials Research, 1992. **7**: p. 1564-1583.
92. Saha, R. and W.D. Nix, *Effects of the substrate on the determination of thin film mechanical properties by nanoindentation*. Acta Materialia, 2002. **50**(1): p. 23-38.
93. Wang, M., Liechti, K.M., White, J.M., Winter, R.M., *Nanoindentation of polymeric thin films with an interfacial force microscope*. Journal of the Mechanics and Physics of Solids, 2004. **52**: p. 2329-2354.
94. Chen, S., L. Liu, and T. Wang, *Size dependent nanoindentation of a soft film on a hard substrate*. Acta Materialia, 2004. **52**(5): p. 1089-1095.